Combustion Characteristics for Non-homogeneous Segregated H2-Air Mixtures

by

Maha Manoubi

Thesis submitted to the
Faculty of Graduate and Postdoctoral Studies
In partial fulfillment of the requirements
For the M.A.Sc. degree in
Mechanical Engineering

Department of Mechanical Engineering
Faculty of Engineering
University of Ottawa

Abstract

The work presented in this thesis is an investigation of the dynamics of unconfined hydrogen-air flames in the presence of buoyant effects and the determination of an ignition criterion for flame propagation between adjacent pockets of reactive gas separated by air. The experimental work was conducted using the soap bubble technique and visualized with high speed schlieren or large scale shadowgraph systems. A study was first conducted to determine the most suitable soap solution additive among glycerol, guar and polyethylene oxide for conducting the experiments, isolating guar as the best candidate. The soap solution was then used to study the dynamics of flames in single or multiple soap bubbles filled with reactive mixtures of different compositions. The soap bubble method was also further improved by designing a soap dispenser that can maintain a bubble indefinitely, and a method to burst the soap solution prior to an experiment using timed heated wires.

In the experiments with single bubbles, it was found that for sufficiently lean hydrogen-air mixtures, buoyancy effects become important at small scales. The critical radius of hemispherical flames that will rise due to buoyancy was measured and estimated using a model comparing the characteristic burning speed and the rise speed of the flame kernel. Excellent agreement was found between the model predictions and the measured critical flame radii.

The experiments with multiple bubbles provided the scaling rules for flame transition between neighboring pockets of hemispherical or spherical shape separated by an inert gas. The test results demonstrated that the separation distance between the bubbles is mainly determined by the expansion ratio when the buoyancy effects are negligible, corresponding to near stoichiometric mixtures. For leaner mixtures with stronger buoyant effects, the critical separation distance was no longer governed by the expansion ratio alone, as buoyancy forces render the flame propagation across the inert gas more difficult. Visualization of the ignition dynamics confirmed that buoyancy forces tend to accelerate the first kernel up before ignition of the second kernel can be achieved.

Acknowledgements

First and foremost, I would like to express my deepest gratitude to my supervisor, Dr. Matei I. Radulescu, for all his guidance, mentorship and feedback throughout all the time of research and writing of this thesis. Furthermore, I would like to thank Dr. Zhe Liang for useful help and recommendations throughout this work.

A special thanks goes to my team mates and friends Maxime La Flèche, Kadeem Dennis and Louis Leblanc. I would also like to thank Leo Denner at the Mechanical Engineering machine shop for his contribution, and everyone involved in the Detonation and Reactive Dynamics Laboratory (DRDL) at the University of Ottawa for their academic help. Finally, I would like to thank Atomic Energy of Canada Limited (AECL) for financial support.

Dedication

I would like to dedicate this thesis to my dear parents.
A special thanks to my parents and my brother. Words cannot express how grateful I am for their endless love, encouragement and the sacrifices that they have made on my behalf. I would also like to thank all of my friends and roommates who supported me.

Table of Contents

List of Tables

List of Figures

Nomenclature

Greek Symbols

ρ	Density
θ	Ratio of the characteristic time scales of burning and buoyancy

Roman Symbols

D	Diameter
Fr	Froude number
g	Gravity
R_1^*	Final radius of the flame
R	Bubble radius
R_{switch}	Critical flame radius
S_L	Laminar flame speed
t_{rise}	Characteristic time scale of flame rising
V_{burn}	Spatial velocity of the flame
V_{rise}	Characteristic rise speed of the flame

Subscripts

$()_1$	First bubble
$()_2$	Second bubble
$()_b$	burnt
$()_u$	unburnt

Chapter 1

Introduction

1.1 Background and motivation

Loss of coolant accidents (L.O.C.A) in water-cooled nuclear power plants, regardless of how infrequent, engender cumbersome and serious consequences. Those accidents are generally caused by a cooling system failure, which leads to an overheat of the reactor core. At high temperature, this reactor core made with zirconium cladding reacts with the surrounding steam to produce hydrogen [1]. In the aftermath, large amounts of hydrogen can escape and be released into the containment or reactor buildings. Mixed with air, this hydrogen can violently explode.

Combustion behaviour of hydrogen-air mixtures is thus of interest in the analysis of accidental scenarios for hydrogen applications, particularly the large-scale deflagrations in the open atmosphere as in postulated post-accident nuclear containments. To overcome risks and provide hydrogen safety it is important to understand the underlying physical phenomena related to flame propagation process in non-uniform media.

Earlier investigations have mostly dealt with uniform mixtures and most codes and standards are developed based on data obtained from premixed uniform hydrogen-air mixtures [2, 3]. In reality, stratified regions of hydrogen concentration exist prior to complete mixing. In fact, in several industries, weak releases of hydrogen gas in confined irregular spaces (e.g., industrial facilities for hydrogen production, distribution and storage, containment buildings in nuclear reactors) can yield small or large-scale pockets of partially mixed hydrogen-air mixtures that slowly accumulate in discrete locations (e.g., corners of equipment, ceiling cavities, and areas without adequate ventilation). Indeed, formation of stratified combustible mixtures is significant in a wide range of industrial fire and explosion scenarios.

Experimental investigations as well as a theoretical understanding of flame propagation in non-homogeneous environments are underdeveloped compared to the well-established uniform and homogeneous flames. Knowledge gaps in combustion characteristics for non-uniform hydrogen-air mixtures require closure for safe regulation of nuclear power plants. However, limited guidelines are available for estimating explosion characteristics in non-homogeneous mixtures. The first studies on stratified mixtures were undertaken to investigate the non-uniform flame propagation in stratified charge internal combustion engines. Most available data address mixtures with composition gradients, and how the flame propagates normal or parallel to such gradients [4, 5, 6, 7, 8, 9, 10]. For instance, Badr and Karim studied flame propagation in an horizontal tube with multiple inlets used to obtain a variable concentration upward and downward [5]. They have investigated the flame propagation in the same direction as the mixture gradient. A later investigation was performed with propane-air flames propagating through concentration gradients in a vertical combustion chamber separating the lean mixture on the upper part of the vessel from the rich mixture on the lower part by a porous plate [7]. Another work has been conducted in a spherical latex balloon filled with a lean mixture and containing another internal balloon of rich mixture to simulate a discontinuity in the concentration [11]. Hydrogen-air deflagrations of stratified mixtures with concentration gradients were also studied in large scale experiments by Whitehouse et al. [6], who used a 10 m^3 cylindrical vessel.

The soap bubble technique, used in the present study, has proven to be quite relevant to studies of flame propagation in non-uniform mixtures. Sochet et al. used soap bubbles filled with a reactive mixture to induce a reactivity gradient by diffusion after the breaking of the soap film [8]. In an early investigation, Girard et al. [4] were able to study the flame propagation through stratified mixtures (including hydrogen-air) by blowing two concentric hemispherical bubbles one inside the other filled with different concentrations. Since the overpressure generated by an unconfined deflagration depends on the flame acceleration, which depends on the concentration gradient of the mixture, the aim of those studies was to study the pressure profile to better understand the deflagration process in non-uniform mixtures. Results indicated that the peak overpressure generated by the layered hemisphere is three times larger than the peak produced by the homogeneous hemisphere. They also found that for a flame propagating through an increment concentration the velocity increases, giving only one overpressure peak with high amplitude. However, for a decreasing concentration, the velocity slows down and gives two peaks of over-pressure with a lower amplitude. Furthermore, the lean flammability limit was found to be lower in the stratified mixture than in the homogeneous mixture for hydrogen fuel, a fact to be considered for safety purposes.

In spite of a substantial amount of study of flame propagation in mixtures with composition gradients, to the best of the author's knowledge, guidelines for assessing the conditions for deflagration propagation between isolated regions of combustible mixtures do not currently exist. The lack of practical guidelines in non-homogeneous environments, as well as lack of fundamental basic physical principles governing this phenomenon, is of particular concern in an industry-wide hydrogen economy grouping production, distribution, storage, and the end user of hydrogen in homes. Knowledge gaps in combustion characteristics for non-uniform hydrogen air mixtures are also a concern for safe regulation of nuclear power plants.

The main thrust of the present study is thus to examine the combustion characteristics of non-homogeneous segregated hydrogen-air mixtures. The purpose is to investigate the physical mechanisms governing the flame propagation between neighboring reactive pockets, separated by an inert, or much weaker, usually non-ignitable mixture and develop scaling rules for flame propagation in non-uniform hydrogen-air mixtures, simulating real accident configurations.

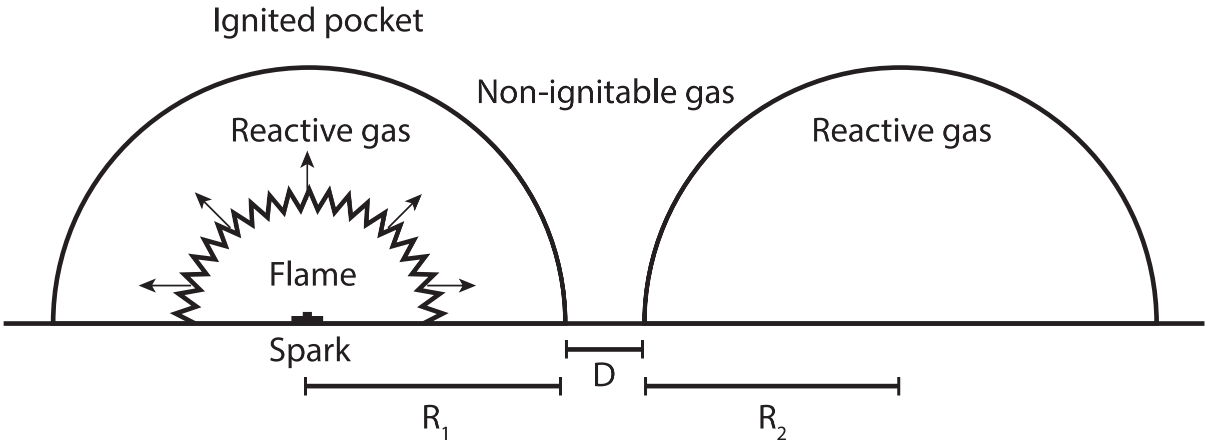

Figure 1.1: Problem investigated: criteria for the propagation of a deflagration wave from one reactive cloud to another, separated by an inert or non-ignitable mixture.

1.2 Problem definition and objective

Figure 1.1 shows the physical problem studied. Considering two adjacent clouds of reactive gases, the conditions for a deflagration wave to propagate from the first cloud to the second one are determined in terms of the cloud mixture compositions and dimensions. Prior to examining the ignition mechanism between two bubbles, studies were first performed to understand the dynamics of flame propagation inside one bubble. The objective of the present study is thus to clarify the physical mechanisms for flame propagation in non-uniform mixtures and develop the scaling rules for flame propagation in non-uniform mixtures of combustible and air, simulating real accident configurations.

1.3 The soap bubble technique

To reproduce individual pockets of reactive gas, the soap bubble technique was used to fill prescribed volumes of reactive gas surrounded by air. The soap bubble method was first proposed by Stevens in 1926 to measure the burning velocity of freely expanding spherical flames in a constant pressure environment [12]. It was further improved by Linnett et al. [13] and Strehlow et al. [14]. One advantage of this method is that it does not involve any consideration of confinement, such as pressure increase and wall interactions [14]. In this method, the combustible mixture is used to blow a spherical soap bubble around a pair of spark electrodes. A very thin soap film contains the reactive mixture of interest [12]. The thin film of the bubble cannot sustain any pressure build-up in the bubble. The bubble thus grows during the experiment, accommodating the expansion of the burned gases. Soap bubbles are cheap and easy to make, as well as transparent, making visualization relatively simple.

Most of previous soap bubble experiments, such as those performed by Guibert et al. and Strehlow et al. [15, 14], were however limited to small bubbles with diameters less than approximately 10 cm. There have been however claims by soap bubble hobbyists that certain soapy solutions may permit one to form large scale bubbles on the order of few meters [16, 17, 18, 19].

A soap bubble consists of two soap films with a thin water layer in between [16]. A soap bubble will fail when the film gets too thin. This occurs as a result of water draining from between the soap monolayers. Fluid flow in soap films has been studied in detail by Rutgers and Hidema [16, 17]. In a hemispherical bubble, failure begins as water drains from the top of the bubble, making the film extremely thin. Small holes begin to open in the film where there is no water, and these coalesce together into larger holes. Eventually the holes merge into a single crack, which breaks the remaining film. Evaporation of water in the bubble is also suspected to accelerate this process.

Soap films have two primary ingredients: soap and water. Rutgers and Ballet [16, 18] have found that Proctor & Gamble's Dawn soap produces the most desirable soap films. Typical soap concentrations they have tested range between 1 % and 10 % by volume. Ballet found that a soap concentration of 4 % soap permitted them to obtain the longest soap curtains [18]. Our investigation has thus adopted this particular composition as starting point. It is not uncommon for soap solutions to include additives in order to change the surface elasticity of the solution, which has been shown by Ballet [18] to be related to stability of the film. A stable soap film is one that can have a variation in film thickness and return to a constant state [18]. Soap bubble hobbyists have discovered several polymer additives that can improve soap film performance. Glycerol, polyethylene oxide (PEO), and guar gum are common additives in household bubble solution formulations. PEO as an additive in soap solution has been studied by Hidema [17], and guar is a popular additive for home enthusiasts [19].

This study thus first aims to characterize these anecdotal claims, in order to select the soapy solution offering the best prospects for studying flames in single and double bubbles. Development of the soap bubble technique used in this study is described in Chapter 2.

1.4 Large scale visualization

In the early use of the soap bubble method, the experiments were visualized by direct photography, which was not convenient for the low luminosity of most flame fronts. In 1951, Pickering and Linnett [20] improved the visualization technique of the soap bubble method from the direct photography to a schlieren system, which relies on the large density gradients at the flame front to capture very well the flame shape. In this perspective, we have used the schlieren technique to visualize the flame dynamics in some of our experiments.

The schlieren system available is limited to the dimensions of the mirrors (30 cm), which restrict the bubbles' sizes. While larger fields of views would be available with larger mirrors, parabolic first surface mirrors are very expensive and generally unavailable for dimensions exceeding 50 cm. Thus, for view areas exceeding approximately one meter, this method become more complicated to implement. A shadowgraph system was used instead. Recently, Settles developed an affordable large-scale shadowgraphy system for visualization of explosions and gunshots [21]. To be able to visualize the flame transition in larger and double bubble experiments, a similar shadowgraph system more suitable than the schlieren system has been implemented, details of which were recently published by Dennis et al. [22]. The details of the implementation are presented in Chapter 3.

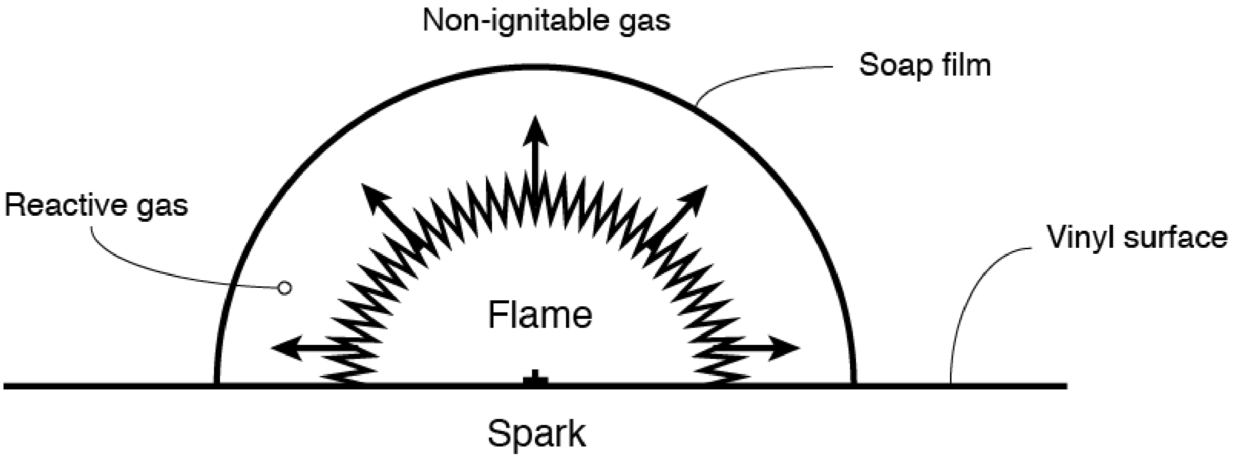

Figure 1.2: Bubble sketch.

1.5 Outline of the present study

The present thesis addresses the dynamics of flames in single bubble and two bubble (hemispherical and spherical shapes) experiments. The purpose of each type of experiment is explained in the following sections.

1.5.1 Deflagration in Single bubbles

In the current study, we are interested in hydrogen-air mixtures near the lean flammability limit. In such weak mixtures, buoyancy effects may begin to play a role. This is because the flame speed may fall below the characteristic rise speed of the burned products due to buoyancy [23]. This signifies that the flame may rise while it is burning. This convective motion is expected to play an important role in the multiple-bubble deflagrations which are of interest in the present study. Chapter 4 thus addresses the dynamics of unconfined deflagrations of single bubbles (see Fig. 1.2) under the possible influence of buoyant forces. The scaling laws suggested by Babkin et al. [24] and Zingale & Dursi [25] for determining the flame size at which buoyant effects become important are verified experimentally. The criteria for various hydrogen-air compositions from the lean flammability limit to stoichiometric compositions are evaluated.

1.5.2 Deflagration with Two Bubbles

Chapter 5 presents the results of experiments aimed at determining the critical conditions for deflagrations to propagate across two separated mixture pockets. Two bubbles were created side by side with the desired spacing, individual dimensions and gas compositions. One pocket was ignited with a weak spark, and the experiments monitored if the flame successfully spread to the other pocket. Chapter 6 presents the experimental results obtained for two spherical bubbles. The comparison with the results obtained with the hemispherical bubble tests permitted one to study the exact role played by wall boundary layers.

1.6 Thesis organization

This thesis is organized as follows. Details on the experimental procedure and our selection of the soap bubble solution are provided in Chapter 2. The visualization systems used in the various experiments are documented in Chapter 3. The visualization of H_2-air deflagrations in single bubbles is reported in Chapter 4, along with laminar flame speed measurements, the measurement of the critical radius at which the buoyancy forces become important, and its prediction using scaling laws. In Chapter 5 are reported experiments with two adjacent reactive mixtures, and the conditions for the flame to propagate successfully. Chapter 6 reports on a preliminary study of flame propagation between two nearly spherical flame bubbles. Finally, Chapter 7 summarizes the current investigation and draws conclusions from the experimental results and calculations.

Chapter 2

Experimental details

This chapter provides an overview of the experimental technique used. The soap bubble method is outlined and its implementation is described, including our selection of the soap bubble solution.

2.1 Test set-up

The bubble deflagration tests were performed using the soap bubble method to fill prescribed volumes of hydrogen-air mixtures surrounded by air on a flat plastic sheet. The soap solution selected consists of 40 ml of Dawn detergent per liter of water with an addition of 0.5 g of guar gum. This composition was chosen based on our trials of several candidate mixtures presented in Section 2.2.4.

For the early bubble tests, the soap film was not broken prior to ignition. To examine the effect of soap film on the criterion of flame propagation between bubbles, the soap film was ruptured in the later tests with two neighboring bubbles. The rupture of the soap confinement was achieved using heated wires next to the bubbles before the experiment in order to simulate a truly unconfined setting. See more details in Section 2.5.

All the experiments were conducted at room temperature and atmospheric pressure conditions.

To visualize the experiments, either the schlieren system or the large shadowgraph system was used [22]. The visualization details are addressed in the next chapter.

Figure 2.1 provides a schematic overview of the experiments set-up used for the two-bubble tests using the large-scale shadowgraph system. The set-up is composed of a test area, the visualization components and a command system (as seen in Fig. 2.1). The test area consists of a flat plastic sheet with the wires where the bubbles are generated (as seen in right side of Fig. 2.1). The shadowgraph system includes a retro-reflective screen as a background surface (with length scales of almost 2 m square) and a 1600 W arc lamp as the light source, which was coupled with a high-speed camera to record the video. The BNC box, the trigger module and the computer form the command system. The photographs shown in Fig. 2.1 through Fig. 2.2 illustrate the actual test area and set-up installed in the lab.

2.2 The soap bubble method

The soap bubble technique consists of producing a thin-walled soap bubble with the combustible gas inside [12]. Since the soap film does not resist the expansion of gases, the ignition of the mixture results in the propagation of the flame at nearly constant pressure. For purposes of analysis, the flame travel and the expanding bubble are recorded photographically with a high-speed camera.

2.2.1 Hemispherical bubble generation

In most of the tests performed in the present study, hemispherical bubbles were created over a flat surface made of vinyl. A photograph showing a bubble forming is shown in Fig. 2.3. The bubbles were formed by dipping the end of a 3/8” interior diameter polyvinyl chloride (PVC) tube in soapy solution to form a soap film (Fig. 2.4). The pre-mixed hydrogen-air mixture was fed through the tube forming a hemispherical bubble on the surface. The bubble was filled with combustible gas until the desired diameter was reached, then the tube was removed.

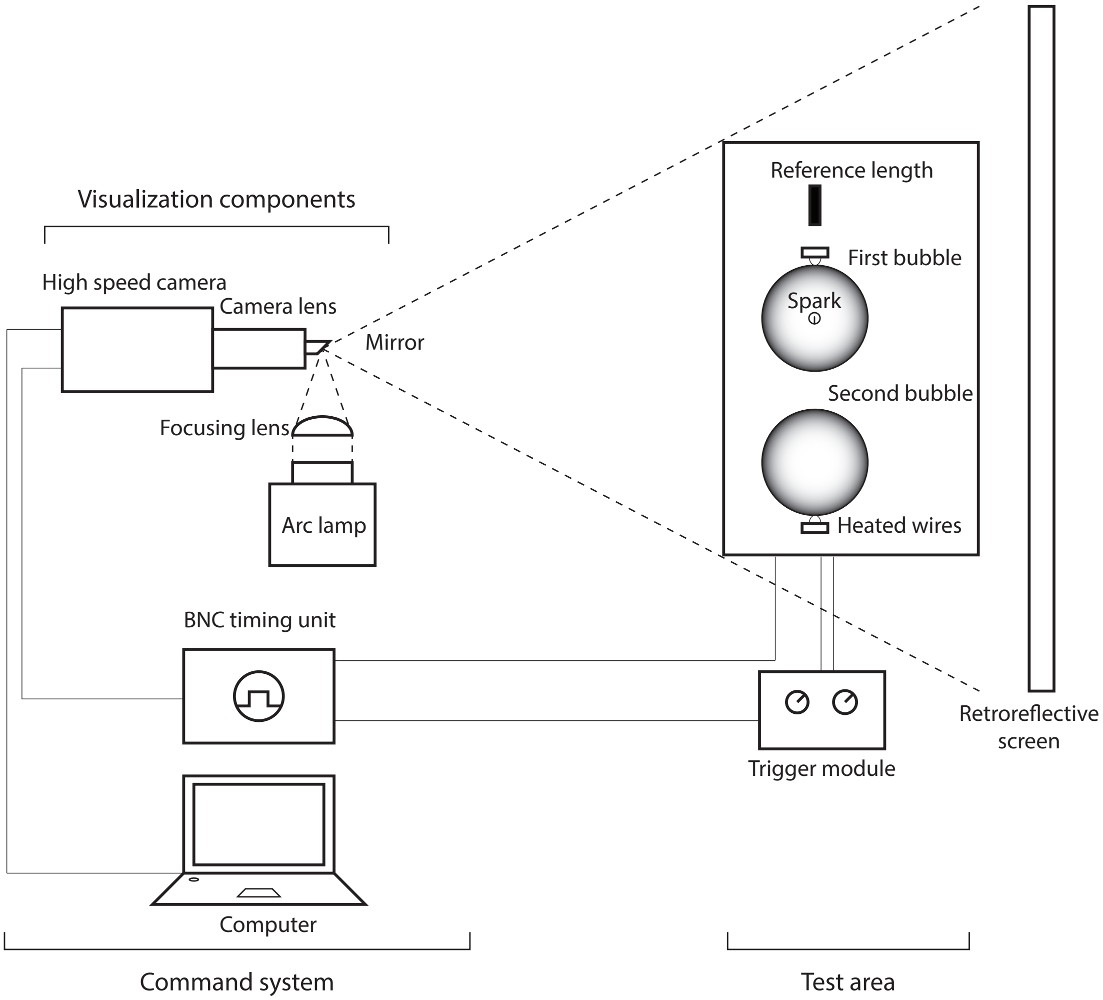

Figure 2.1: Experimental Setup.

Figure 2.2: Full view of the set-up.

Figure 2.3: Blowing the soap bubble with hydrogen-air.

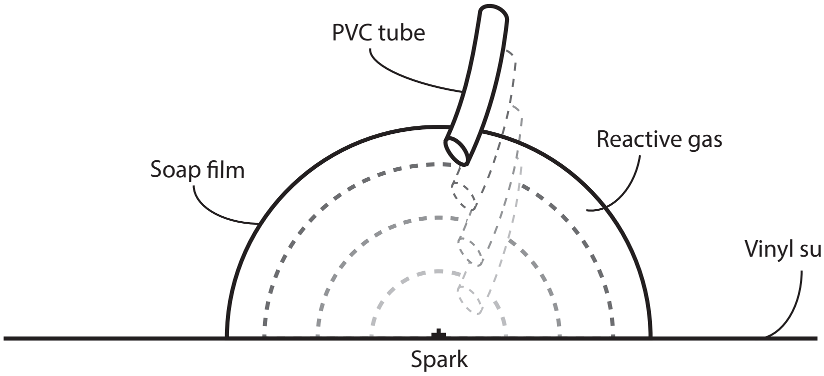

Figure 2.4: Sketch of the bubble generation.

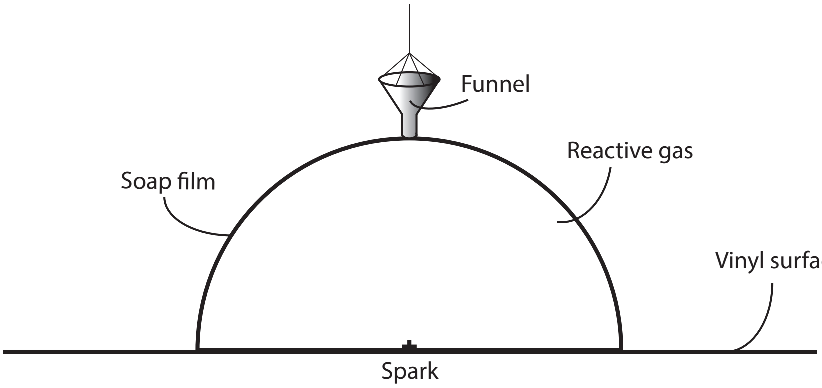

Figure 2.5: Soap film uphold system.

2.2.2 Continuously fed soap bubbles

In order to obtain longer-lived soap bubbles, a soap solution dispenser was developed to prevent the thinning out of the soap bubble due to evaporation (see Fig. 2.5). In fact, as long as the soap film was continuously fed from the top in a symmetric way, the bubble did not burst easily and remained stable and centered. The funnel was filled with soap solution above a small piece of cotton cloth to insure a smooth contact with the soap film. The funnel support was removed by pulling a cord to move the funnel to the side, prior to ignition.

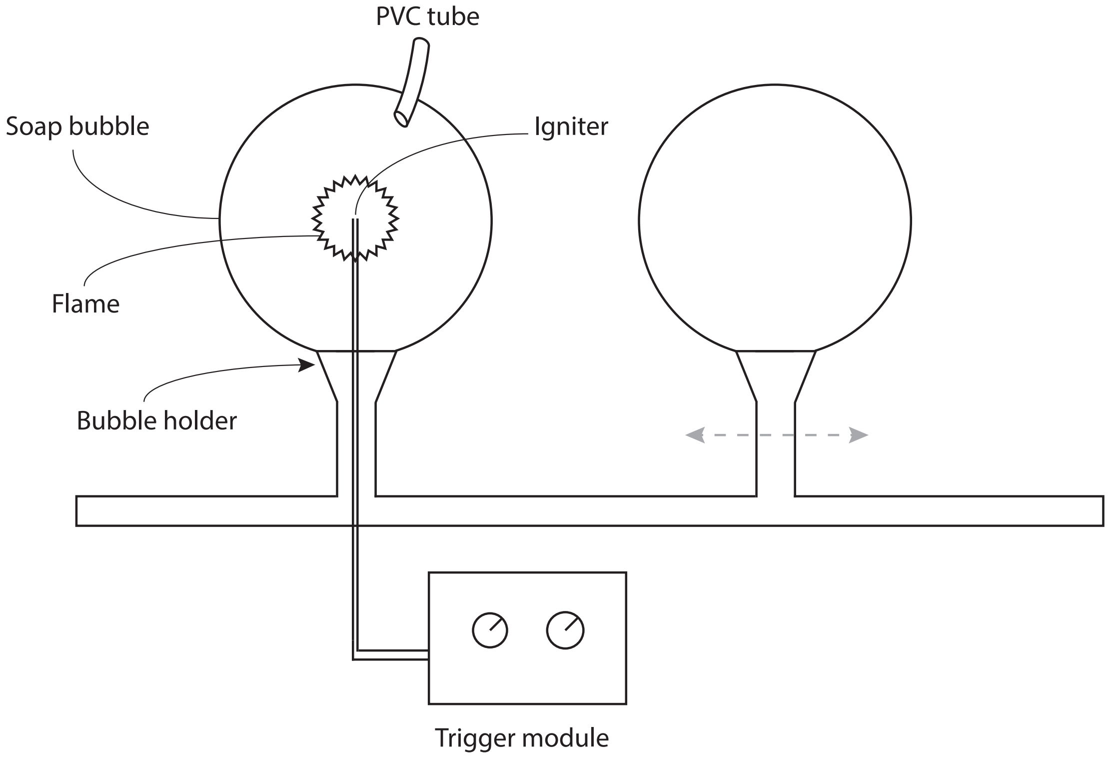

Figure 2.6: Sketch of the spherical bubble system.

2.2.3 Spherical bubble generation setup

An apparatus was constructed and used to blow spherical bubbles away from the plate as shown in Fig. 2.6. It consists of a device for filling spherical bubbles with the reactive mixture at ambient pressure and temperature. Bubbles were formed separately on elevated vinyl platforms as shown in Fig. 2.6. To ensure a regular spherical development of the flame, the radius of the bubbles was limited to 1.5 times the radius of the bubble holder. The shape of bigger bubbles tends to become an ovoid or to be more sensitive to any movement. Moreover, a smooth circular bubble holder is more convenient than a square shaped one. The position of the second bubble could be adjusted by moving the support to the right or to the left and then fix it with a screw.

2.2.4 Selection of the soap solution - Bubble Longevity

To get the most effective soapy solution, the selection of the best additive is needed. In this perspective, we tested three different additives, namely glycerol, guar and PEO. In our preliminary tests, a 10 % glycerol mixture was found to be the worst performer out of the three additives. As a result the remaining two additives were more closely investigated. Our experiments focused on three candidate mixtures, namely a soap-water solution, and the same solution with either PEO or guar gum. The composition of 4 % Dawn soap in water was used with those additives and in isolation as a control. PEO was used in 30 mg per liter of water and guar in 0.5 g per liter of water. The solutions were used to create soap bubbles at six target diameters: 10, 16, 26 and 41 cm. For each mixture and target size, ten tests were performed. For each test, we recorded the lifetime of the bubble, defined as the duration from the start of the bubble formation to when the bubble bursts. We also recorded the survival time, which we defined as the fraction of time between when the target dimension was achieved and when the bubble bursts. Survivability was the major metric for this study because the bubble must be able to consistently survive the time after filling to ignition. All solutions were also subjected to a qualitative study for transparency to schlieren visualization and found to be adequate. It was however found that above 2.0 g of guar gum per liter of water impaired the visualization.

Compressed air was used to make the bubbles on a flat sheet. The tests were performed in a room with minimal ventilation and a stable temperature of 22 °C, at approximately 30 % relative humidity. Fig. 2.7 shows an example of a large hemispherical bubble obtained by this technique using the guar solution (0.5 g of guar per liter of water and 4 ml of Dawn soap). The largest bubble obtained was 70 cm in diameter.

The average lifetime and survival time for each condition and mixture tested are shown in Fig. 2.8. The error bar amplitude is the standard deviation measured. As shown in Figs. 2.8 and 2.9, the solutions containing PEO and guar outperformed the pure soap and water solution. On average, it was found that bubbles made using the guar solution had approximately one minute of survival before the bubble burst. The guar mixture had the highest survival time for all diameters tested and was therefore selected as the mixture

Figure 2.7: A 63.5 cm diameter bubble made using the guar solution.

to conduct flame experiments. It was also found that the lifetime of a bubble for a given bubble solution decreases slightly with respect to size (Fig. 2.8). The survivability time decreases with respect to bubble size mainly because the bubbles take longer to blow to larger diameter (Fig. 2.9). From this, it was concluded that maximizing the flow rate used to blow the bubble should allow the creation of larger bubbles or bubbles with higher survivability.

2.3 Gas mixture preparation

The reactive gases were premixed in a 50 L mixing tank at 3.35 bar and left to diffuse for 24 hours. The composition of the mixtures tested ranged from 7 % H_2-air near to the flammability limit and 30 % H_2-air by volume (near the stoichiometric mixture). Nitrogen, oxygen and hydrogen from pressurized cylinders were mixed in appropriate proportions to provide the required reactive gas composition. The hose used to blow the bubble was entirely evacuated before filling with the gas in order to insure that no air infiltrated the tube and contaminated the mixture. Only the last part of the hose, right after the valve control, was exposed to air and could cause a modification in the percentage concentration

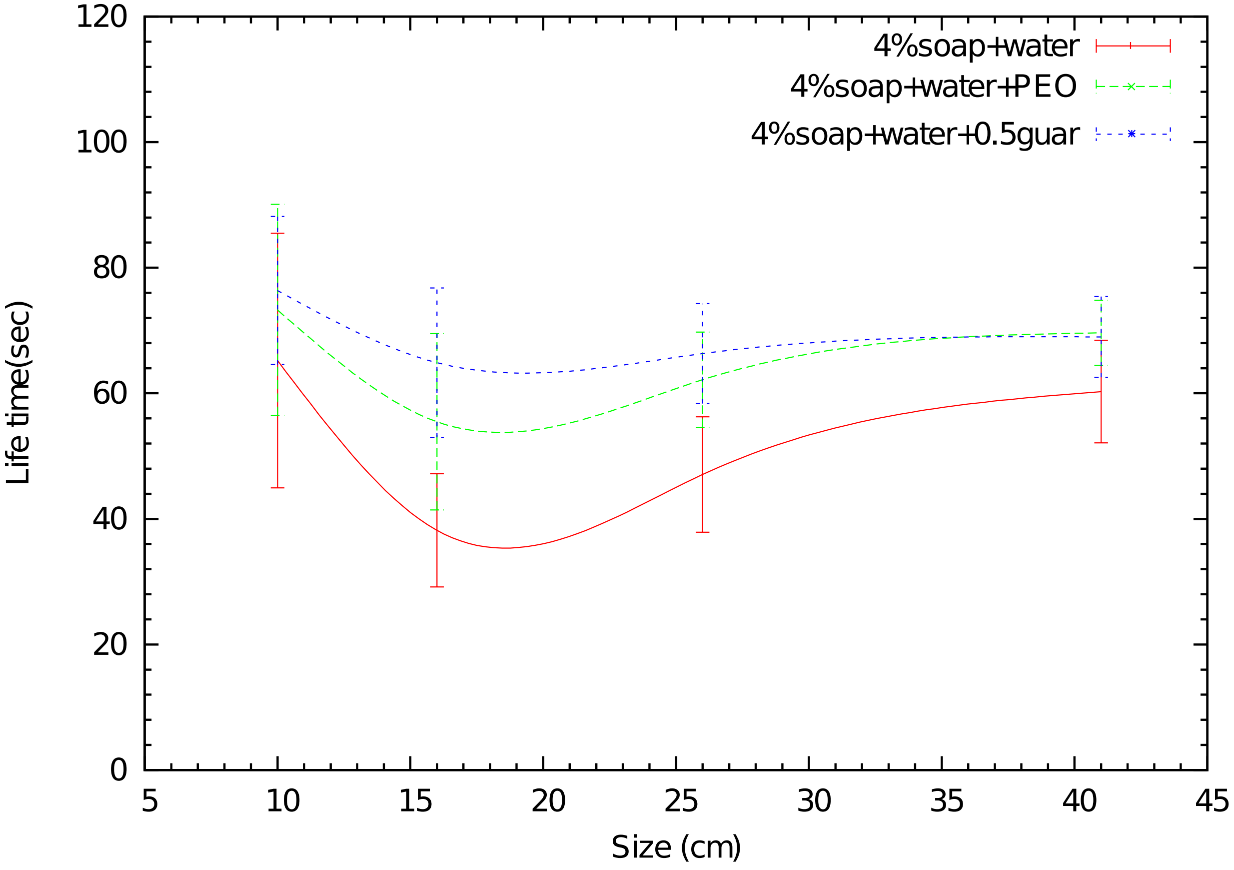

Figure 2.8: Influence of bubble diameter on its lifetime (including formation).

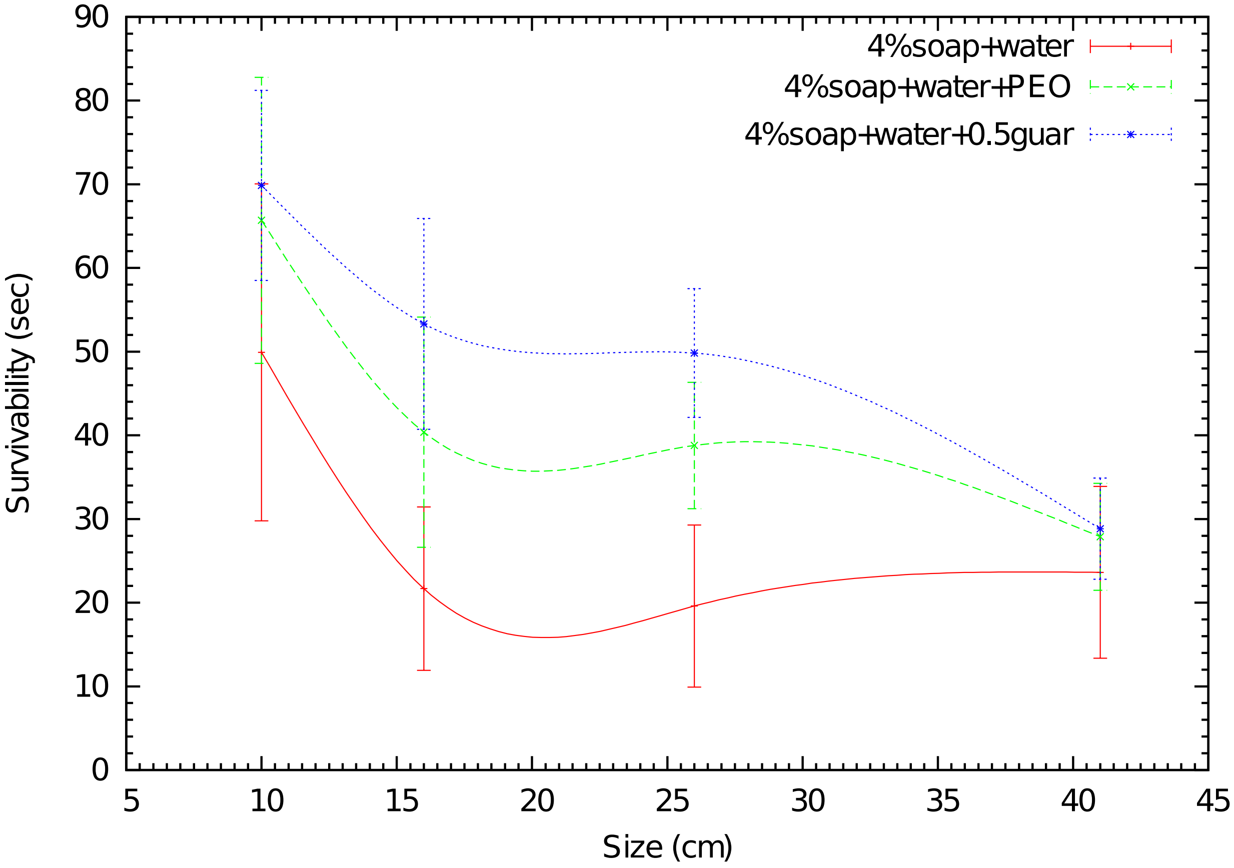

Figure 2.9: Influence of bubble diameter on its survivability at desired size.

of hydrogen, resulting in the decrease of the hydrogen mole fraction by ~ 0.14 %. The effect of this decrease on the flame propagation is negligible.

2.4 Ignition system

For the hemispheric bubbles, the combustion experiments were performed over a vinyl plate, outfitted with an automotive spark plug used as igniter. Bubbles were formed over this ignition source, as shown in Fig. 2.3. For the spherical tests, long copper electrodes were placed up from the bubble support and generated a spark right at the bubble center (see Fig. 2.6). An EG& G TM-11 trigger module was used to generate the required spark. The trigger module represents a compact instrument designed to provide a high voltage trigger pulse (peak of 30 kV) with fast rise time (1 μs). The trigger module consists of a line voltage to DC power supply, a primary triggering circuit and a pulse output transformer. It is used to provide an ignition type pulse. The ignition and visualization systems were synchronized to the ignition event using a BNC timing unit.

2.5 Experiments with burst bubbles

In order to avoid any potential effect of the soap film on the likelihood of the flame to propagate between the reactive pockets, the present technique has been improved by removing the soap film prior to the experiment. This was carried out with a heated Nichrome wire placed next to the soap film of both bubbles and synchronized as the bubbles burst before ignition. A BNC box model 575 insured the synchronization. The camera, the trigger module (controlling the spark) and the wire switch were connected to the BNC box, which allowed the control of each operation with a desired timing. A battery generated the wire heat. The time delay between the beginning of the rupture and the energy deposition through the spark plug varied from 100 to 200 ms (depending on the size of the bubbles). The time delay being relatively short, the diffusion of the uniform gas into the surrounding air due to the rupture of the confining film was assumed to be negligible.

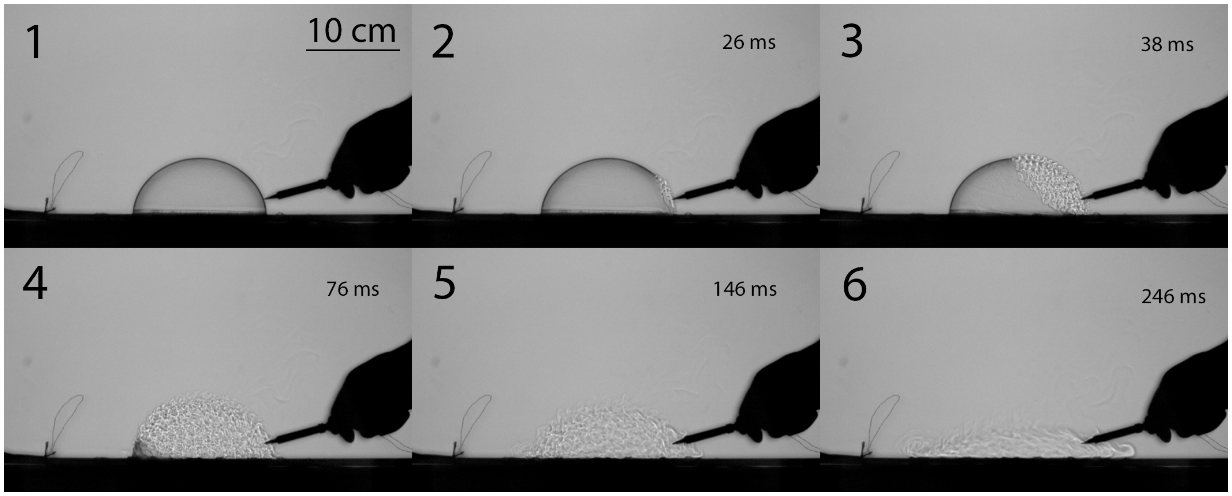

Figure 2.10: CO_2 bubble burst on the side recorded at 500 fps. The resolution is 1280 x 800. The exposure time is 8 μs.

To make sure that the soap film burst at the side did not affect the expansion of the flame in one side more than another, tests were conducted with a non-reactive, heavy CO_2 gas, which allowed the visualization of the soap film being burst. Fig. 2.10 and Fig. 2.11 illustrate the tests made using a soldering iron (one from the top and one from the side). From both shadowgraph images, the heavy gas does not tend to evacuate significantly from the location where the soap film is being burst. Based on those tests, we conclude that the soap film being burst with the wire on the side or on top would not have an important impact on the flame propagation. This was verified with our experiments with the stoichiometric hydrogen-air mixture. As the ignition operates after removing the soap film, the expanding flame remains hemispherical and symmetrical. However, for leaner mixtures, the wires' position may influence the propagation of the flame. The flame spreads towards the side where the bubble burst. In fact, the bubble broke unsymmetrically and could possibly disturb the symmetrical gas motion (see Section 5.2.2).

An example of the synchronization between the soap film bursting and flame ignition is shown in Fig. 2.12.

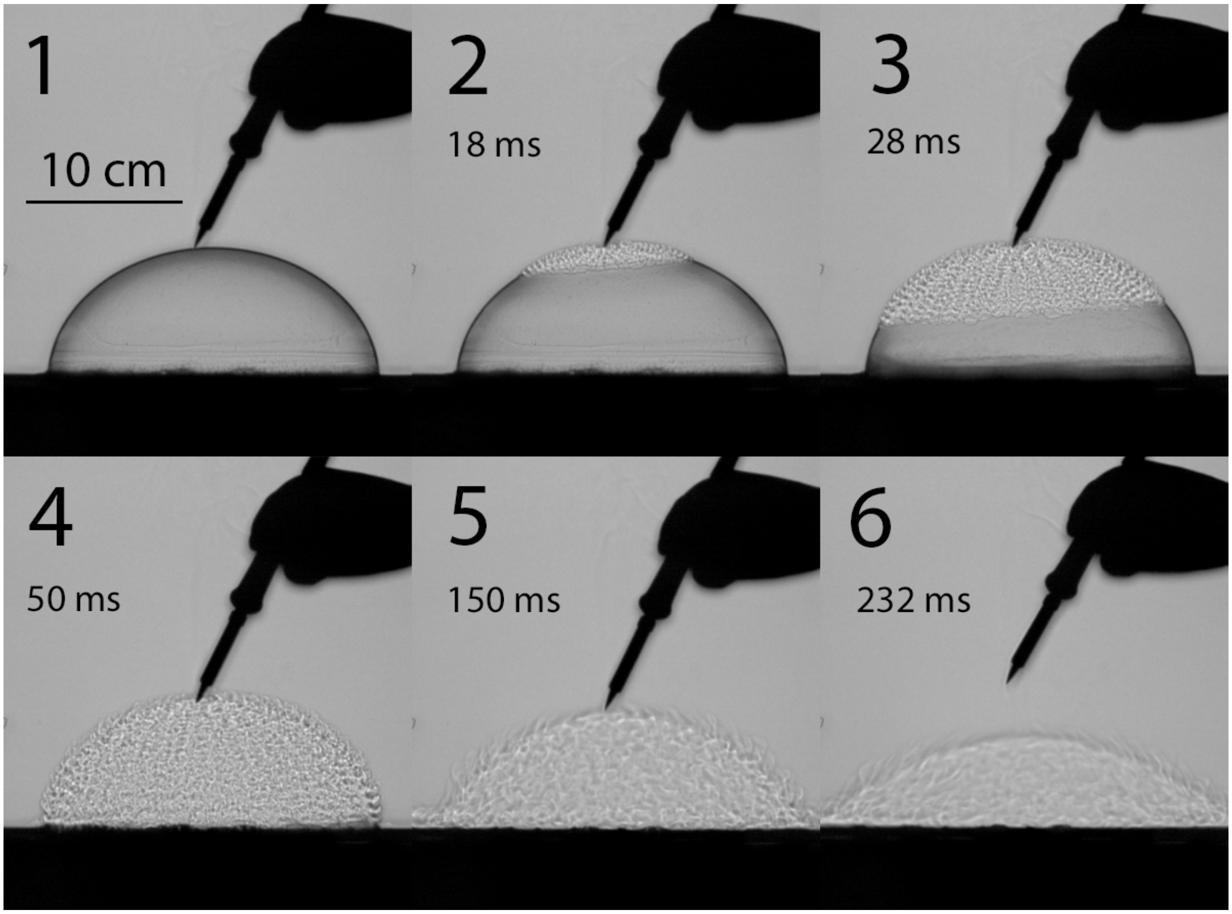

Figure 2.11: CO_2 bubble burst on the top recorded at 500 fps. The resolution is 1280 x 800. The exposure time is 8 μs.

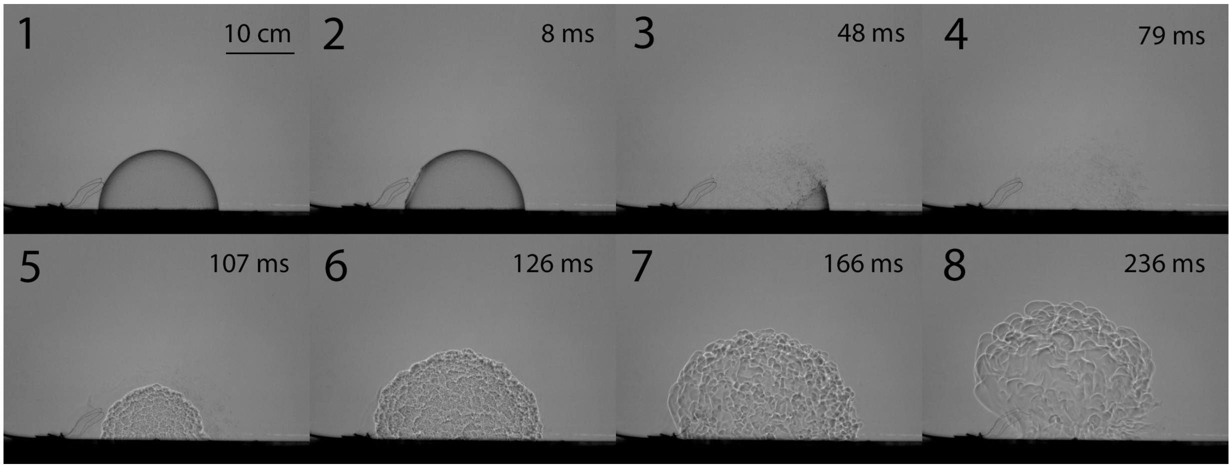

Figure 2.12: Bubble burst test by heated wire with stoichiometric hydrogen-air mixture recorded at 3,000 fps. The resolution is 1280 x 800. The exposure time is 1 μs.

2.6 Image processing and spatial calibration of an image

For each experimental condition, typically 10 frames were chosen and extracted from the video to be analyzed and used in our measurements of the single bubble tests. The dimension of the mirrors of the schlieren system was used as the length scale for dimension calibration. All the measurements were performed using the program ImageJ. For the tests performed with the shadowgraph system, we placed a known reference length scale next to the bubbles to be able to calibrate the field of view. The same reference scale was used in all the shadowgraph records.

Chapter 3

Visualization system

The main diagnostic in the experiments was flame visualization either by schlieren or shadowgraph techniques [26]. This chapter outlines the implementation of these techniques.

3.1 Schlieren system

The flame expansion was imaged and recorded with a conventional Z-type schlieren system. The Z-type schlieren set-up used is shown in Fig. 3.1. The Schlieren technique permits one to measure the first density derivative and relies on the changes of the index of refraction with density changes. The field of view in the Schlieren imaging was limited to the dimension of the mirrors used. In this study they were 12.5 in (31.75 cm) diameter parabolic f8 mirrors. The light source was a 300 W LED producing approximately 16,500 lumens continuously during recording. The details of the schlieren setup have been documented by Bhattacharjee [27].

3.2 Shadowgraphy system design

The shadowgraph system used is an implementation of the Edgerton retro-reflective technique, documented recently by Dennis et al. [22]. In order to construct a large-scale

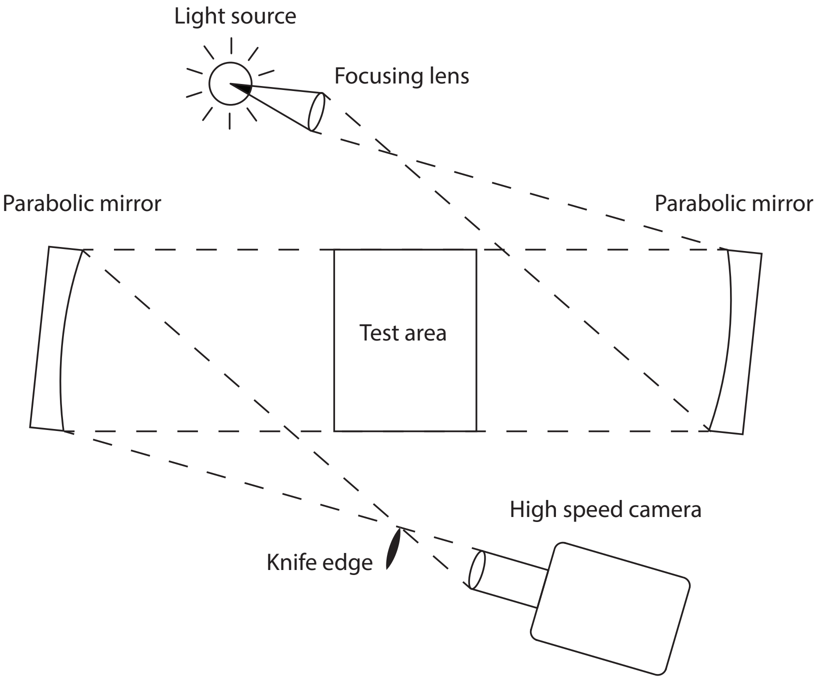

Figure 3.1: Experimental set up using a Z-type schlieren configuration.

shadowgraphy system, there are two prerequisites. The first is a powerful light source to illuminate a large area. The arc lamp's potential in large-scale shadowgraphy has been previously demonstrated, making it a strong light source candidate since it produces continuously high intensity light [21]. The second criterion for large-scale shadowgraphy is the background. In 1958, Edgerton developed a cheap and simple direct technique which does not generate undesirable noise in large-scale shadowgraphy by using a retro-reflective screen [28, 29]. A schematic of the technique is shown in Fig. 3.2. The retro-reflective screen reflects light back towards its origin, giving it a higher reflective ability compared to other screens, which may diffuse light. A key benefit of the screen is light entering at any angle and from any distance will be reflected back to its source. Thus, the retro-reflective screen is flexible, cheaper than mirrors and minimizes background noise while reflecting most incident light, making it ideal for use in shadowgraphy.

Settles modernized and improved Edgerton's technique using an arc lamp and video camera [21]. Hence, the large-scale shadowgraph system implemented for this study uses an arc lamp for a light source and a retro-reflective screen as a background surface. Noise-free shadowgraphs could be taken by placing a light source and camera very close together. When the camera and the light source are not aligned on the same axis, a double image is created owing to parallax. To overcome this effect, the axes of the incident and reflected beams were made to coincide with the help of a small mirror mounted on the end of the camera lens, onto which the light from the light source was focused using a condenser lens [21].

The shadowgraph system implemented in this study uses the same layout as the Settles design shown in Fig. 3.3. For our deflagration tests, positioning of the camera and the background screen is set around 3.65 m. Figure 3.3 also defines the distance between the screen and test section (parameter d), and distance between the screen and camera (parameter f). For highest image quality Settles found that the ratio d/f should be between 0.3 to 0.7 [21]. For all the tests performed, the ratio of d/f ranged between 0.4 to 0.5 [22].

Figure 3.4 shows a top view of the optical components used in the setup, similar to what was proposed by Settles. The light source was a 1600 W xenon arc lamp from Newport. A 50-mm-focal length lens was used to focus the light to a circle of approximately 4 mm in diameter. Rod mirrors of both 5 mm and 10 mm diameter were used. The rod mirror was placed at the focal point of the lens, which reflects light onto the screen. To ensure returning light enters the camera, the rod mirror was mounted on the end of the camera lens. The camera used was a Phantom v1210 from Vision Research. It is a high-speed video camera capable of 1280 by 800 pixels resolution at 12,000 frame per second (fps) or 1,000,000 fps at a reduced resolution of 128 by 16 pixels. A 1.82 m by 1.82 m retro-reflective screen was made by Virtual Backgrounds containing 3M 7610 retro-reflective material and was fitted over an aluminum frame.

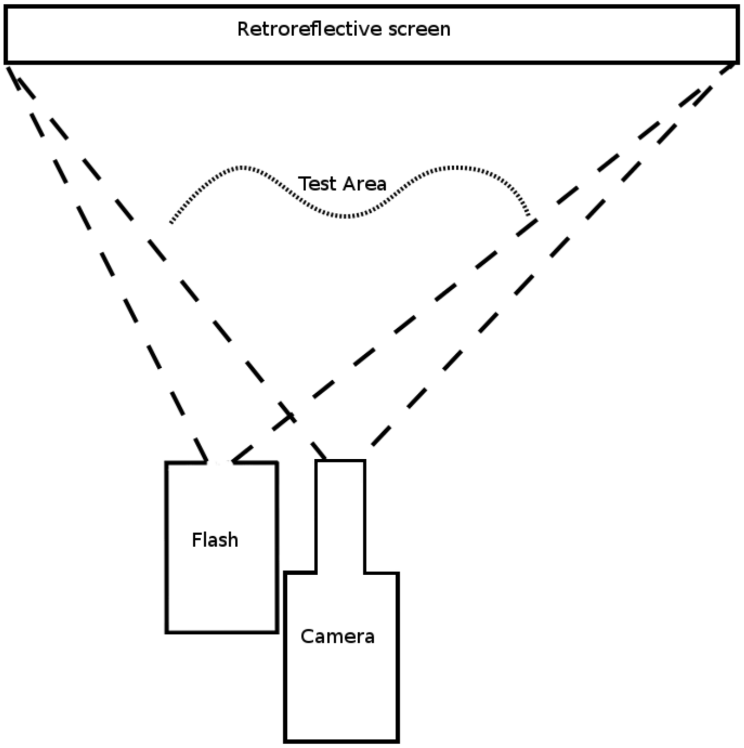

Figure 3.2: Top-view sketch of retro-reflective shadowgraph technique by Edgerton [28].

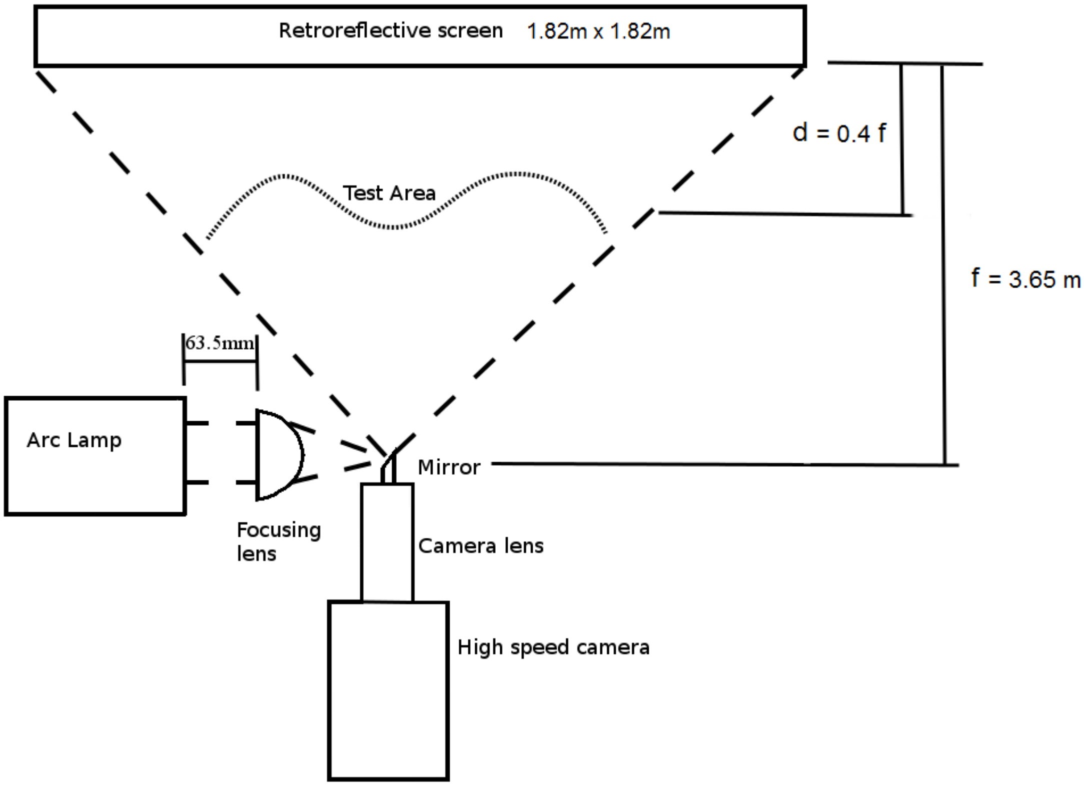

Figure 3.3: Top-view illustration of our retro-reflective shadowgraphy system.

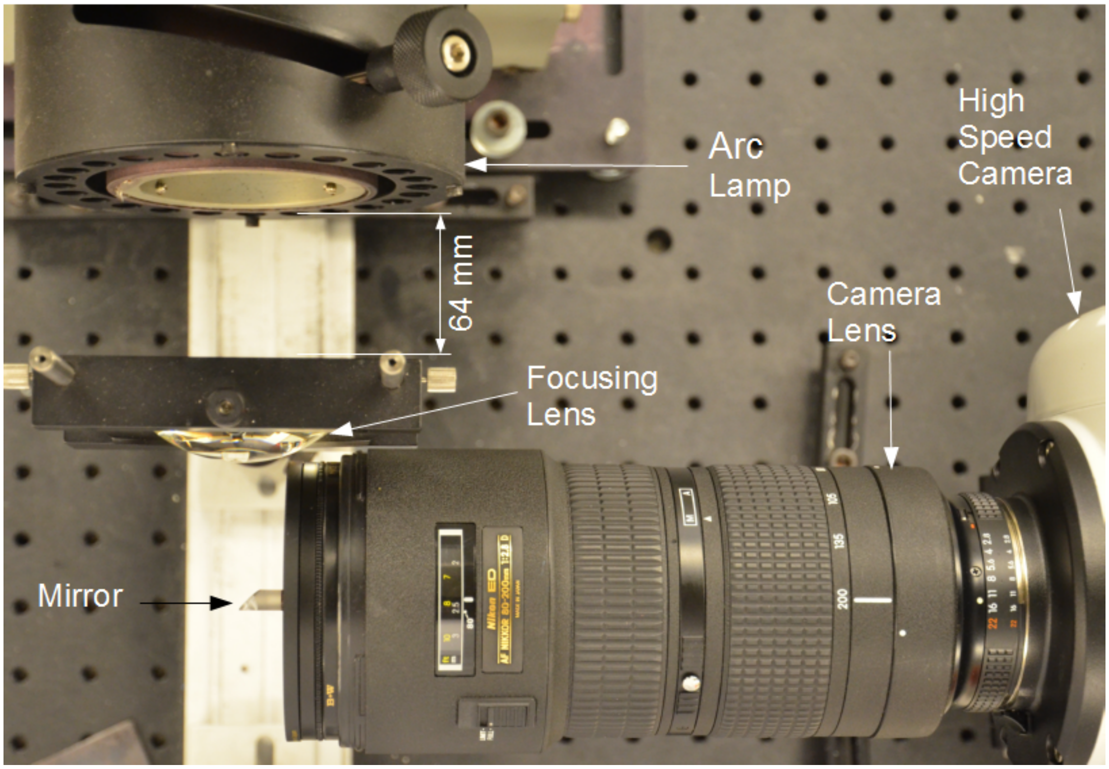

Figure 3.4: Top-view picture of the optical components in our shadowgraphy system.

Chapter 4

Single bubble tests

This chapter details the experiments performed with a single bubble. The focus of these experiments is to study the role played by buoyant forces in lean mixtures close to the flammability limit.

4.1 Test configuration and conditions

For these series of tests, the composition of the mixtures tested ranged from 7% and 30% H_2-air by volume. The dynamics of the unconfined hydrogen-air flames were visualized using schlieren videos. The soap film was not ruptured prior to ignition for these tests. The soap bubbles were hemispherical in shape. The tests were typically recorded at frame rates between 5,000 fps and 30,000 fps, with a resolution set to 512 by 512 pixels. The field of view in schlieren imaging was limited to the dimension of the mirrors used. Select experiments requiring the monitoring of the flame dynamics on larger scales were performed with the large scale shadowgraph system. The average number of tests performed for each mixture was 4 tests. Only one video for every concentration was selected for the measurements of the laminar flame speed and for evaluation of the critical flame radius where buoyant effects become prominent (refer to Section 4.4.2). All the tests were performed at room temperature and atmospheric pressure with minimal ventilation.

4.2 Flame dynamics

Figure 4.1 and Figure 4.2 illustrate the dynamics of non-buoyant flames, measured in 30% H_2-air and 23% H_2-air respectively. The flame assumes a spherically symmetric cellular structure. In these tests, one can notice the soap bubble's growth as the flame propagates to maintain constant pressure. The instabilities developed on the flame structure are also clearly discernible; these have been well documented elsewhere in the literature, see for example [23].

Figure 4.3 shows select frames of a 11.9% H_2-air flame. The flame speed in this case was much lower (with an experimental value of 0.3 m/s compared to 2.5 m/s for 30% H_2-air). At the initial stages, the flame remains nearly hemispherical. In the last frame, however, the flame begins to rise. The transition is characterized by the presence of a clear mushroom-like shape.

For even leaner mixtures characterized by smaller flame speeds, the buoyancy effects begin to play a role at smaller scales. Figure 4.4 shows the flame dynamics in a 8.9% H_2-air mixture. By the second frame, the flame has detached from the bottom wall. The flame then continues to rise and deform, taking an elongated pancake-like shape in the fourth frame, which was taken just before the bubble bursts. The elongation of the flame shows that the bubble constrains the flame motion somewhat as the flame approaches the top boundary of the bubble. Disturbances were observed on the flame surface when the bubble film breaks. These disturbances than grew at later times, as shown in the sixth frame of Figure 4.4.

Further reduction in the hydrogen content permitted us to obtain buoyancy-affected flames at much smaller scales. Figure 4.5 shows the dynamics of the flame in a 7% H_2-air mixture. By the first frame shown, the flame has already nearly detached from the bottom plate. The subsequent frames illustrate the rise of the flame and its elongation as it approaches the top film surface. Interestingly, the flame is also smoother than in the slightly richer mixture. However, instabilities set in upon breaking of the soap film (frame 5), which then grow in subsequent frames. Note that again large portions of gas remain non-reacted during the event, as the buoyancy effects entrain the flame faster than the

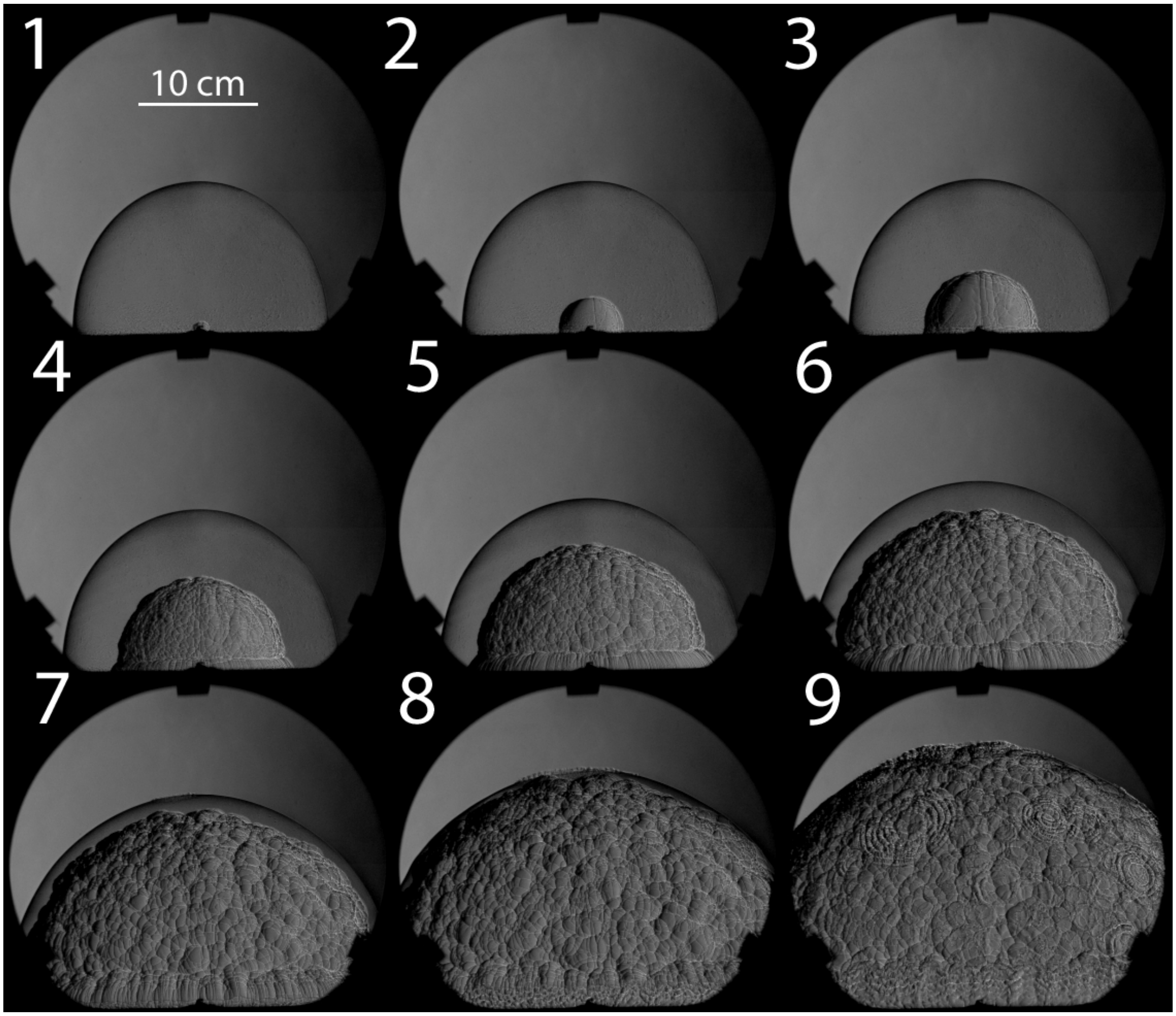

Figure 4.1: Frames from a 30% H_2-air, stoichiometric, mixture contained in a soap bubble (R = 12 cm); for reference, the field of view (diameter of luminous region) is 31.8 cm in diameter. Video recorded at 30,018 fps. The time interval between frames is 1.5 ms. The resolution is 512 x 512. The exposure time is 1 μs. The spark plug is at the bottom center of each frame.

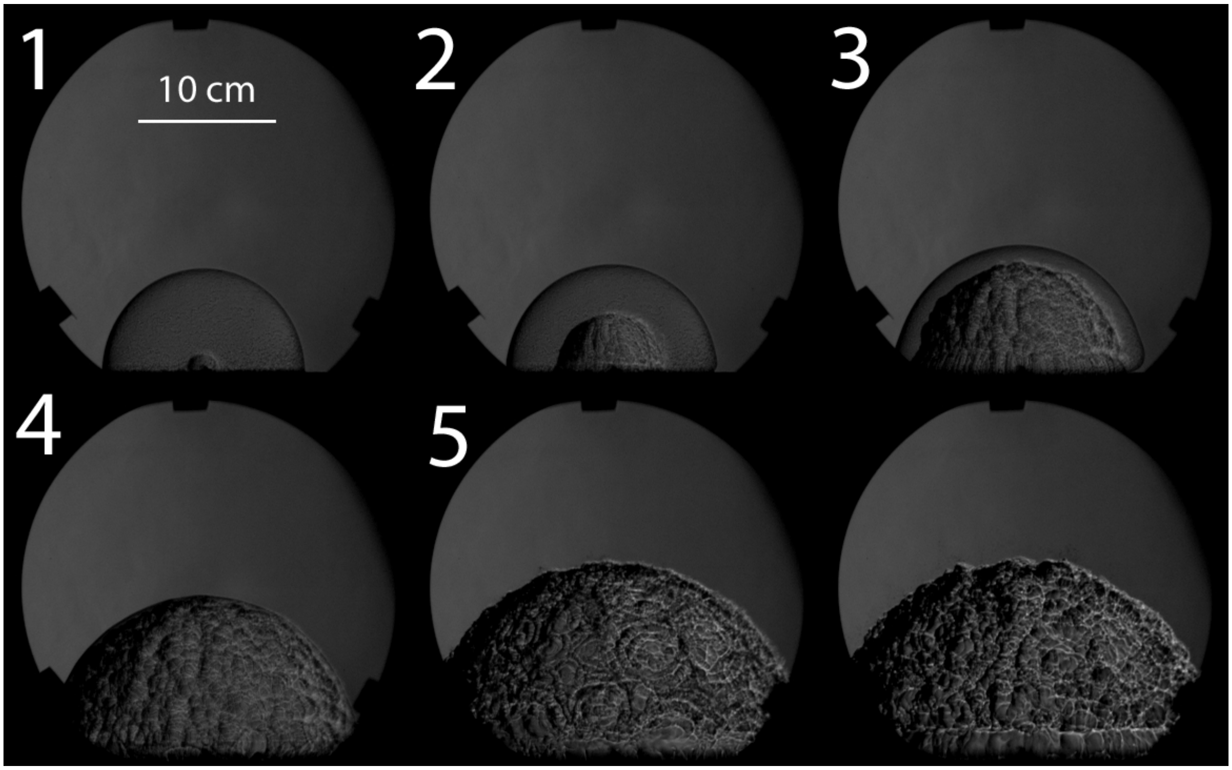

Figure 4.2: Frames from a 23% H_2-air mixture contained in a soap bubble ($R = 7.29$ cm) recorded at 16,000 fps. The time interval between frames is 3.75 ms. The resolution is 512 x 384. The exposure time is 1 μs.

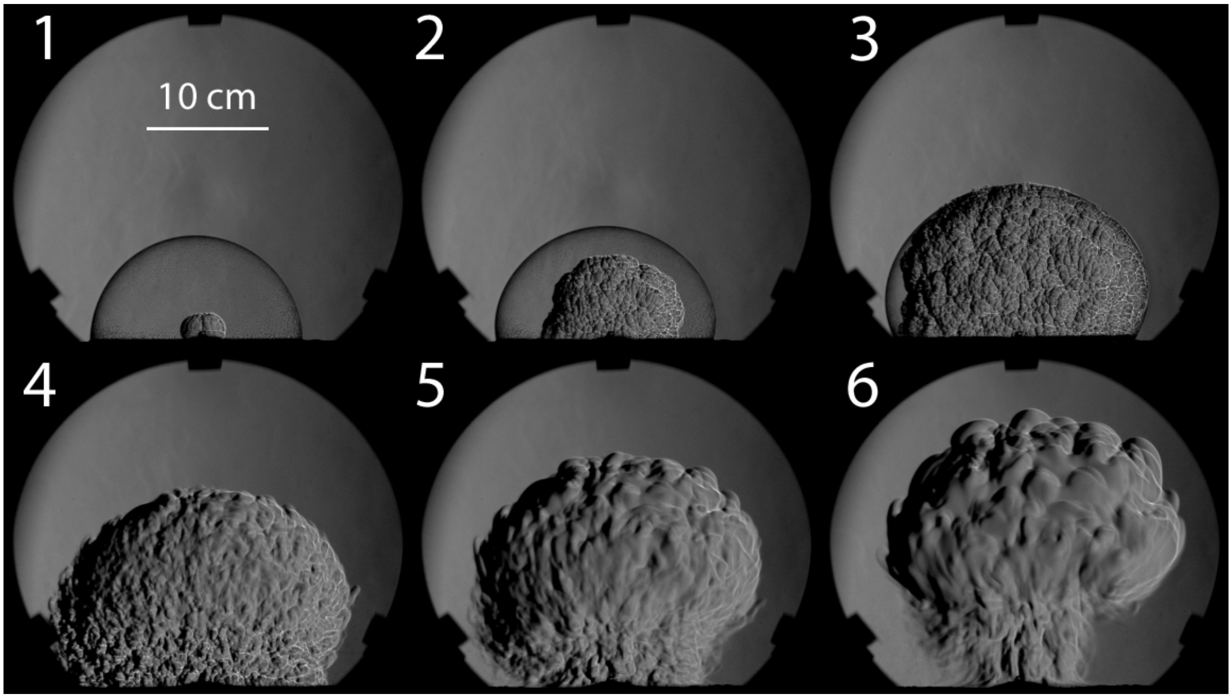

Figure 4.3: Frames from a 11.9% H_2-air mixture contained in a soap bubble ($R = 8.13$ cm) recorded at 30,018 fps. The time interval between frames is 44 ms. The resolution is 512 x 512. The exposure time is 1 μs.

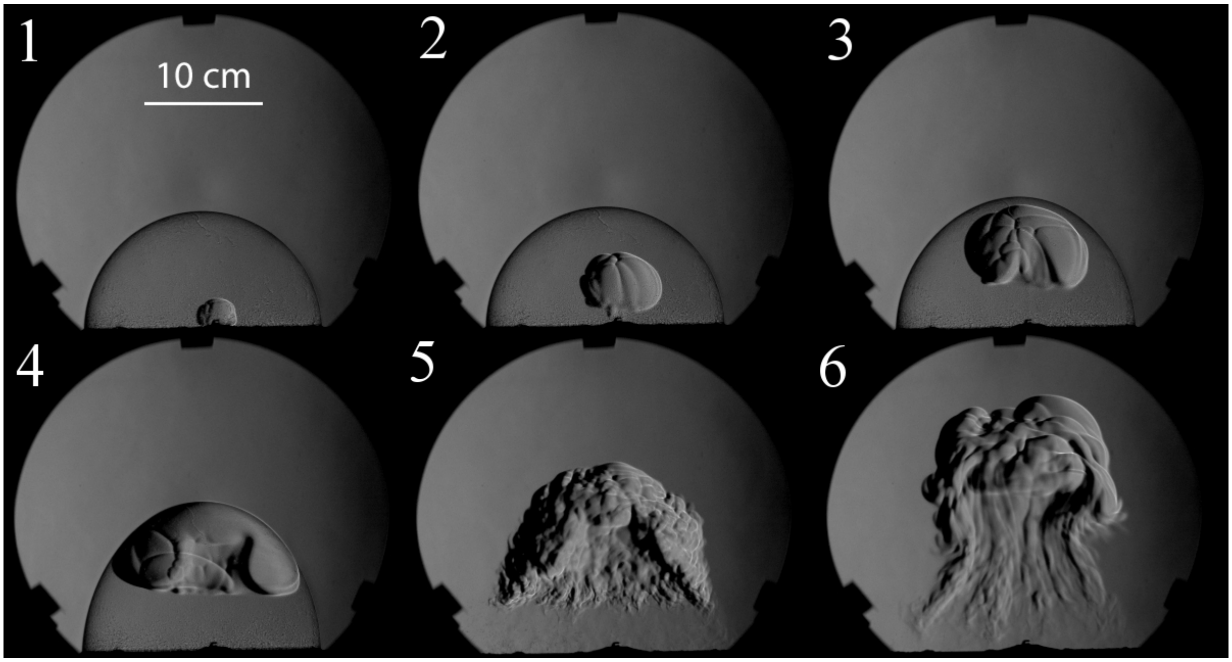

Figure 4.4: Frames from a 8.9% H_2-air mixture contained in a soap bubble ($R = 9.24$ cm) recorded at 30,018 fps. The time interval between frames is 93.1 ms. The resolution is 512 x 512. The exposure time is 1 μs.

flame can burn surrounding material.

In order to visualize the same phenomenon for 7% H_2-air mixture on a larger scale we used the shadowgraph system. Figure 4.6 shows a bubble of 31.12 cm in diameter filled with 7% H_2-air.

4.3 Laminar burning velocity measurements

We extracted the laminar burning velocity S_L from the video recordings. Continuity across the flame requires that the speed of the flame with respect to the stationary burned gases is

$$V_{burn} = \frac{\rho_u}{\rho_b} S_L \tag{4.1}$$

where ρ_b and ρ_u are the densities in the burned and unburned gases, respectively.

Our measurements of the laminar flame speed followed the usual technique of first determining the absolute velocity of the flame surface V_{burn}. The mean spatial velocity was obtained from a sequence of pictures. The time between the frames was determined from the framing speed (sample rate) of the camera. For a given mixture, the spatial velocity was determined by plotting the location of the flame front as a function of time and then calculating the slope. For lean mixtures, only the early frames steps (before the flame is detached) were considered for the measurements. The laminar flame speed was then obtained from V_{burn} using Eq. (4.1) and the calculated density ratio.

The density ratio was computed using the equilibrium solver available with the Cantera software, by requiring that the pressure and enthalpy be conserved in the gases. These are the common assumptions for a laminar flame. Figure 4.7 shows the variation of ρ_b/ρ_u with hydrogen concentration. From density variations alone, one would expect a weaker influence of buoyancy effects in lean mixtures.

Figure 4.8 shows the variation of flame speeds with hydrogen concentration. Our experimental data points are compared with previous measurements [30, 31, 32, 33, 34, 35, 36,

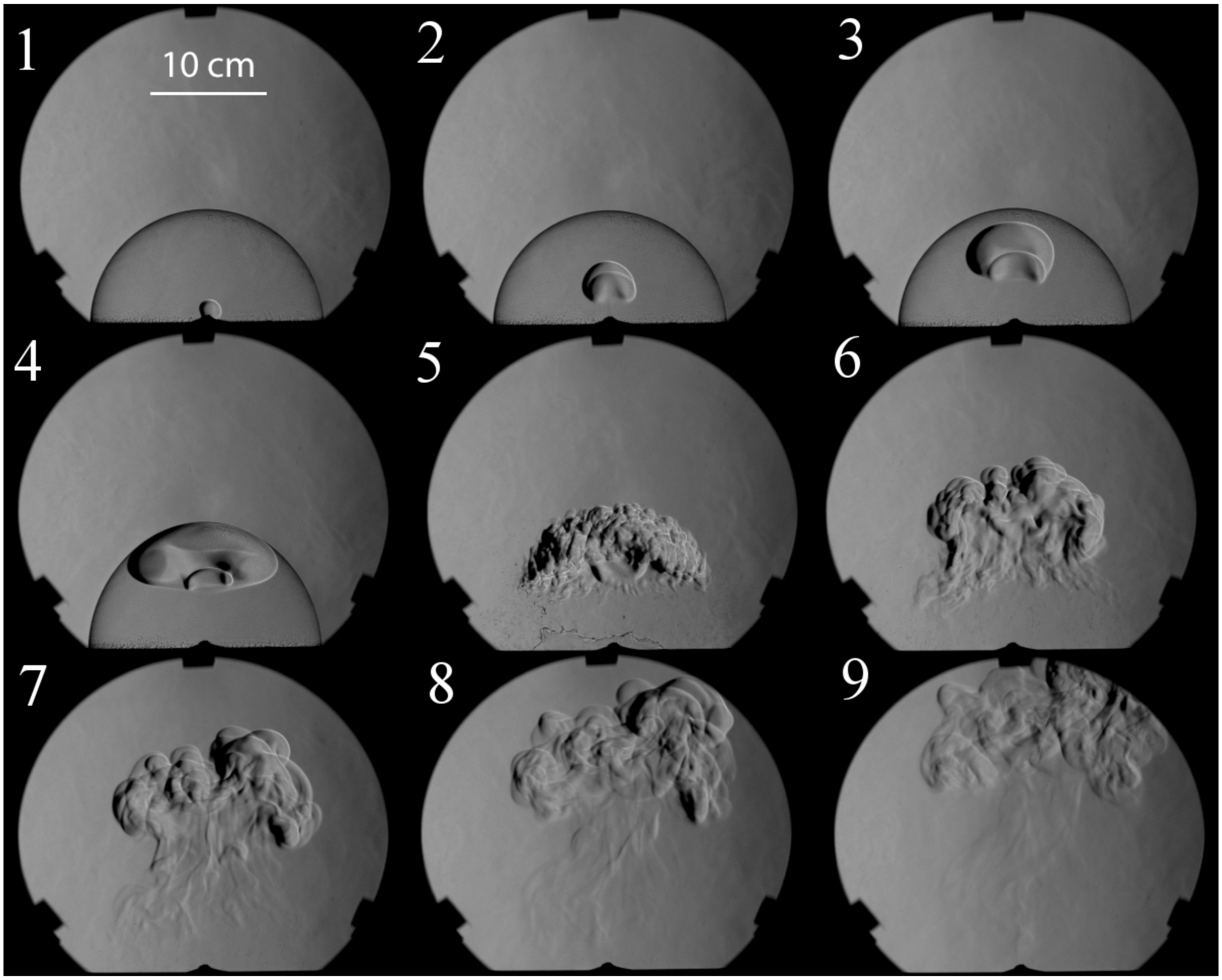

Figure 4.5: Frames from a 7% H_2-air mixture contained in a soap bubble (R = 9.26 cm) recorded at 5,000 fps. The time interval between frames is 100 ms. The resolution is 512 x 512. The exposure time is 1 μs.

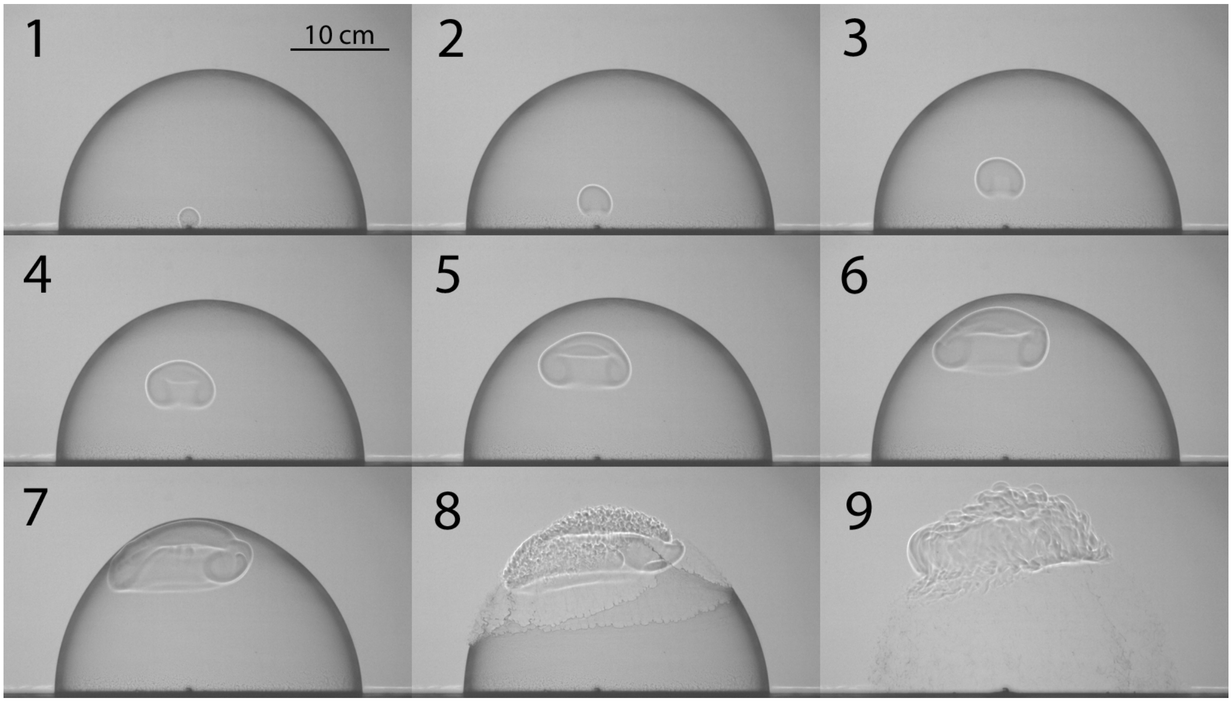

Figure 4.6: Frames from a 7% H_2-air mixture contained in a soap bubble ($R = 15.56$ cm) with large scale shadowgraph visualization recorded at 1,000 fps. The resolution is 1024 x 576. The exposure time is 1 μs. The time interval between frames is 66 ms.

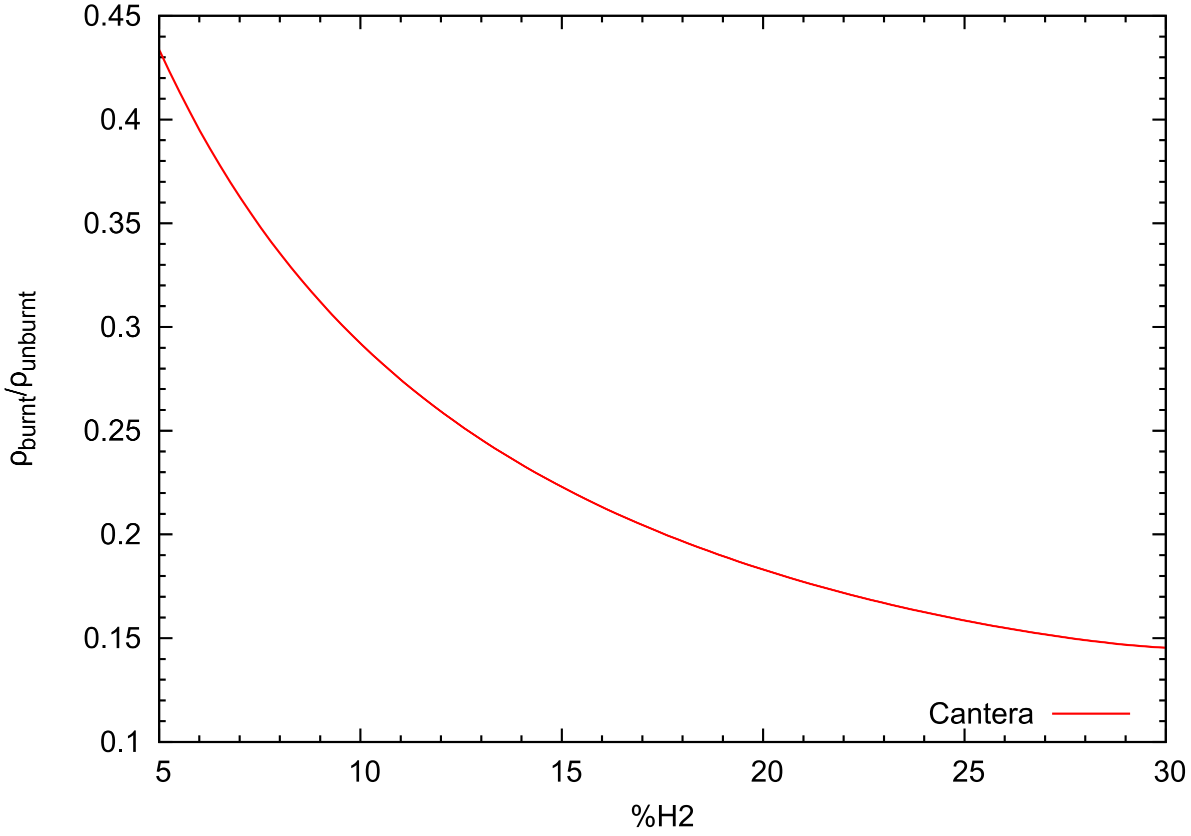

Figure 4.7: Variation of the density ratio in terms with hydrogen concentration obtained from equilibrium calculations.

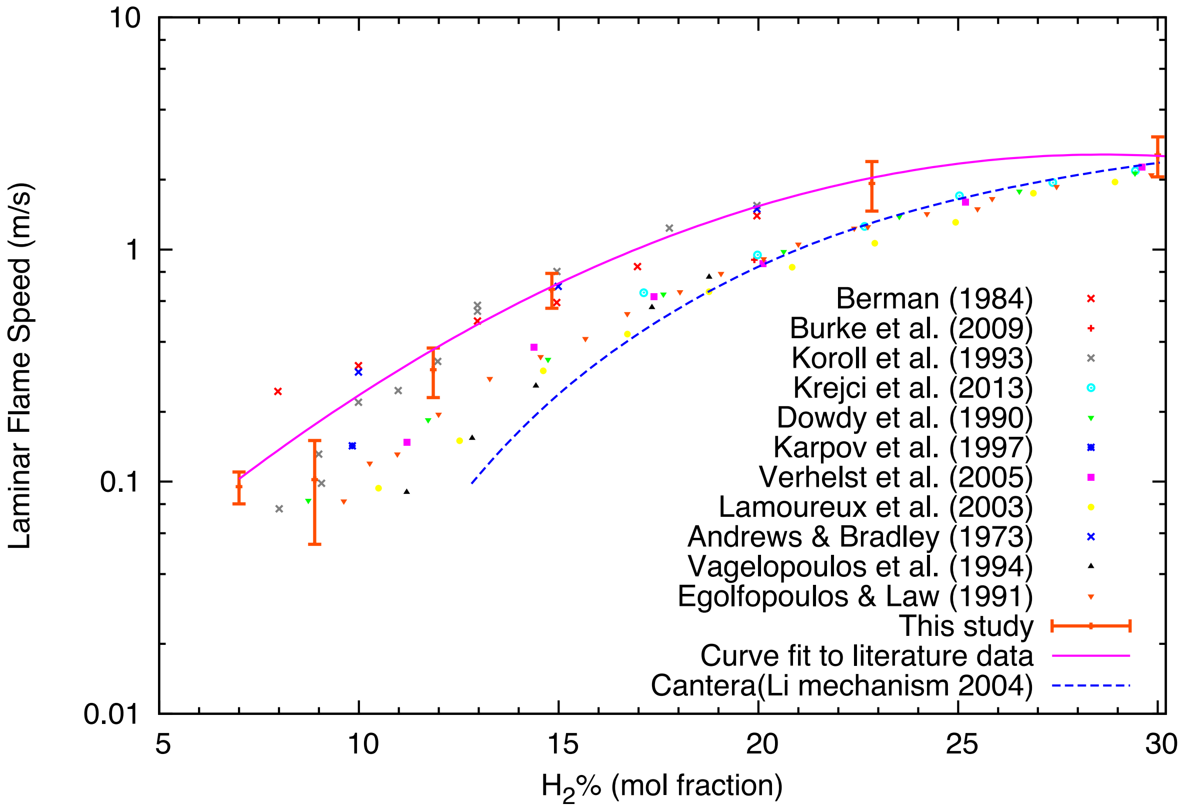

Figure 4.8: Variation of flame speeds with hydrogen concentration; experimental data points are compared with previous measurements [30, 31, 32, 33, 34, 35, 36, 37, 38, 39, 40] and calculations of the laminar flame speed using the Li et al. kinetic mechanism [41].

37, 38, 39, 40] . As can be seen from Fig. 4.8, our measurements of flame speed are in good agreement with published data, particularly with the measurements of Koroll et al. [30]. Also shown in Fig. 4.8 are our calculations of the laminar flame speed using the Li et al. chemical kinetic mechanism [41] (containing 19 elementary chimical reactions and 11 species). These calculations were performed with the Cantera package, assuming mixture averaged transport properties. The predictions somewhat underestimate our experimental values and those of Koroll et al. We believe this discrepancy is due to the fact that the simulations do not take into account the stretch effects, which tend to give rise to higher flame speeds in lean radially expanding of flames hydrogen-air [23]. Most of the other data include the corrections for the effects of stretch.

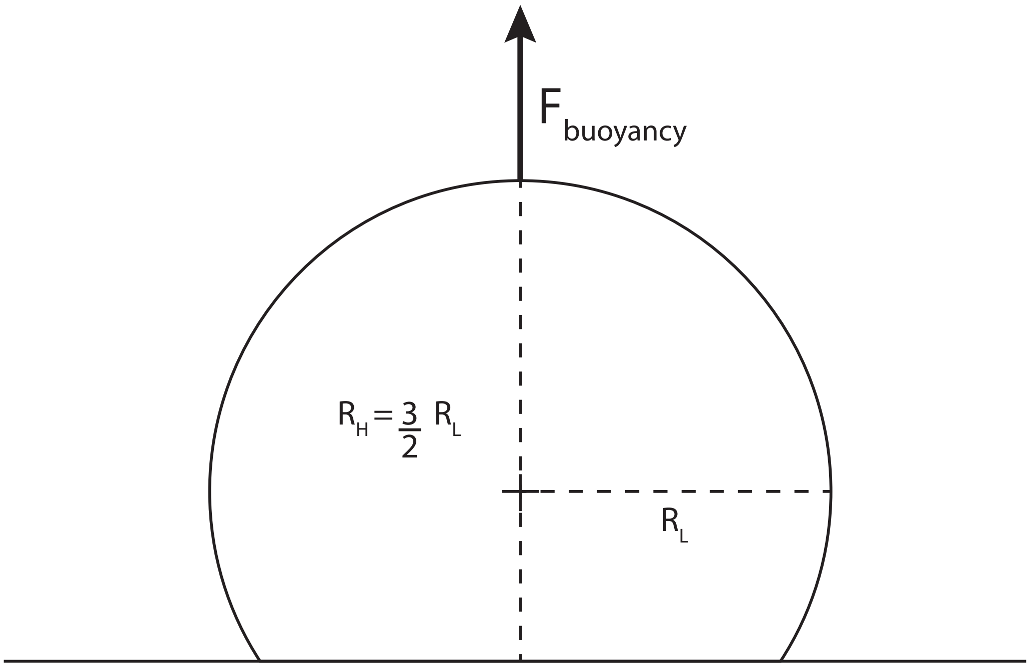

Figure 4.9: Definition of R_{switch} as the flame radius when the flame has lifted by half this radius.

4.4 The critical radius of buoyant flames

4.4.1 Critical radius measurements

To quantify the buoyancy effect experimentally, we defined in our study R_{switch} as the radius of the flame at which buoyancy starts playing an important role. We define this radius as the radius of the flame when buoyancy has displaced the flame kernel upwards by 50% of the flame radius, as illustrated in the Fig. 4.9 ($R_{switch} = R_L$). Given the size of the bubbles used in the tests (limited to tens of centimeters), we could only estimate the actual critical radius for relatively lean mixtures, below 12% H_2-air. The measured critical radii are shown in Figure 4.10.

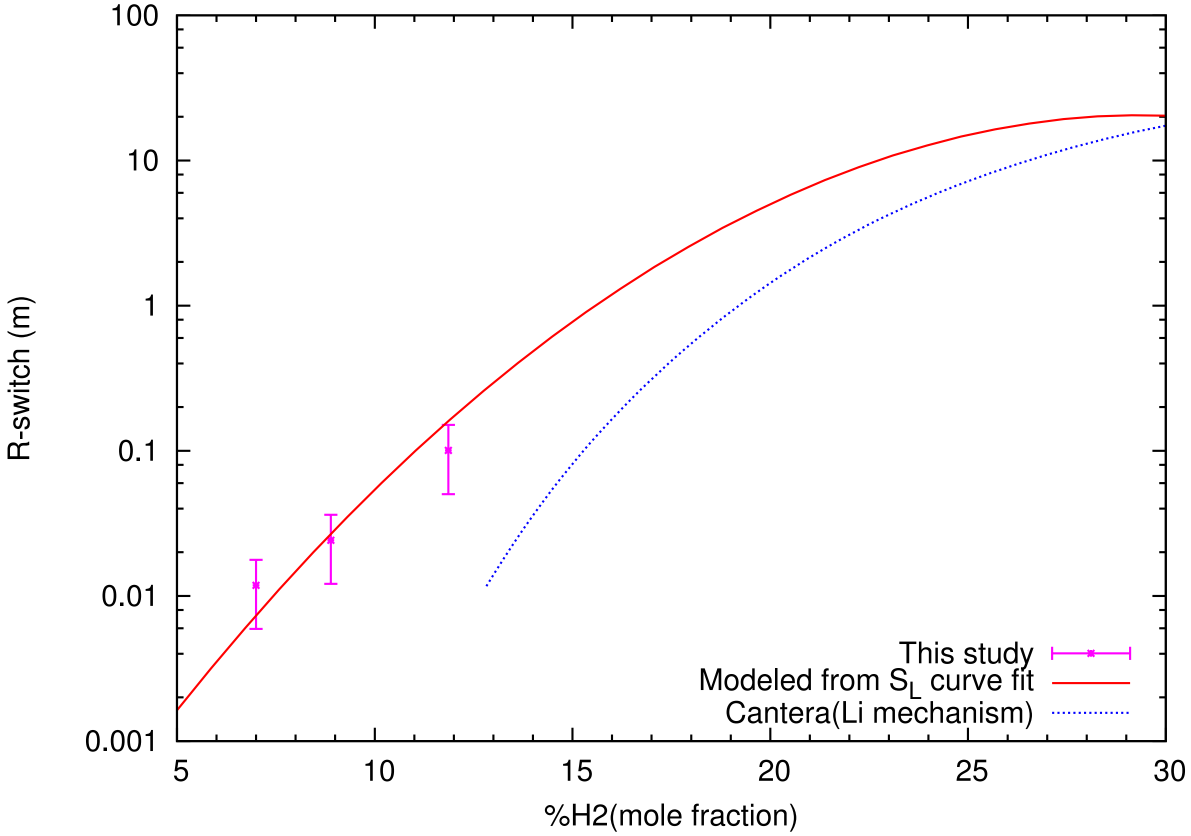

Figure 4.10: Variation of the critical radius R_{switch} above which a flame kernel will be affected by buoyancy; the two predictions are made based on the measured flame speed, and on the flame speed calculated for a stretch-free flame.

4.4.2 Prediction of the critical radius of buoyant flames

The critical radius of buoyant flames defined above, R_{switch}, can be estimated a priori by considering the two time scales of the phenomena responsible for flame motion, i.e. combustion and buoyancy. The time scale for the flame to grow to a characteristic dimension R is

$$t_{burn} = \frac{R}{V_{burn}} \tag{4.2}$$

Based on Eq. (4.1), it becomes

$$t_{burn} = \frac{R}{S_L}\frac{\rho_b}{\rho_u} \tag{4.3}$$

The time scale for the buoyant force to displace the flame bubble a characteristic distance *R/2* can be obtained from simple physical arguments, following a similar treatment as Zingale and Dursi [25]. The speed at which a flame bubble is convected upwards can be estimated from the classic work of Davies and Taylor [42], who investigated the speed at which gas bubbles of approximately hemispherical shape rise in a liquid. This motion is due to the competition between the buoyancy force, $2/3\pi R^3(\rho_u - \rho_b)g$ and the drag force. Since drag for such rising bubbles is due mainly to pressure drag in inviscid flow, the drag is simply proportional to the characteristic dynamic pressure $1/2\rho_u {V_{rise}}^2$, the projected surface area of the flame bubble, πR^2, and the drag coefficient C_D. The drag coefficient resulting from Davies and Taylor [42] for hemispherical bubbles is 3. Equating the two forces, the characteristic rise speed of the bubble is obtained, differing from the result of Davies and Taylor [42] by the density ratio, which is non-negligible in the case of combustion, since the burned gas density cannot be neglected as compared to that of the unburned gas.

$$V_{rise} = \frac{2}{3}\sqrt{Rg\left(1 - \frac{\rho_b}{\rho_u}\right)} \tag{4.4}$$

The characteristic time scale for buoyancy effects thus becomes $t_{rise} = \frac{R}{2}/V_{rise}$. The ratio of the characteristic time scales of burning and buoyancy yields:

$$\theta = \frac{t_{burn}}{t_{rise}} = \frac{4}{3}\frac{1}{S_L}\frac{\rho_b}{\rho_u}\sqrt{Rg\left(1-\frac{\rho_b}{\rho_u}\right)} \tag{4.5}$$

The buoyant regime is expected when $\theta >> 1$ and the non-buoyant regime when $\theta << 1$. Alternatively, a critical flame radius R_{switch} can be defined when the two time scales are equal. Setting $\theta = 1$ yields:

$$R_{switch} = \frac{9}{16}\frac{{S_L}^2}{g}\left(\frac{\rho_b}{\rho_u}\right)^{-2}\left(1-\frac{\rho_b}{\rho_u}\right)^{-1} \tag{4.6}$$

As the flame grows from a small radius, buoyant forces will have no influence until $R \simeq R_{switch}$.

It is worthwhile to compare our predictions based on the previous scaling laws established for the effect of buoyancy in flame propagation. Traditionally, it is the Froude number, given by Eq. (4.7), that is used to establish whether buoyancy plays a substantial role. The buoyancy effects are considered to dominate over the process of flame expansion when the Froude number is small, and estimated to be $Fr < Fr^* = 0.11$ [43]. We note first that the time scale ratio defined in equation (4.5) can thus be interpreted as a modified inverse (square root of) Froude number. Furthermore, the empirical value given to the critical Froude number in the past depends on the expansion ratio.

$$\begin{aligned} Fr &= \frac{{V_{burn}}^2}{2gR} \\ &= \frac{{S_L}^2}{2gR}\left(\frac{\rho_u}{\rho_b}\right)^2 \end{aligned} \tag{4.7}$$

The criterion derived in the present study, based on the arguments of Zingale and Dursi, can now be compared with the experiments illustrated above. The evaluation of R_{switch} was made using the laminar flame speed (S_L) and density ratio ρ_b/ρ_u data presented above.

The variation of the critical radius with hydrogen concentration is shown in Fig. 4.10. The two curves correspond to the predictions made using the Cantera prediction made without accounting for flame stretch, and a correlation of the flame speed of our measurements and those of Koroll et al. [30], reported in Fig. 4.8. Figure 4.10 also shows our measurements of R_{switch} taken directly from the high-speed videos when the flame sphere starts detaching from the bottom wall; the prediction made with account for stretch effects is found in excellent agreement with the experimental values, while the prediction made without the account of stretch underestimates the critical radius at which buoyancy begins playing a substantial role.

For the range of parameters investigated, the predictions for R_{switch} further demonstrate the strong sensitivity of this length scale on hydrogen concentration. At near stoichiometric conditions (30% H_2), terrestrial flames will begin to be affected by buoyancy effects when they reach a radius of tens of meters. Near 10% hydrogen, however, flames on the order of a few centimeters will begin to be affected. This is in excellent agreement with our experiments.

4.5 Conclusion

The results presented in this chapter thus illustrate the role played by buoyancy on the dynamics of unconfined flames. The soap bubble technique permitted us to observe these dynamics over length scales of tens of centimeters. Buoyancy effects become important when the flame is sufficiently weak, such that the flame speed evolves on time scales longer than buoyancy. Simple scaling laws were made for the critical flame dimension beyond which the flame sphere motion becomes buoyancy dominated. The scaling laws were found in excellent agreement with the experimental measurements.

Chapter 5

Two bubble tests

This chapter reports the experimental results obtained with two hemispherical bubbles separated by air.

5.1 Test configuration and conditions

The separated pockets of reactive mixture were obtained using the soap bubble technique. We filled two hemispherical soap bubbles with hydrogen-air mixture, aligned on a flat plastic sheet (as shown in Fig. 5.1). The two bubbles were created side by side with the desired spacing and individual dimensions. A spark plug was placed in the center of the first bubble to ignite the reactive mixture. The experiments monitored if the flame successfully spread from the ignited pocket to the other pocket.

For these series of tests, the experiments were performed with four different gas concentrations: a near stoichiometric mixture of 30% H_2 and leaner mixtures of 20% H_2-air, 15% H_2-air and 11% H_2-air. Details on these series of tests are available in the Appendix B.

The visualization system used was the large-scale shadowgraph system. The video's frame rate varied between 3,000 frames per second (fps) for the stoichiometric mixture to 1,000 fps for the 15% H_2-air and 11% H_2-air concentrations. The resolution of the videos

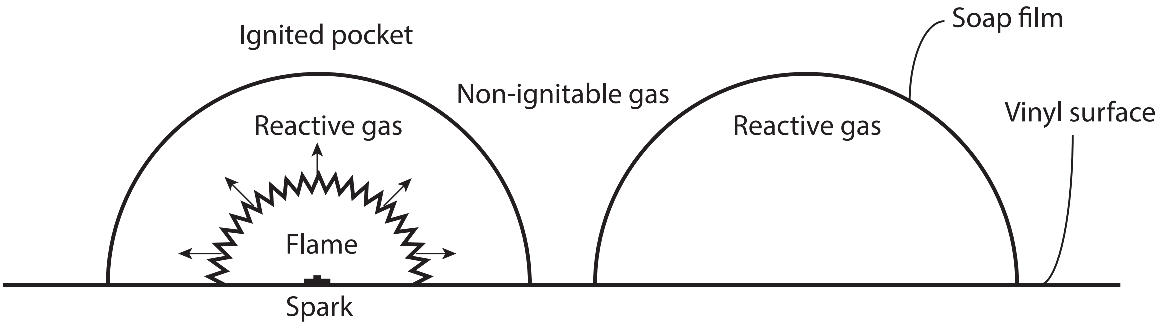

Figure 5.1: Illustration of the two reactive pockets.

was set to 1280 by 800 pixels. The initial radii of each bubble, R_1 and R_2 respectively, were varied between 0.02 and 0.15 m. In a second part of these series, experiments were conducted without the soap film of both bubbles in order to determine if the soap film plays a significant role in the transition criteria from one bubble to the next. The film burst and the ignition was triggered sequentially with an approximate time delay of 100 ms. All the tests were performed at room temperature and atmospheric pressure with minimal ventilation.

5.2 Experimental results

5.2.1 Experiments with the soap film

Stochiometric H_2-Air

Figure 5.2 and Fig. 5.3 illustrate the dynamics of a stoichiometric hydrogen-air flame. The bubble film was not ruptured prior to ignition. For the stoichiometric concentration, the flame is hemispherical and takes on a cellular structure. This deflagration wave consumes the gas while the products expand and the soap bubble grows. Upon rupture of the soap film, the second bubble may ignite if sufficiently close to the first. The ignition of the second bubble was generally observed near the sheet surface, presumably in the gas left behind at the foot of the boundary layer of the gases of the second bubble.

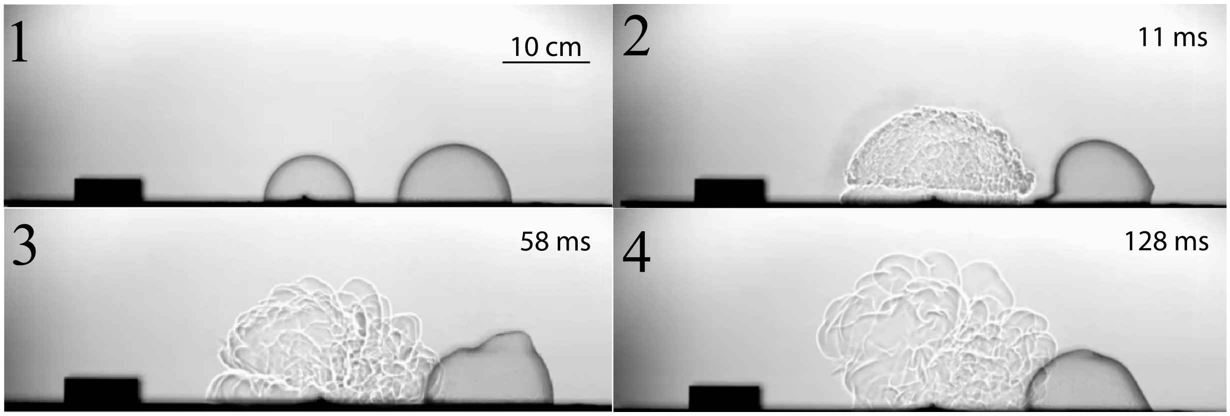

Figure 5.2: Shadowgraph images of stoichiometric hydrogen-air deflagrations recorded at 12,251 fps. The resolution is 1024 x 512. The exposure time is 1 μs. The field of view is 22.4 cm tall. No ignition of the second bubble. $R_1 = 5.43$ cm, $R_2 = 6.54$ cm, $D = 4.75$ cm.

Figure 5.2 shows an example of a failed propagation event. As the first flame grew, it generated a flow movement of the second bubble, which was displaced toward the right. The shape of the bubble was also disturbed, as shown in the third frame. For this particular geometry of the bubbles and the distance between them, the flame did not reach the second reactive pocket.

Figure 5.3 illustrates a successful propagation of the flame from the first bubble to the second. Disturbances were observed on the flame surface when the first bubble film broke. The flame front reached the second bubble in the third frame. The flame started igniting the reactive gas inside the second bubble only when the soap film broke as seen in the seventh frame.

The regimes of successful and unsuccessful flame propagation to the second bubble were obtained by varying R_1, R_2 and D. The results obtained for the stoichiometric mixture are shown in Fig. 5.4. The transmission limit appears to be well correlated with the distance that the first bubble needs to travel to reach the initial position of the gases in the second bubble, which are left behind in the boundary layer.

The difference between the final radius of the flame defined as R_1^* and the initial radius

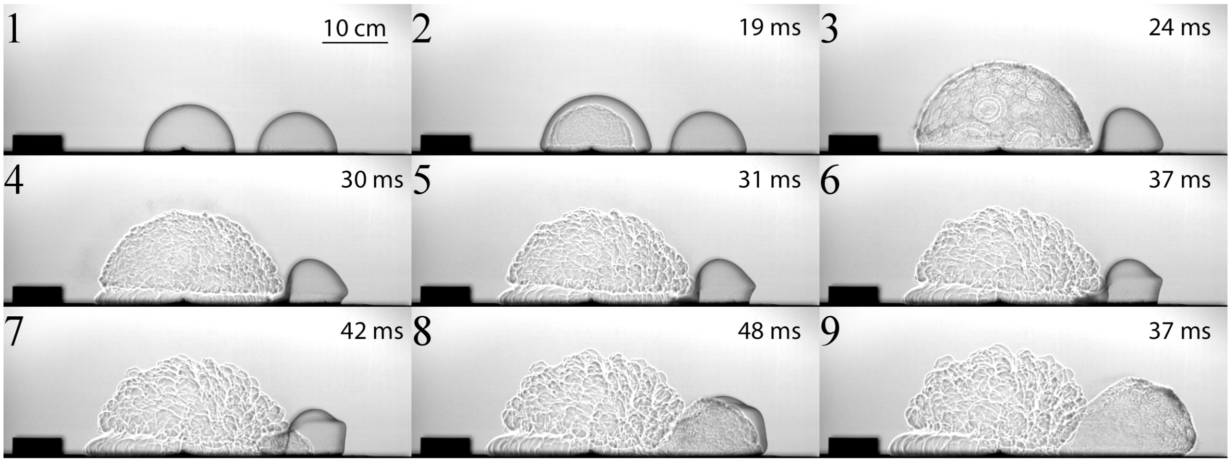

Figure 5.3: Shadowgraph images of stoichiometric hydrogen-air deflagrations recorded at 12,251 fps. The resolution is 1024 x 512. The exposure time is 1 μs. The field of view is 22.4 cm tall. Ignition of the second bubble. $R_1 = 7.71$ cm, $R_2 = 6.15$ cm, $D = 3.51$ cm.

R_1 should be proportional to the separation distance D and the transmission condition can thus be correlated by:

$$R_1^* - R_1 = D \tag{5.1}$$

The final radius R_1^* could be calculated using the expansion ratio of the mixture ρ_u/ρ_b. This gives:

$$\frac{R_1^*}{R_1} = \left(\frac{\rho_u}{\rho_b}\right)^{1/3} \tag{5.2}$$

The condition can thus be correlated by:

$$\begin{aligned} \frac{D}{R_1} &= \frac{(R_1^* - R_1)}{R_1} \\ &= \left(\frac{\rho_u}{\rho_b}\right)^{1/3} - 1 \end{aligned} \tag{5.3}$$

This limit depends solely on the expansion ratio of the combustible mixture. Since the expansion ratio for stoichiometric H_2-air mixture is ~ 7, the results indicate a limit of R_1/D=1.11. This limit offers a fairly good correlation, as can be seen in Fig. 5.4.

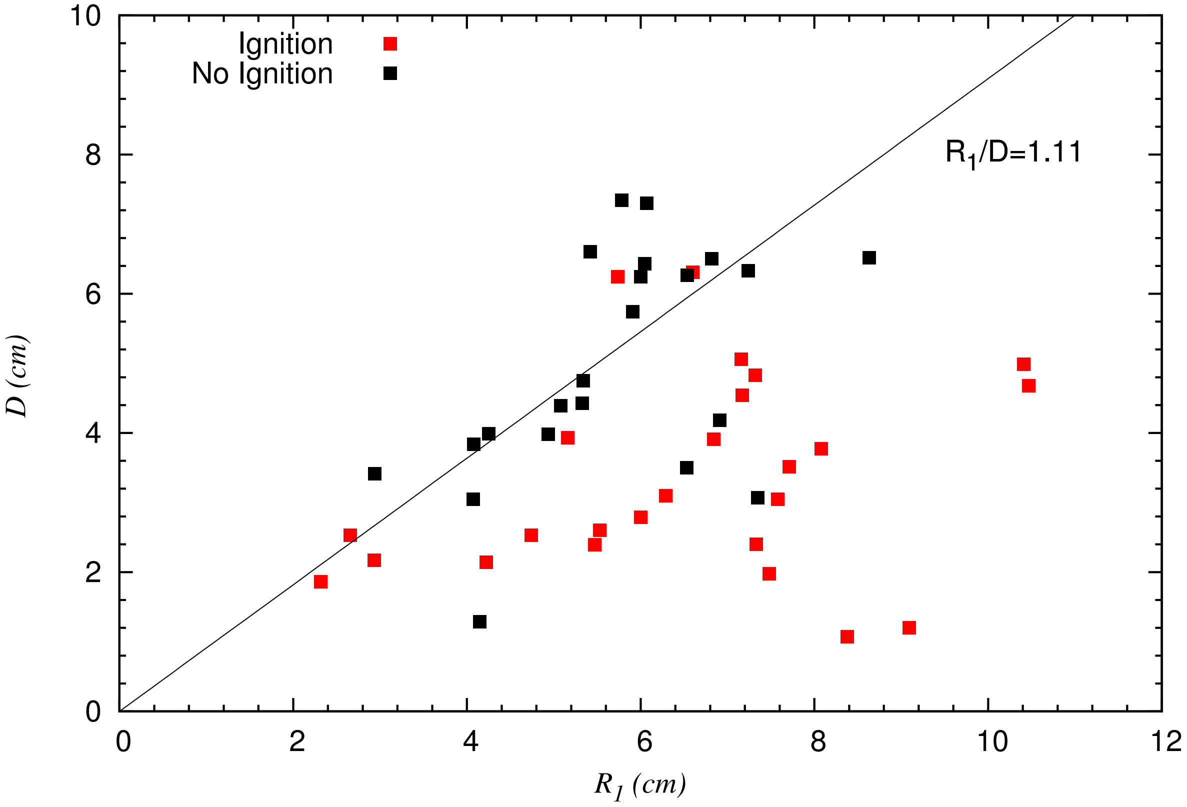

Figure 5.4: Propagation condition between two pockets of stoichiometric hydrogen-air mixture.

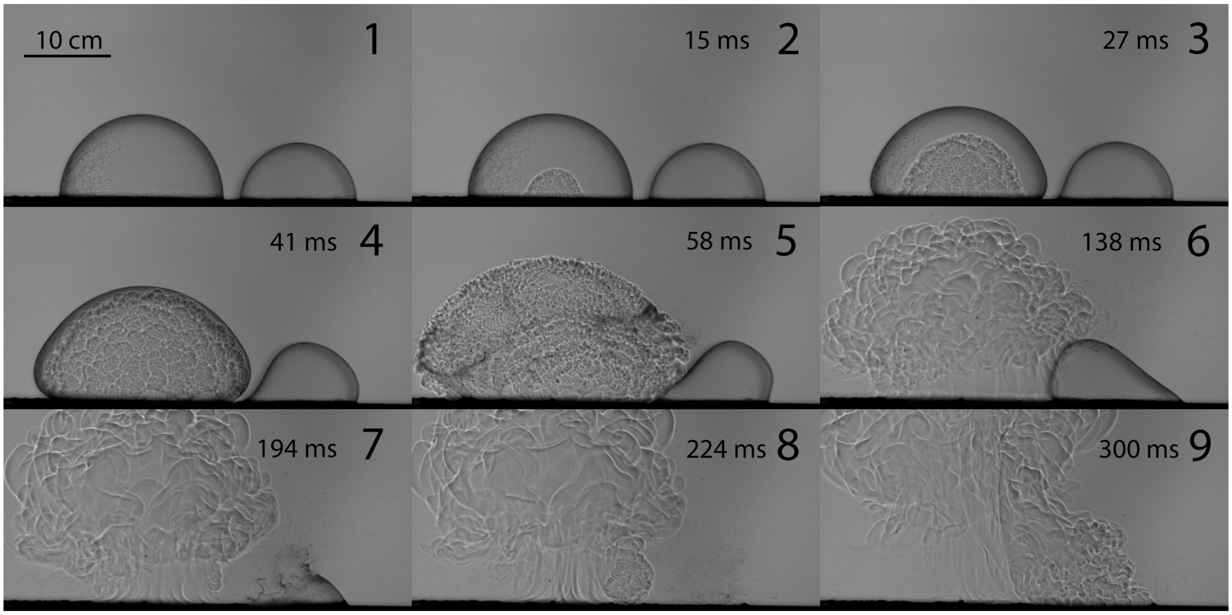

Figure 5.5: Shadowgraph images of 15% H_2-air deflagrations recorded at 3,200 fps. The resolution is 1280 x 800. The exposure time is 1 μs. Ignition of the second bubble. $R_1 = 8.59$ cm, $R_2 = 6.30$ cm, $D = 1.75$ cm.

Experiments with 15% H_2-Air

Figure 5.5 shows selected frames of an experiment with an initial mixture composition of 15% H_2-air. The flame speed in this case was much lower (experimental value: 0.67 m/s). At the initial stages, the flame remains nearly hemispherical. In the sixth frame, however, the flame begins to rise. The transition is characterized by the presence of a mushroom-like shape. As the flame was rising, the soap film of the second reactive pocket burst in the seventh frame. The lower part of the flame succeeded to reach and ignite the unburned gas of the second bubble. The new portion of flame propagates further even after the big part of the burnt gas has already risen far from the surface (see ninth frame).

The expansion ratio for 15% H_2-air mixture is ~ 4.5. Based on Eq. (5.3), the propagation limit determined by the expansion ratio is $R_1/D = 1.52$ as shown on Fig. 5.6. The video illustrated in Fig. 5.5 has a ratio of $R_1/D = 4.91$ which is more important than the limit 1.52. An analysis built on the expansion ratio for 15% H_2-air mixture would certainly predict a successful propagation for the configuration of Fig. 5.5 as it is the case

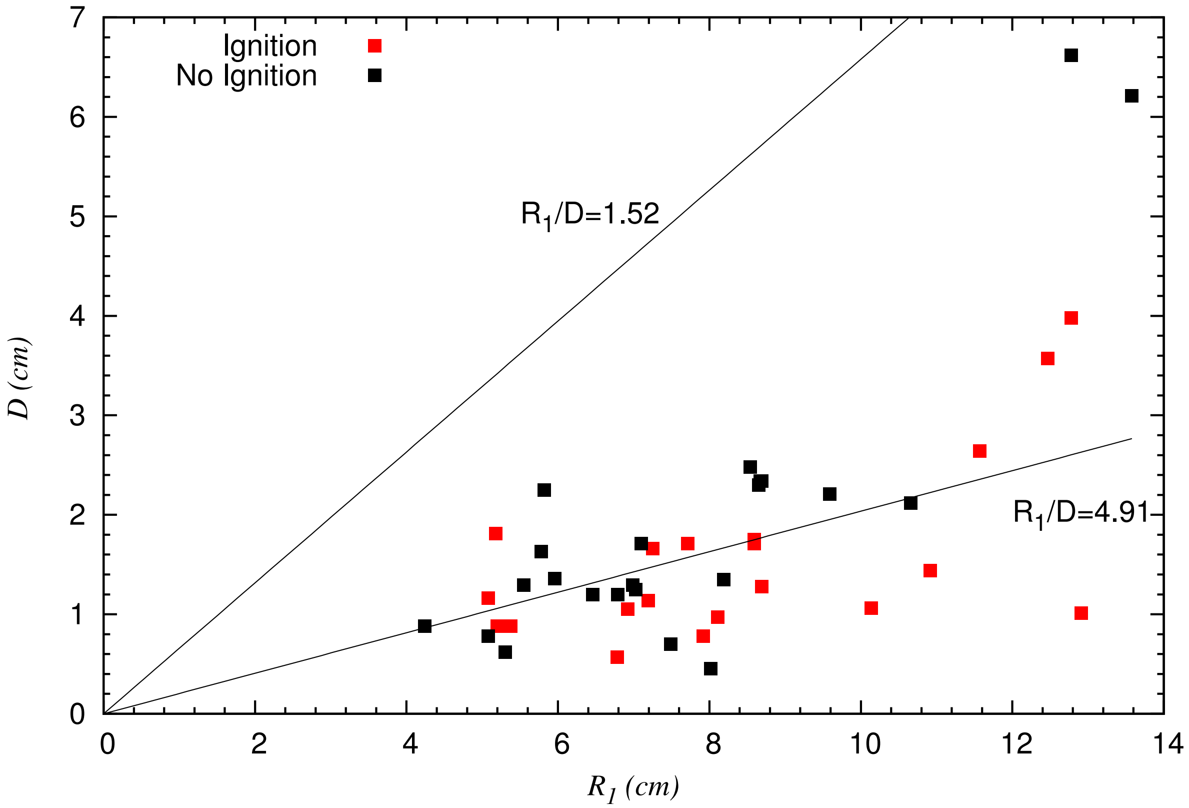

Figure 5.6: Propagation condition between two pockets of 15% H_2-air mixture.

here. However, the video illustrates a test with critical conditions of propagation. The propagation limit found with the expansion ratio is lower than the measurement results. The expansion ratio is not the only physical mechanism involved in the flame propagation conditions between the bubbles. In fact, most of the experiments conducted with the 15% H_2-air composition did not lead to ignition of the second bubble. The inability of the second bubble to ignite in this mixture is attributed to the buoyant effect operating on the first flame, which accelerates the flame kernel upward before heat and mass transfer originating from it can reach the second bubble, as observed from the high speed videos. Thus, the propagation criterion based on the volumetric expansion of burned gases for lean mixtures does not provide a realistic prediction. The buoyancy forces play a role on the flame dynamics for this concentration.

Experiments with 11% H_2-Air

In order to further investigate the effects of buoyancy on the likelihood of the flame to propagate in leaner mixtures, experiments were conducted with a leaner mixture of composition 11% H_2-air. A test with the radius of the first bubble R_1=6.9 cm (illustrated in Fig. 5.7) and one test with a larger radius R_1=13.4 cm (see Fig. 5.8) were performed. Those tests were conducted with the soap film and the heating wires shown beside the bubbles were not triggered. Comparing the third frame in Fig. 5.7 with frames 3 and 4 in Fig. 5.8, we see the second bubble shape more deformed in the case where the size of the ignited bubble is larger. The lift of the ignited bubble causes the movement of the second bubble. The faster the first pocket rises, the more the second pocket swings. The lift of the ignited bubble is driven by the buoyancy forces. The buoyancy effects are more significant when the radius of the reactive pocket becomes larger, thus the tendency of the flame to propagate is less likely for a larger radius than for a smaller one.

Further reduction in the hydrogen content permitted us to obtain buoyancy-affected flames at much smaller scales. For those concentrations the propagation was impossible. In fact, in the earlier frames the flame detaches from the bottom plate as the buoyancy effects entrain the flame faster than the flame can burn surrounding material. No ignition was observed for the second bubble for all the tests performed with 11% H_2-air mixtures, irrespective of how arbitrarily close the two bubbles were positioned.

5.2.2 Experiments without the soap film

Experiments with stochiometric H_2-Air

Figure 5.9 and Fig. 5.10 show tests of successful and unsuccessful transmission of the flame at different geometrical configurations when the soap film was broken before ignition. Comparing the limits of the flame expanding in the sixth frame to the initial position of the second pocket in the second frame above in the Fig. 5.9, we can easily estimate that the flame reached the second reactive gas while expanding. As the soap film does not confine the reactive gas anymore, it has more freedom to shift as it is pushed by the expansion of

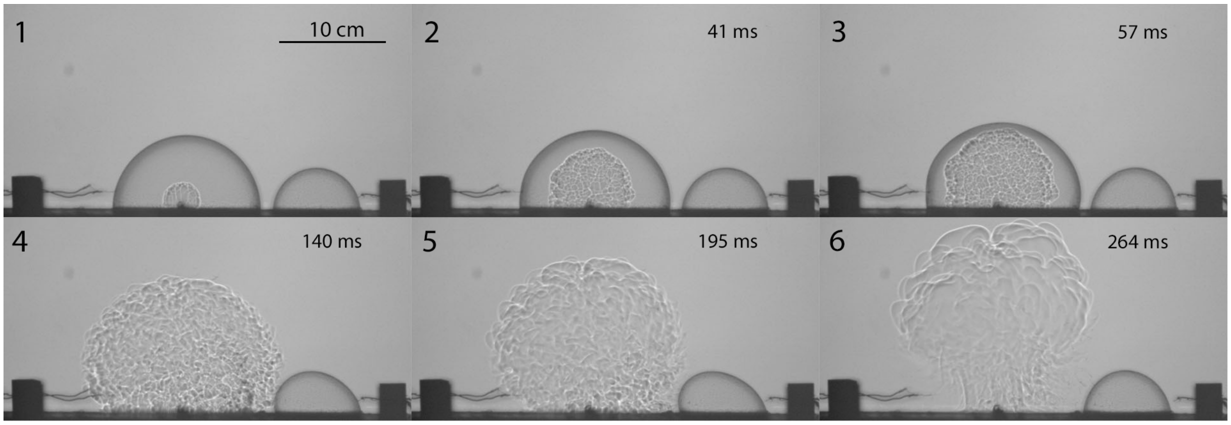

Figure 5.7: Shadowgraph images of 11% H_2-air deflagrations recorded at 1,000 fps. The resolution is 1280 x 800. The exposure time is 8 μs. No ignition of the second bubble. R_1 = 6.90 cm, R_2 = 3.84 cm, D = 1.11 cm.

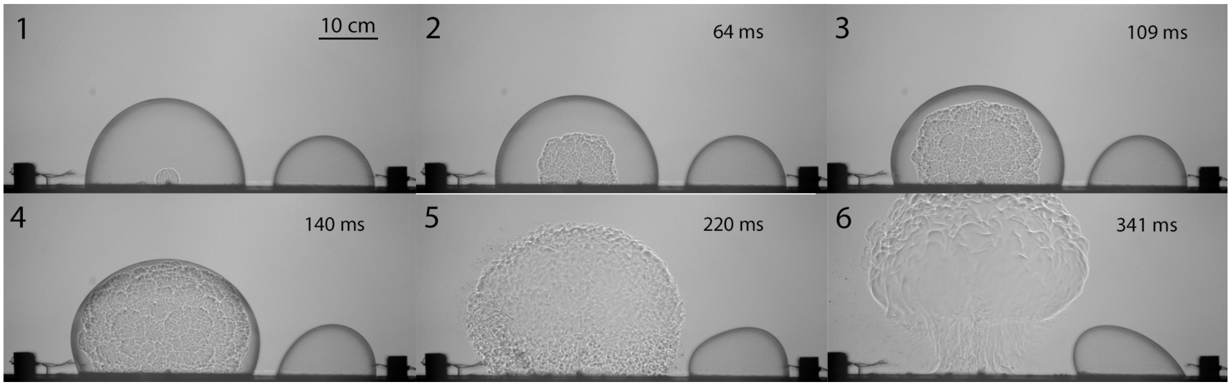

Figure 5.8: Shadowgraph images of 11% H_2-air deflagrations recorded at 1,000 fps. The resolution is 1280 x 800. The exposure time is 8 μs. No ignition of the second bubble. R_1 = 13.41 cm, R_2 = 8.86 cm, D = 4.84 cm.

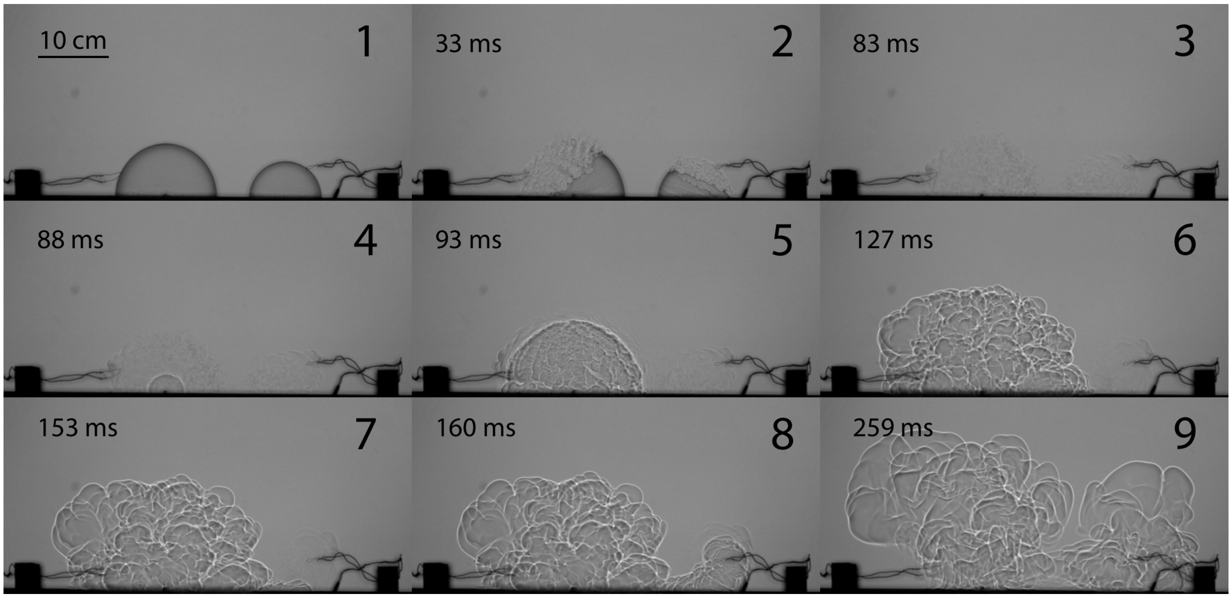

Figure 5.9: Shadowgraph images of stoichiometric hydrogen-air deflagrations without soap film recorded at 3,000 fps. The resolution is 1280 x 800. The exposure time is 8 μs. Ignition of the second bubble. $R_1 = 7.24$ cm, $R_2 = 5.00$ cm, $D = 4.54$ cm.

the first flame. In the seventh frame of the same figure, we see that the flame could survive and progressively propagate before reaching more portions of gas of the second bubble. The separation distances between the pockets were found to be minimally affected by the presence or absence of the soap film (see Fig. 5.15), although more scatter was apparent in the experiments. The invariance of the separation distance signifies that the transition mechanism is likely associated with the expanding gas of the first bubble reaching the gas left behind on the plate (in the boundary layer) by the second bubble.

Experiments with 20% H_2-Air

Figure 5.11 and Fig. 5.12 show selected frames of experiments with a mixture composition of 20% H_2-air without the soap film. Images were recorded with a free field of view due to technical issues with the arc lamp at the time of the tests. A black screen was placed between the bubbles and the retro-reflective screen to get a better contrast with the luminous flame. The flame transition is not clearly apparent on the images compared

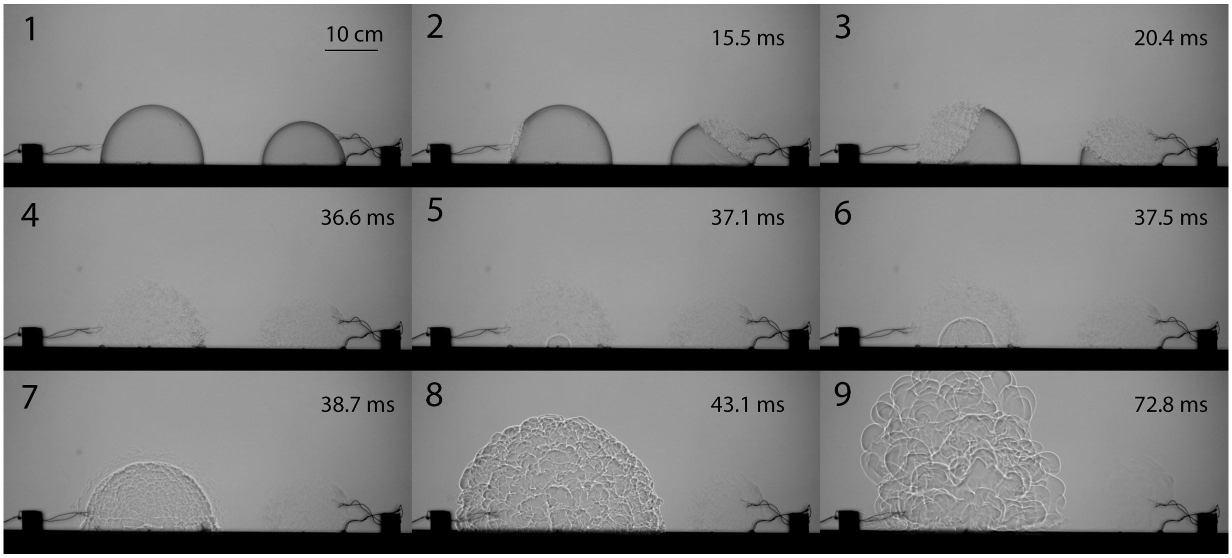

Figure 5.10: Shadowgraph images of stoichiometric hydrogen-air deflagrations without soap film recorded at 3,000 fps. The resolution is 1280 x 800. The exposure time is 8 μs. No ignition of the second bubble. $R_1 = 9.94$ cm, $R_2 = 7.68$ cm, $D = 10.55$ cm.

to the shadowgraph technique. Figure 5.11 shows a successful propagation of the flame to the next pocket and Fig. 5.12 illustrates a failed event, in which the flame from the ignited bubble did not reach the second pocket before it rose in the sixth frame. For all the 20% H_2-air tests, the results show similar behavior to the 30% H_2-air mixtures, but there is a slight decrease in the separation limit as shown in Fig. 5.14 and Fig. 5.15.

Experiments with 11% H_2-Air

Figure 5.13 shows the shadowgraph images of 11% H_2-air. This figure shows clearly the impact of the soap film being burst with the wires from the side. Indeed, beyond the fact that the bubble was initially well centered over the spark, we see in the third and fourth frames that the flame was displaced to the left side (the side where the bubble first failed) and is not centered anymore. This should affect the propagation of the flame to the right side towards the second bubble. The gas inside the bubble is at slightly higher pressure than the atmosphere. When the soap film is burst the gas is preferentially expelled from the bubble at the location where it first opens. Since no propagation was observed in any

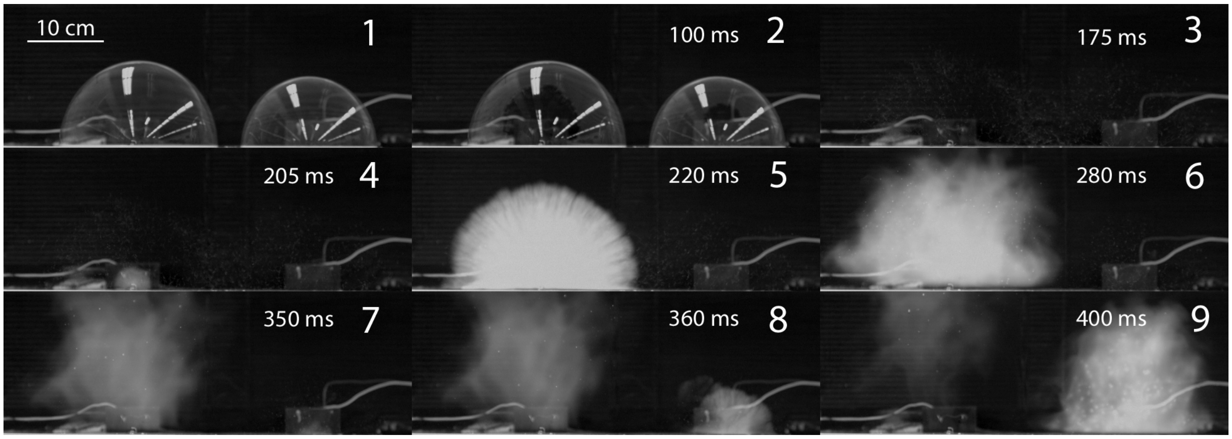

Figure 5.11: Images of 20% H_2-air deflagrations without the soap film recorded at 1,000 fps. The resolution is 1280 x 800. The exposure time is 899.22 μs. Ignition of the second bubble. $R_1 = 11.27$ cm, $R_2 = 8.91$ cm, $D = 3.13$ cm.

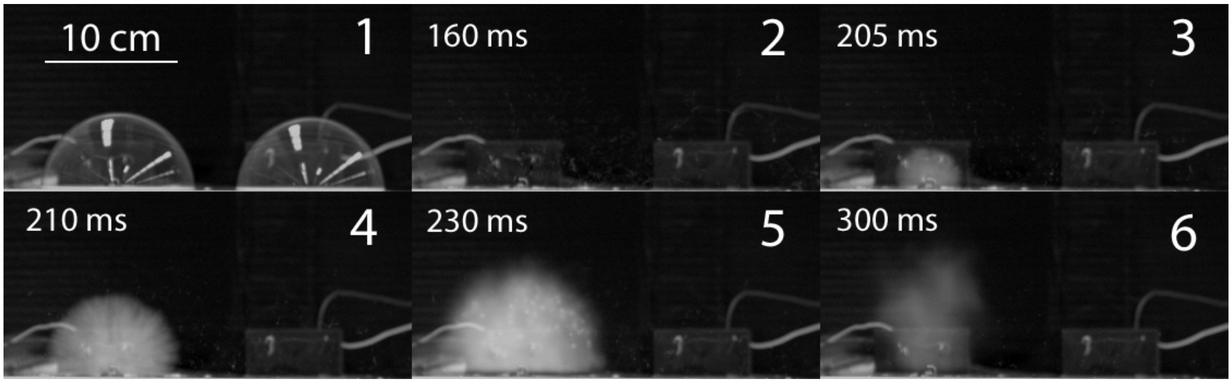

Figure 5.12: Images of 20% H_2-air deflagrations without the soap film recorded at 1,000 fps. The resolution is 1280 x 800. The exposure time is 899.22 μs. No ignition of the second bubble. $R_1 = 6.09$ cm, $R_2 = 5.66$ cm, $D = 3.29$ cm.

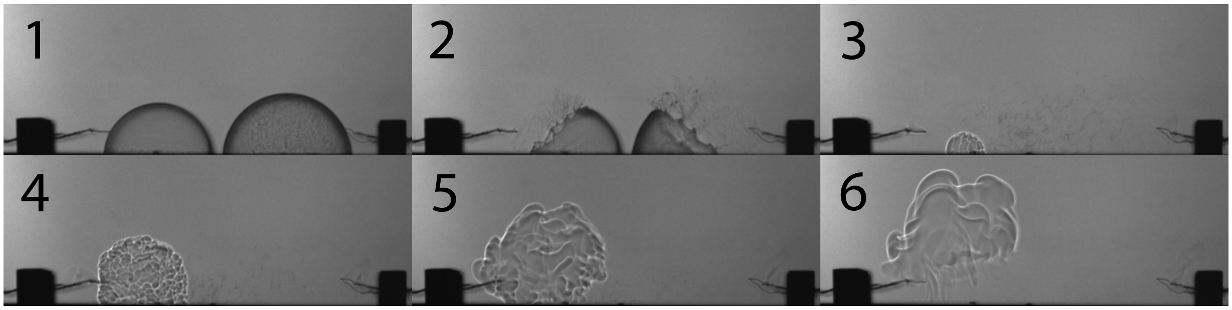

Figure 5.13: Shadowgraph images of 11% H_2-air deflagrations without soap film recorded at 1,000 fps. The resolution is 1280 x 800. The exposure time is 8 μs. No ignition of the second bubble. $R_1 = 5.61$ cm, $R_2 = 6.63$ cm, $D = 1.1$ cm.

test with 11% H_2-air, the results are not likely to be influenced by this effect.

5.3 Analysis of the results and discussion

The results obtained for experiments without the soap film are shown in Fig. 5.14. The results obtained for all mixture compositions are given in Fig. 5.15. Denoting R_1^* the final radius of the first flame kernel, the separation distance criterion described in Section 5.2.1 corresponds to $D/((R_1^* - R_1))$=1 and is represented by the red line (see Fig. 5.15). R_1^* on the y-axis is determined based on the expansion ratio for each concentration. The results obtained for the 15 and 11% H_2 mixtures show that this limit is lower than for the 30 and 20% H_2 mixtures based on the measurements. In fact, as shown in Fig. 5.15, the transition between the successful ignitions and the failure of propagation represented by the green data points and blue points, respectively, shows that the ratio of $D/((R_1^* - R_1)$ decreases with a decrease in the hydrogen concentration. For 11% H_2-air, there is no more transition limit because no data was recorded with successful propagation. The difference in behavior in ignition criteria between the stoichiometric and lean mixtures can be explained by the effect of buoyant convection, as clearly observed in the high-speed movies. As the upward buoyant acceleration of the flame kernel becomes more important, the first flame can no longer reach close to the second adjacent bubble and cause ignition.

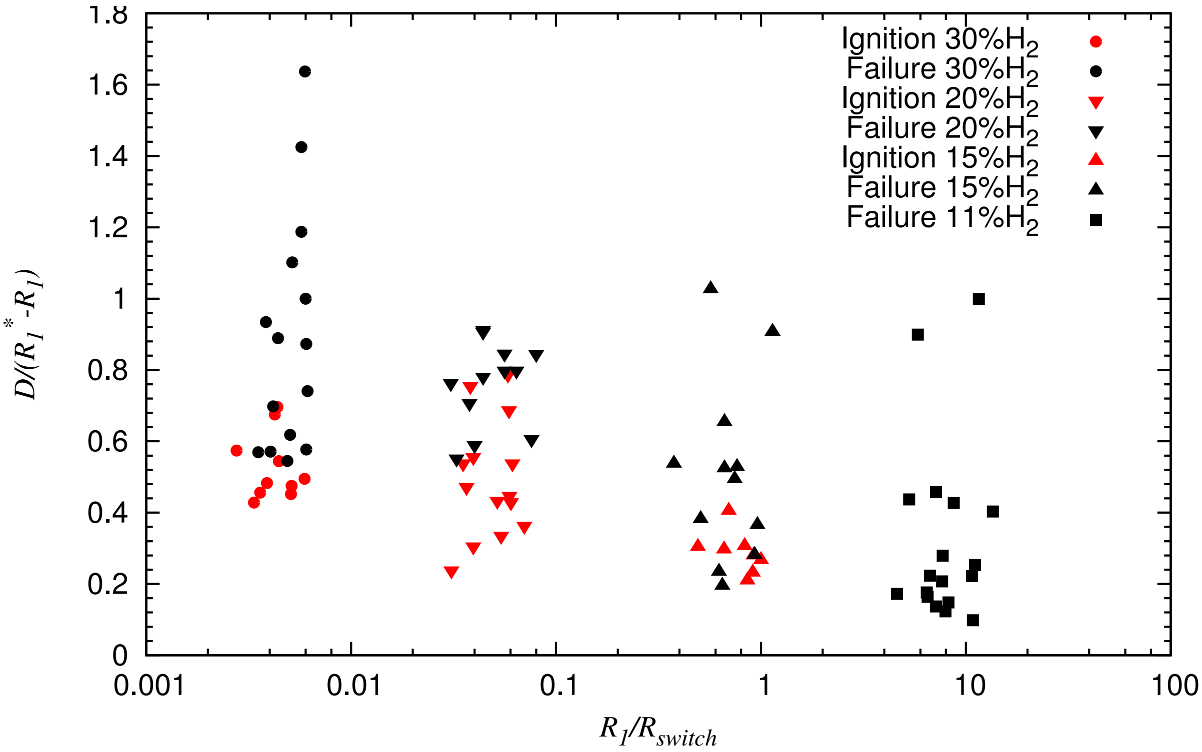

Figure 5.14: Correlation between critical spacing and R_{switch} without soap film.

In order to quantify the buoyancy effect on the spherical flame dynamics, we use the defined radius R_{switch} (see Section 4.4.2). For the same concentration mixture, when the bubble size is smaller than this critical size, flame propagation would not be affected by buoyancy. The transition results reported in Fig. 5.14 and Fig. 5.15 show that indeed this length scale permits one to differentiate the limits in weak and strong mixtures.

Based on the shadowgraphs of the tests without the soap film, the effect of the soap film being burst on the side of the bubbles was only seen on the 11% H_2-air tests and had no significant impact on the tests performed at stoichiometric and 20% H_2-air. This is probably due to the higher flame speed. To counteract the effect from the rupture of the confinement, particularly for lean mixture, we moved the wires to the back of the soap pockets in the later tests.

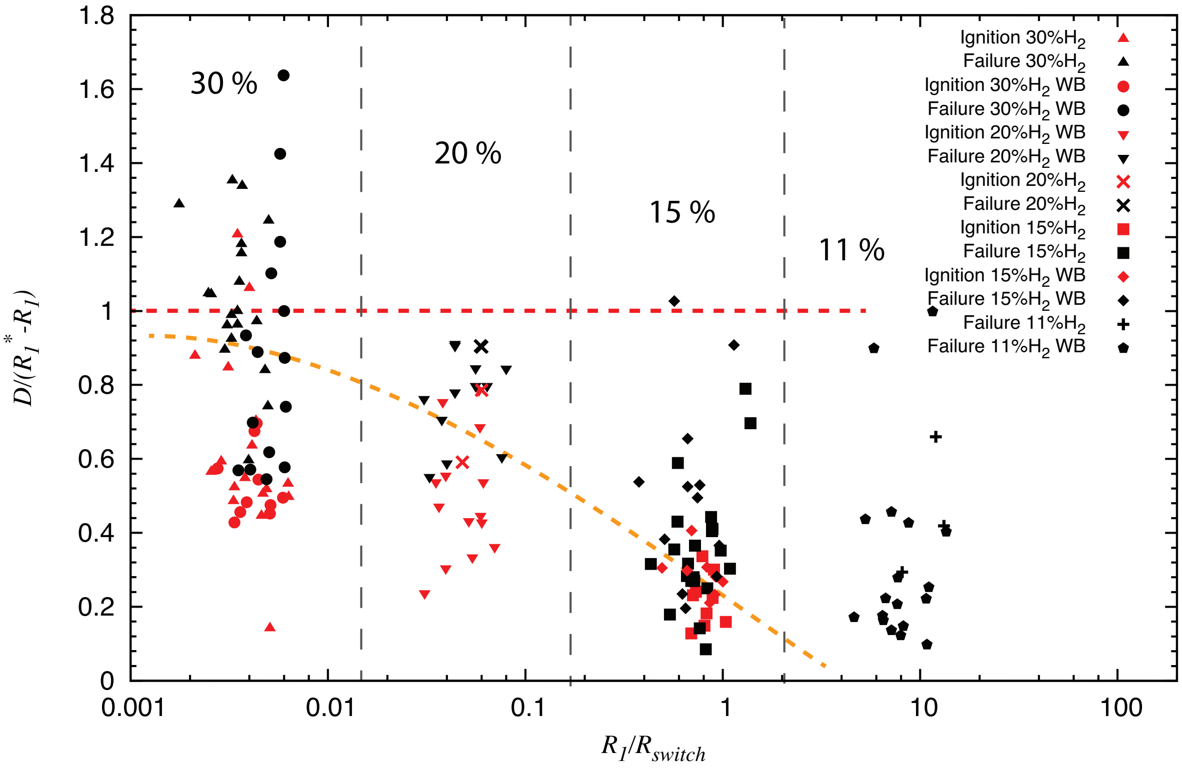

Figure 5.15: Correlation between critical spacing and R_{switch} for all data. WB: without soap film.

5.4 Conclusion

The present chapter has provided the scaling laws necessary to predict the transition of a flame between neighboring pockets of gas separated by air. The results have revealed that the separation distance for mixtures near stoichiometry is given by the distance that the flame must expand to reach the original location of the second neighboring kernel. This criterion mainly depends on the expansion ratio. However, it has been shown that for leaner mixtures (i.e., 11% and 15% H_2 in air) characterized by lower flame speeds, buoyancy effects begin to play a role at smaller scales. The flame kernel rises due to buoyant effects before the flame can reach the second bubble. Hence the critical separation distance becomes much smaller and is no longer determined by the expansion ratio. The tests with and without soap film did not show a significant difference in the flame propagation conditions results. It showed however that the soap film being burst on the side on the propagation direction could possibly disturb the symmetrical gas expansion for mixture with low flame speed (from 11% H_2).

Chapter 6

Spherical bubble tests

This chapter reports preliminary experiments with two nearly spherical bubbles, maintained on individual supports of smaller footprint than in the hemispherical bubbles addressed in the previous chapter.

6.1 Test configuration and conditions

In order to study the effect of the boundary layer on the propagation of the flame, tests have been made with nearly spherical bubbles at 30% H_2-air, 15% H_2-air and 11% H_2-air and recorded with the shadowgraph system. Experiments were conducted with and without the soap film of the bubbles. In the tests without the soap film, the heated wires were placed at the back to not disturb and affect the flame dynamics in the propagation direction between the adjacent bubbles.

6.2 Experimental results

Stochiometric H_2-air

Figure 6.1 illustrates the dynamics of two adjacent spherical bubbles filled with stoichiometric hydrogen-air. In the second frame of Fig. 6.1, the soap film is burst from the back

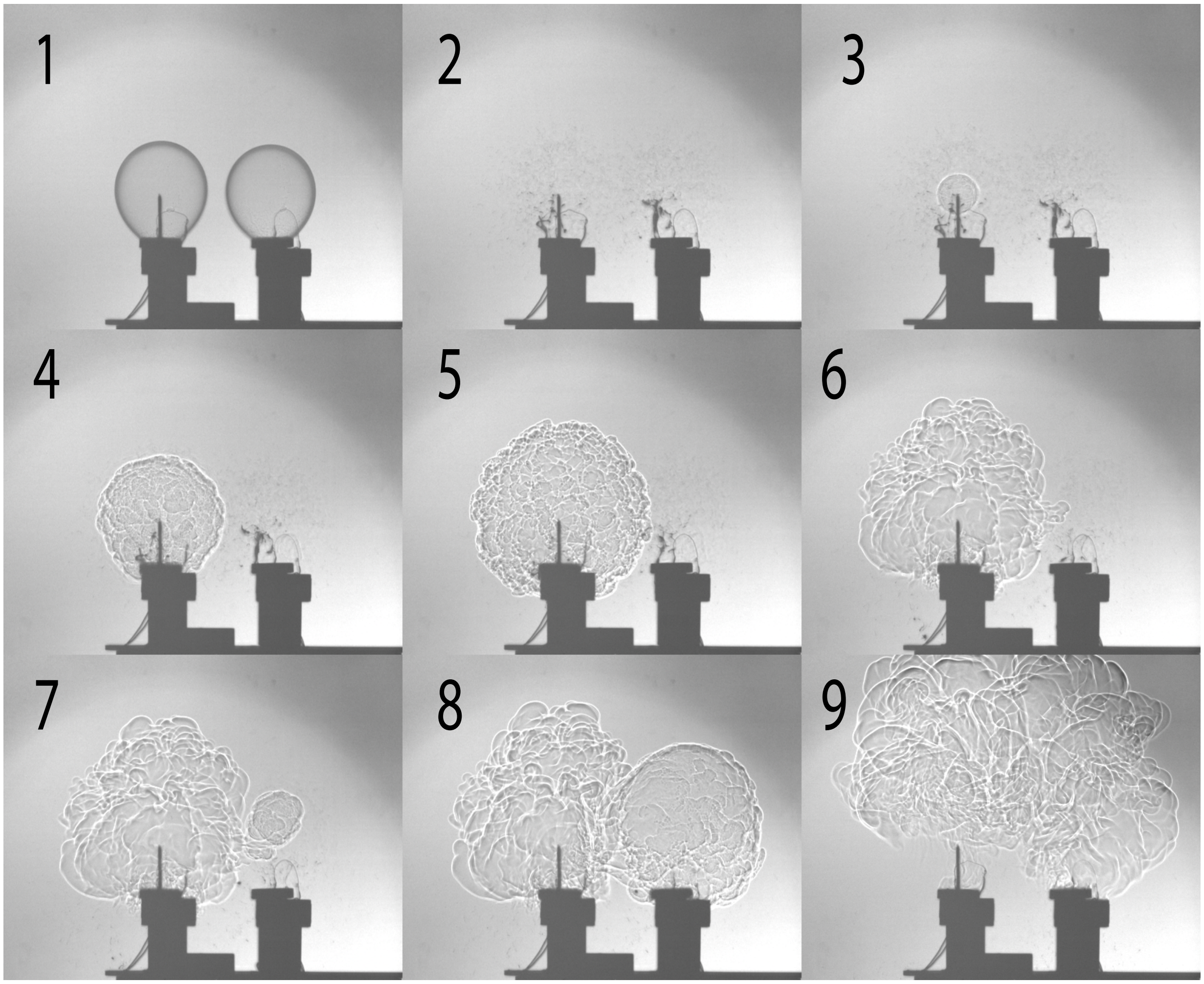

Figure 6.1: Images of 30% H_2-air spherical deflagrations without soap film. Ignition of the second pocket.

with the heated wires. Then, the electrodes ignite the mixture and a perfectly spherical, laminar and smooth flame freely expands as seen in the third frame. In the earlier stages when the flame radius is small, the flame front seems stable. Later in the fifth and sixth frames, creases appear on the front of the flame due to instabilities. Those instabilities could be hydrodynamic and diffusive thermal instabilities. The creases of the flame front lead the flame velocity to accelerate [44]. In the fourth frame, the gas products reached the initial position of the second bubble without leading to a propagation. In the successive frames, the flame expanded further to reach the gas of the second pocket which was pushed by the expansion of the first flame (see the sixth frame).

A summary of the experiments performed in stoichiometric mixtures is shown in Fig. 6.2 for experiments with the soap bubble burst and not burst. In spite of the apparent large scatter in the experiments, we find, somewhat surprisingly, that the critical separation distance between neighboring pockets in the spherical bubble experiments is similar to the one determined for the hemispherical bubbles (see Fig. 5.15). At present, these results are difficult to rationalize. One possibility is that turbulent convection, enhanced by the popping of the soap bubbles, enhances the mixing of the gases along the axis of ignition. This can also explain the apparent irreproducibility in the results indicated by the wide experimental scatter.

Experiments with 15% H_2-Air

Figure 6.3 shows selected frames of experiments with a mixture composition of 15% H_2-air. The different frames illustrate a successful propagation event of the flame from the first pocket to the second pocket. In the early frames, the flame expands similarly to the stochiometric mixture tests, but with a much slower speed. At the fourth frame, the flame surface reaches the initial position of the second pocket. The flame then starts rising (fifth frame). Similar to the tests with hemispherical shape at 15% H_2-air, the lowest surface of the flame progressively propagates to ignite the reactive gas initially confined in the second pocket. The propagation occurs while the burned gases of the first bubble are rising. It is worth noting that unlike the hemispherical tests with the soap film, the ignition of the

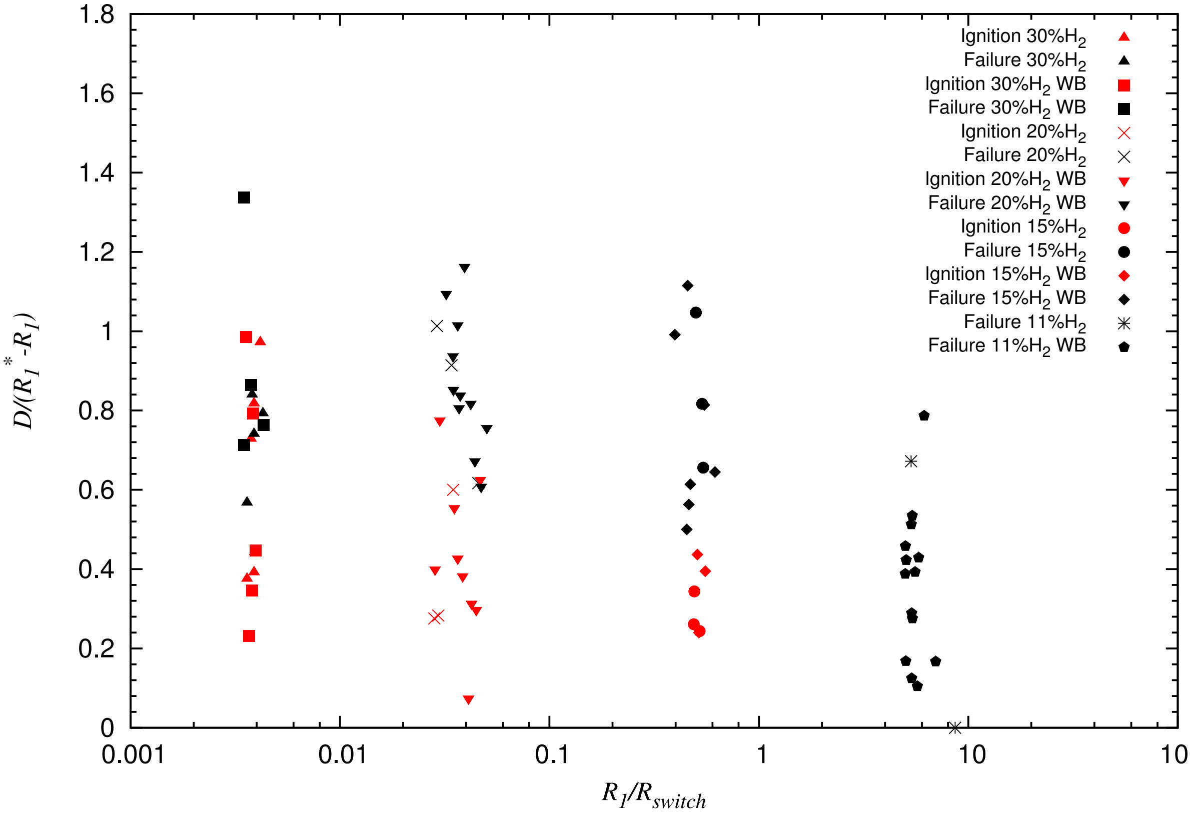

Figure 6.2: Correlation between critical spacing and R_{switch} for all spherical data. WB: without soap film.

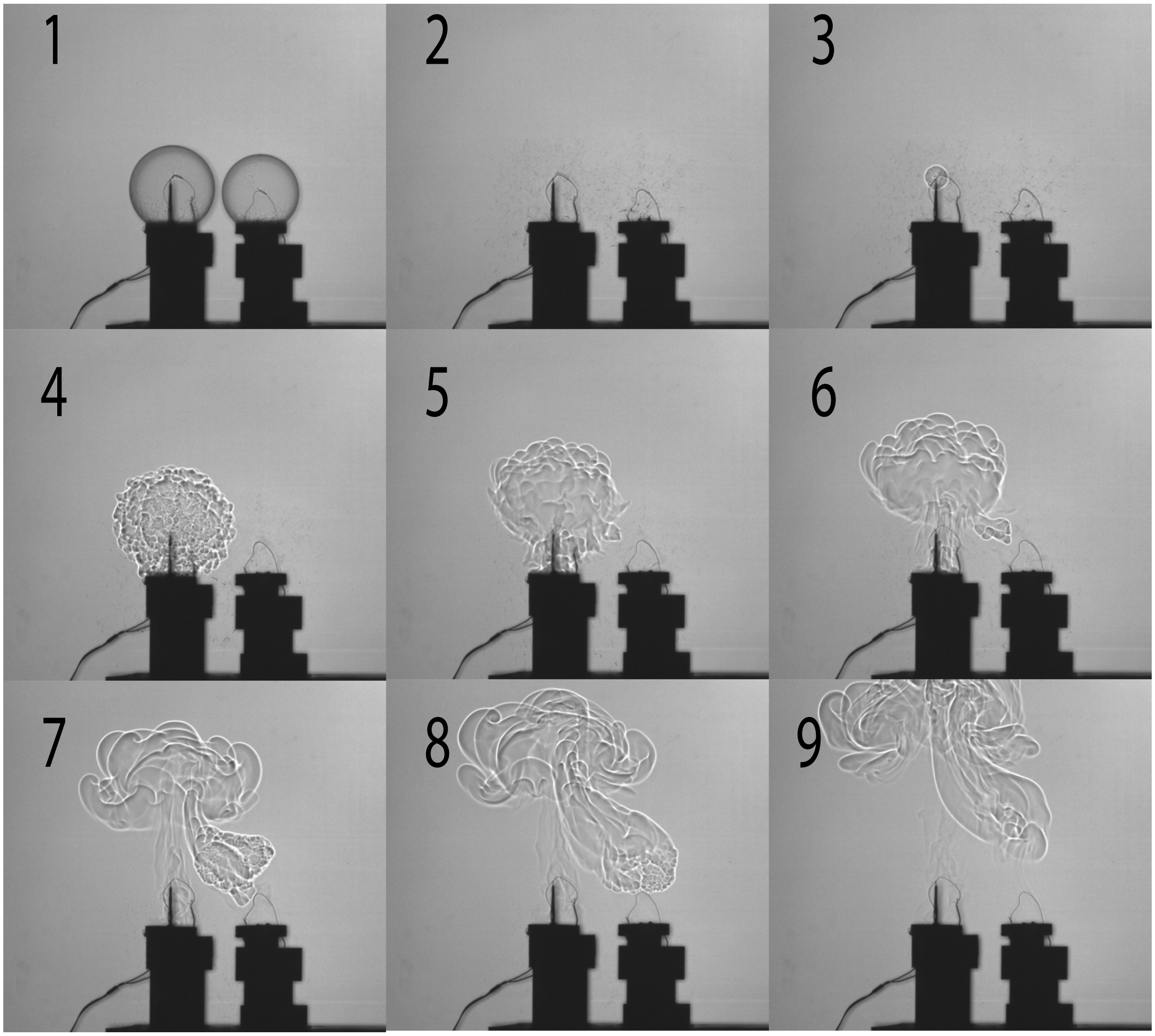

Figure 6.3: Images of 15% H_2-air spherical deflagrations without soap film. Ignition of the second pocket.

second pocket arose far from the bubble support and not next to the plate. This difference could be related to the effect of the boundary layer providing a closest distance path in the hemispherical bubbles. Moreover, the flame transmission in this test does not happen along the bubble center axis, again highlighting the inferred action of buoyant effects in the hemispherical bubbles at this concentration.

A summary of the experiments performed in 15% H_2-air mixtures is shown in Fig. 6.2 for experiments with the soap bubble burst and not burst. The scatter appears to now be reduced, as compared to stiochiometric mixtures. The results obtained are also found in good agreement with the results presented for hemispherical bubbles (see Fig. 5.15). These observations, along with the visual confirmation of buoyant effects, suggest that the separation distance is now a function of how rapidly the first flame kernel pulls away from the second, due to buoyancy.

Experiments with 11% H_2-Air

Experiments performed in 11% H_2-air mixtures revealed that transmission was not possible to the second bubble, irrespective of how close the bubbles were made, with the soap film burst or not. Figure 6.4 illustrates once again a failure of propagation of the flame to the second bubble at 11% H_2-air despite the extremely small separation distance. In the second frame, the flame expands symmetrically. However, the third frame shows clearly that the flame begins to rise while expanding. The velocity in the upward direction is higher than the velocity downward. The burned gas continues moving up without reaching the gas of the second bubble. At these conditions, as shown in Fig. 6.2, the bubble size was always larger than the predicted critical radius, suggesting that the first bubble will rise before propagating to the second bubble.

6.3 Summary and concluding remarks

Figure 6.2 summarizes the results of the tests performed with spherical bubbles at stoichiometric, 20% H_2-air, 15% H_2-air and 11% H_2-air. The limits measured for the spherical

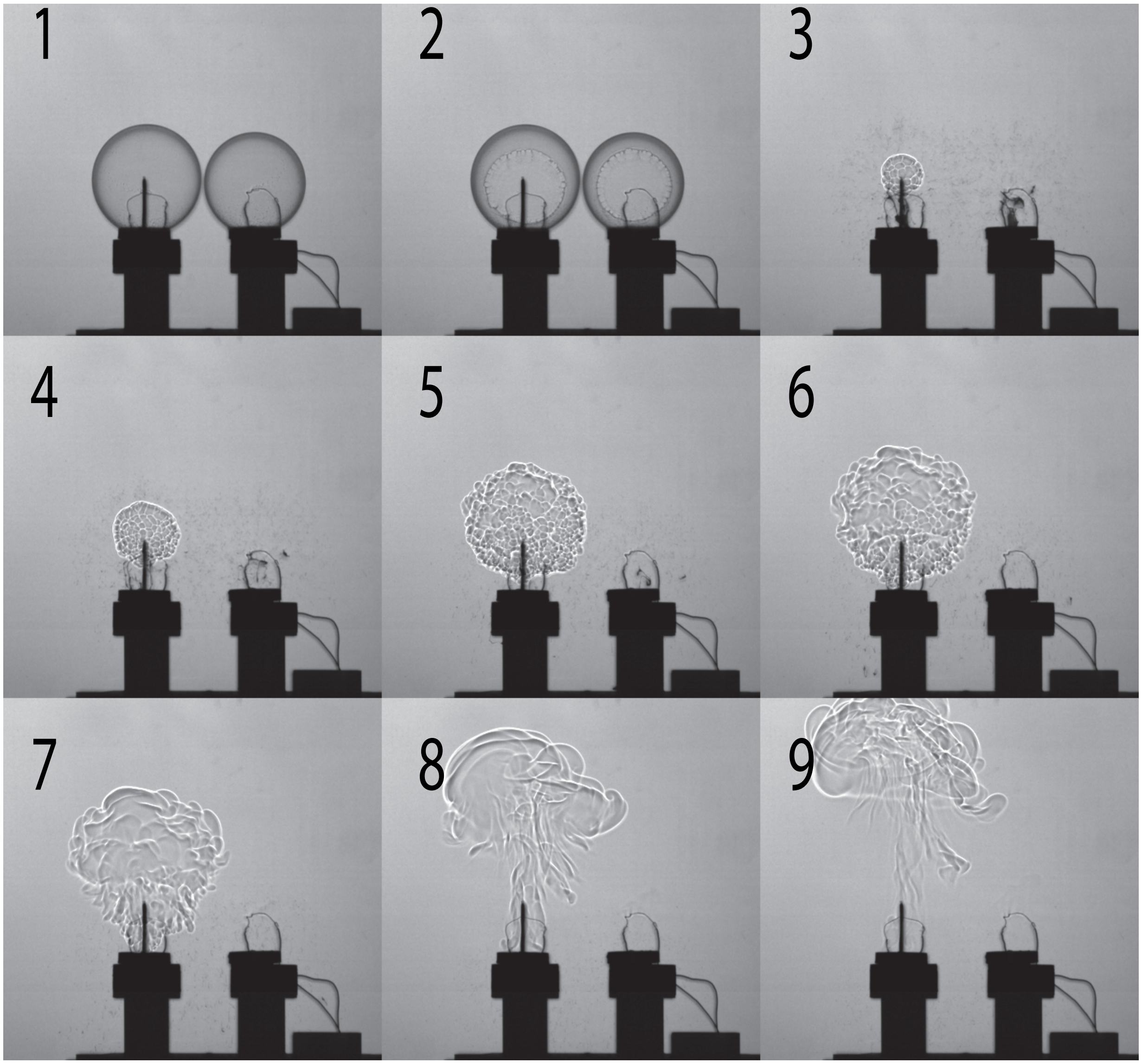

Figure 6.4: Images of 11% H_2-air spherical deflagrations without soap film.

flames are very similar to the ones measured with the hemispherical bubbles for all concentrations, although the limits observed for the spherical flames are somewhat narrower; bubbles need to be somewhat closer for ignition. The relative agreement nevertheless supports the view that the ignition between the two bubbles is principally governed by the initial distance between the two bubbles. The presence of a boundary layer in the hemispherical experiments thus provides a reproducible location for ignition of the second bubble, as this is the location where the gases of the first bubble are closest to the gases of the second.

Chapter 7

Conclusion

7.1 Contributions to the state of knowledge

This thesis investigated the dynamics of unconfined hydrogen-air flames and sought to determine the critical distance for flame propagation between neighboring pockets of reactive gas separated by air. The soap bubble method was selected and improved to conduct flame experiments using a soapy solution with the longest survival time. Visualization of the various experiments was achieved using schlieren photographs and large shadowgraphs for larger field of view.

In the first part, the dynamics inside a single hemispherical bubble were examined at different mixture concentrations. Flame visualization indicated that the buoyancy effects become important at small scales when the flame is sufficiently weak, such that the flame speed evolves on times scales longer than buoyancy. This was observed for very lean mixtures starting from 15% H_2-air. The critical flame dimension, defined as R_{switch}, beyond which the flame sphere motion becomes buoyancy dominated, was experimentally measured and found to be strongly sensitive to the hydrogen concentration. As the flame grows from a small radius, it will not be influenced by buoyant forces until its radius becomes comparable with the critical radius, estimated to be

$$R = R_{switch} = \frac{9}{16}\frac{{S_L}^2}{g}\left(\frac{\rho_b}{\rho_u}\right)^{-2}\left(1-\frac{\rho_b}{\rho_u}\right)^{-1} \tag{7.1}$$

This simple estimate was found in excellent agreement with the measurements.

In the second part of the thesis, tests with two adjacent pockets of reactive gas were conducted. Based on the experiments, scaling laws necessary to predict the transition of a flame between adjacent pockets of gas separated by air were provided. The results have shown that for the stoichiometric concentration the critical distance of transition of a flame between neighboring pockets is given by the distance that the flame must expand to reach the original location of the second kernel. Thus, this critical distance is mainly determined by the expansion ratio. It has been also shown that for lean mixtures, the flame kernel rises due to buoyancy effects before the flame can propagate to the second bubble. Thus the critical separation distance decreases and is no longer determined by the expansion ratio.

Finally, the same experiments were conducted in spherical flames. It has been observed that the flame was mainly transmitted along the bubble center axis only for stochiometric mixtures. The comparison between the results of spherical and hemispherical tests showed that the separation criterion for successful flame propagation to neighbouring bubbles was not significantly altered and that the shape did not affect the criterion of transition when buoyancy effects became important.

7.2 Recommendations for future study

Based on the work performed, a series of recommendations can be made for addressing some of the outstanding issues and possible extensions to this work. These are:

- measurements of the burning velocity were obtained based on the soap bubble method for the different H_2-air concentrations. The experimental results showed good agreement with laminar flame speed measurements made without accounting for stretch effects. Future work should address the suitability of the soap bubble method to measure stretch-free flames;

- measurement of pressure history over the flame propagation process can also provide more insight into convective effects;
- as the ignition process is likely to operate along the line of closest distance between the two pockets, a one dimensional model can be formulated to study the influence of an inert gap between two zones of flammable mixture and determine the critical separating distance for a successful propagation. This will provide insight into the physical mechanisms dominating the ignition process;
- in order to dismiss the effect of the soap film, the moisture present could be quantified and included in the calculation of the flame transition;
- the experimental setup can be updated to allow remote operation, making it more portable and permitting its installation inside other chambers where the ambient pressure and gas composition can be modified.

7.3 Publications of parts of this thesis

Parts of the material contained in this thesis has been presented at conferences and published in journal publications, as follows:

Section 2.2.4 and parts of Chapter 4 are available in:

- L. Leblanc, M. Manoubi, K. Dennis, Z. Liang, and M.I. Radulescu, Influence of buoyancy in unconfined deflagrations: Experiments in soap bubbles, 7th International Seminar on Fire and Explosion Hazards, Providence, USA, 2013.
- L. Leblanc, M. Manoubi, K. Dennis, Z. Liang, and M. Radulescu, Dynamics of unconfined spherical flames: Influence of buoyancy, Physics of Fluids, AIP Publishing LLC 25/9, (2013)

Parts of Chapter 5 have been presented in:

- Manoubi M., La Flèche M., Liang Z., and Radulescu M.I, Criteria for a flame to propagate between neighboring pockets of reactive gas, 10th International Symposium on Hazards, Prevention, and Mitigation of Industrial Explosions, 10-14 June 2014, Bergen, Norway.

References

[1] J. P. Van Dorsselaere, T. Albiol, and J. C. Micaelli. Research on severe accidents in nuclear power plants. Technical report, Nuclear Power - Operation, Safety and Environment, InTech, 2011.

[2] A. C. Ratzel. Data analyses for nevada test site (NTS) premixed combustion tests. Technical Report NUREG/CR-4138, Sandia National Laboratories, 1985.

[3] T. K. Blanchat and D. W. Stamps. Deliberate ignition of hydrogen-air-steam mixtures in condensing steam environments. Technical Report NUREG/CR-6530, Sandia National Laboratories, 1985.

[4] P. Girard, M. Huneau, C. Rabasse, and J. C. Leyer. Flame propagation through unconfined and confined hemispherical stratified gaseous mixtures. *Proceedings of the Combustion Institute*, 17:1247–1255, 1979.

[5] O. Badr and G. Karim. Flame propagation in stratified methane-air mixtures. *Journal of Fire Sciences*, 2:415–426, 1984.

[6] D. R. Whitehouse, D. R. Greig, and G. W. Koroll. Combustion of stratified hydrogen-air mixtures in the 10.7 m3 combustion test facility cylinder. *Nuclear Engineering and Design*, 166:453–462, 1996.

[7] I. Junya, T. Mitsuaki, and A. Kiyoshi. Flame propagation through concentration gradient. *Journal of Thermal Science*, 9:371–375, 2000.

[8] I. Sochet, F. Guelon, and P. Gillard. Deflagrations of non-uniform mixtures: A first experimental approach. *Journal de physique IV*, 12:273–279, 2002.

[9] I. Sochet, P. Gillard, and F. Guelon. Effect of the concentration distribution on the gaseous deflagration propagation in the case of H2/O2 mixture. *Journal of Loss Prevention in the Process Industries*, 19:250262, 2006.

[10] W. Rudy, M. Kuznetsov, R. Porowski, A. Teodorczyk, J. Grune, and K. Sempert. Critical conditions of hydrogenair detonation in partially confined geometry. *Proceedings of the Combustion Institute*, 34:1965–1972, 2013.

[11] J. Brossard, D. Desbordes, J. C. Leyer, J. P. Saint-Cloud, N. Difabio, J. L. Gamier, A. Lannoy, and J. Perrot. Truly unconfned deflagration of ethylene air mixture. Technical report, Proceeding of 10th International Colloquium on Explosives and Reactive Systems, AIAA Series, 1986.

[12] F. W. Stevens. The rate of flame propagation in gaseous explosive reactions. *Journal of the American Chemical Society*, 48:1896–1906, 1926.

[13] J. W. Linnett, H. S. Pickering, and P. J. Wheatley. Burning velocity determinations. part IV.-the soap bubble method of determining burning velocities. *Trans. Faraday Soc.*, 47:974–980, 1951.

[14] R. A. Strehlow and J. G. Stuart. An improved soap bubble method of measuring flame velocities. *Proceedings of the Combustion Institute*, 4:329–336, 1953.

[15] C. Guibert-Duplantier, J. C. Leyer, and D. Desbordes. The terminal phase of an unconfined hemispherical deflagration. *Shock Waves*, 6:115–118, 1996.

[16] M. A. Rutgers, X. L. Wu, and W. B. Daniel. Conducting fluid dynamics experiments with vertical falling soap films. *Review of Scientific Instruments*, 72:3025–3037, 2001.

[17] R. Hidema, Z. Yatabe, M. Shoji, C. Hashimoto, R. Pansu, G. Sagarzazu, and H. Ushiki. Image analysis of thickness in flowing soap films. I: effects of polymer. *Experiments in Fluids*, 49:725–732, 2010.

[18] P. Ballet and F. Graner. Giant soap curtains for public presentations. *European Journal of Physics*, 27:951–967, 2006.

[19] Guar gum. `http://soapbubble.wikia.com/wiki/Guar_Gum`. Accessed: 2013-01-18.

[20] H. S. Pickering and J. W. Linnett. Burning velocity determinations part VI.-the use of schlieren photography in determining burning velocities by the soap bubble method. *Trans. Faraday Soc.*, 47:989–992, 1951.

[21] G.S. Settles, T.P. Grumstrup, J.D. Miller, M.J. Hargather, L.J. Dodson, and J.A. Gatto. Full-Scale High-Speed ”Edgerton” retroreflective shadowgraphy of explosions and gunshots. In *5th Pacific Symposium on Flow Visualization and Image Processing*, 2005.

[22] K. Dennis, L. Maley, Z. Liang, and M. I. Radulescu. Implementation of large scale shadowgraphy in hydrogen explosion phenomena. *International Journal of Hydrogen*, 39:1134611353, 2014.

[23] C. K. Law and G. M. Faeth. Opportunities and challenges of combustion in microgravity. *Progress in Energy and Combustion Science*, 20:65–113, 1994.

[24] V. S. Babkin, A. Ya. Vykhristuk, V. N. Krivulin, and E. Kudriavcev. Convective instability of spherical flames. *Archivum Combustionis*, 4:321–328, 1984.

[25] M. Zingale and L. J. Dursi. Propagation of the first flames in type Ia supernovae. *Astrophysical Journal*, 656:333–346, 2007.

[26] G. S. Settles. *Schlieren and Shadowgraph Techniques.* Springer-Verlag, 2001.

[27] R. R. Bhattacharjee. Experimental investigation of detonation re-initiation mechanisms following a mach reflection of a quenched detonation. *M.A.Sc Thesis. University of Ottawa.*, 2013.

[28] H. E. Edgerton. Shock wave photography of large subjects in daylight. *Review of Scientific Instruments*, 29:171–172, 1958.

[29] H. E. Edgerton. *Electronic Flash - Strobe.* The MIT Press, 3 edition, 1987.

[30] G. W. Koroll, R. K. Kumar, and E. M. Bowles. Burning velocities of hydrogen-air mixtures. *Combustion and Flame*, 94:330–340, 1993.

[31] M. Berman. Light-water reactor safety. *Report SAND 84/0689, Sandia National Laboratories*, 1984.

[32] G.E. Andrews and D. Bradley. Determination of burning velocity by double ignition in a closed vessel. *Combustion and Flame*, 20:77–89, 1973.

[33] F. N. Egolfopoulos and C. K. Law. An experimental and computational study of the burning rates of ultra-lean to moderately-rich H2/O2/N2 laminar flames with pressure variations. *The Combustion Institute*, 23:333–340, 1991.

[34] C. M. Vagelopoulos, F. N. Egolfopoulos, and C.K. Law. Further considerations on the determination of faminar flame speeds with the counterflow twin-flame technique. *The Combustion Institute*, 109:1341–1347, 1994.

[35] D. R. Dowdy, D. B. Smith, and S. C. Taylor. The use of expanding spherical flames to determine burning velocities and stretch effects in hydrogen/air mixtures. *The Combustion Institute*, 23:325–332, 1990.

[36] S. Verhelst, R. Woolley, M. Lawes, and R. Sierens. Laminar and unstable burning velocities and markstein lengths of hydrogenair mixtures at engine-like conditions. *Proceedings of the Combustion Institute*, 30:209–216, 2005.

[37] V. P. Karpov, A. N. Lipatnikov, and P. Wolanski. Finding the markstein number using the measurements of expanding spherical laminar flames. *Combustion and Flame*, 109:436–448, 1997.

[38] N. Lamoureux, N. Djebaili-Chaumeix, and C. E. Paillard. Laminar flame velocity determination for H2-air-he-co2 mixtures using the spherical bomb method. *Experimental Thermal and Fluid Science*, 27:385–393, 2003.

[39] Z. Chen, M. P. Burke, and Y. Ju. Effects of Lewis number and ignition energy on the determination of laminar flame speed using propagating spherical flames. *Proceedings of the Combustion Institute*, 32:1253–1260, 2009.

[40] M. C. Krejci, O. Mathieu, A. J. Vissotski, S. Ravi, T. G. Sikes, and E. L. Laminar flame speed and ignition delay time data for the kinetic methods modeling of hydrogen and syngeas fuel blends. *Journal of Engineering for Gas Turbines and Power*, 135, 2013.

[41] J. Li, Z. Zhao, A. Kazakov, and F. Dryer. An updated comprehensive kinetic model of hydrogen combustion. *International journal of chemical kinetics*, 36:566–575, 2004.

[42] R. M. Davies and G. Taylor. The mechanics of large scale bubbles rising through extended liquids and through liquids in tubes. *Proceedings of the Royal Society of London Series A-Mathematical and Physical Sciences*, 200:375–390, 1950.

[43] W. Breitung, C. Chan, S. Dorofeev, A. Eder, B. Gelfand, M. Heitsch, R. Klein, A. Malliakos, E. Shepherd, E. Studer, and P. Thibault. Flame acceleration and deflagration-to-detonation transition in nuclear safety. Technical report, Nuclear Safety, 2000.

[44] W. K. Kim, T. Mogi, and R. Dobashi. Fundamental study on accidental explosion behavior of hydrogen-air mixtures in an open space. *International Journal of Hydrogen Energy*, 38:802–8029, 2013.

Appendix A

Results of the One bubble tests

The following table provides the results of the laminar flame speed measurements of the single bubble tests. Included in the table are the test's date, the test's number, the size of the bubble, the frame rate of the schlieren videos and the laminar burning velocities of each concentrations (7% H_2-air, 8.9% H_2-air, 11.9% H_2-air,23% H_2-air and 30% H_2-air).

Table A.1: Test matrix of single bubble tests

Test Date	Test ID	H_2, vol%	Radius, cm	Used for analysis	Laminar flame speed [m/s]	Frame rate [fps]
17-01-2013	B1	7.0	12.7		-	5,000
17-01-2013	B2	7.0	9.3	✓	0.095	5,000
17-01-2013	B3	7.0	11.2		-	5,000
14-01-2013	B1	8.9	13.6		-	30,018
14-01-2013	B2	8.9	9.2	✓	0.102	30,018
14-01-2013	B3	8.9	17.1		-	30,018
14-01-2013	B4	8.9	9.0		-	30,018
09-01-2013	B1	11.9	8.1	✓	0.303	30,018
09-01-2013	B2	11.9	11.5		-	30,018
09-01-2013	B3	11.9	9.6		-	30,018
08-01-2013	B1	14.8	10.5		-	30,018
08-01-2013	B2	14.8	8.7		-	30,018
08-01-2013	B3	14.8	8.2		-	30,018
08-01-2013	B4	14.8	11.5	✓	0.674	30,018
26-10-2012	BB2	23.0	7.8		-	16,000
26-10-2012	BB2	23.0	7.3	✓	1.927	16,000
16-01-2013	B1	30.0	8.6		-	30,018
16-01-2013	B2	30.0	12.0	✓	2.557	30,018
16-01-2013	B3	30.0	10.5		-	30,018

Appendix B

Results of the Two bubble tests

The following tables provide the results of the double hemi-spherical bubble tests using the shadowgraph system. The tests are organized according to the concentration of the mixture (11% H_2-air, 15% H_2-air, 20% and stoichiometric mixture) and either the soap bubble was burst or not prior to the experiments. Included in the table are the test's date, the test's number, the size of both bubbles, the separating distance, whether or not the transition was successful, the final radius of the flame and other ratios.

Table B.1: Test matrices of two bubble tests with 11% H_2 in air (with soap bubble)

Test Date	Test ID	R_1 [cm]	R_2 [cm]	Separation D [cm]	R_1/R_2	R_1/D	Ignition	$R_1/Rswitch$	$R_1{}^*$ [cm]	$D/(R_1{}^* - R_1)$
23-12-2013	2	13.4	8.9	4.8	1.514	2.770	n	3.000	20.8	0.660
23-12-2013	3	14.8	9.0	3.4	1.641	4.364	n	3.301	22.8	0.419
23-12-2013	4	9.1	5.1	1.5	1.795	6.211	n	2.029	14.0	0.294

Depending on the type of visualization (shadowgraph or free view), the exposure times for these series are varied between 8 s, 10 s and 899.22 s. The videos are recorded at 1,000 fps or 3,000 fps with a resolution of 1280 x 800 pixels. For this concentration, R_{switch} is estimated to 0.045 m (using Cantera). The expansion ratio is 0.270.

Table B.2: Test matrices of two bubble tests with 11% H_2 in air (without soap bubble)

Test Date	Test ID	R_1 [cm]	R_2 [cm]	Separation D [cm]	R_1/R_2	R_1/D	Ignition	$R_1/Rswitch$	$R_1{}^*$ [cm]	$D/(R_1{}^* - R_1)$
21-05-2014	1	12.9	9.3	7.1	1.38	1.83	n	1.292	20.0	0.999
21-05-2014	2	6.5	6.4	3.2	1.01	2.03	n	0.651	10.1	0.899
21-05-2014	3	9.8	9.1	2.3	1.08	4.29	n	0.977	15.1	0.427
21-05-2014	4	12.1	8.5	0.7	1.43	18.58	n	1.21	18.7	0.098
21-05-2014	5	7.2	6.9	0.7	1.04	10.41	n	0.72	11.1	0.176
21-05-2014	6	7.3	6.8	0.7	1.08	11.17	n	0.727	11.3	0.164
22-05-2014	1	15.2	11.0	3.3	1.38	4.54	n	1.515	23.4	0.403
22-05-2014	2	12.0	10.8	1.5	1.11	8.24	n	1.198	18.5	0.222
22-05-2014	4	8.9	5.5	0.6	1.63	14.86	n	0.89	13.8	0.123
22-05-2014	6	9.2	7.3	0.7	1.25	12.38	n	0.918	14.2	0.148
22-05-2014	9	5.9	7.6	1.4	0.77	4.18	n	0.59	9.1	0.437
22-05-2014	11	8.6	7.7	1.3	1.11	6.57	n	0.861	13.3	0.279
22-05-2014	12	12.4	8.8	1.7	1.41	7.23	n	1.238	19.2	0.253
22-05-2014	13	7.5	9.2	0.9	0.81	8.19	n	0.747	11.6	0.223
22-05-2014	14	4.6	5.3	0.8	0.87	5.63	n	0.458	7.1	0.325
22-05-2014	15	5.1	5.2	0.5	0.97	9.83	n	0.505	7.8	0.186
22-05-2014	16	5.2	5.4	0.5	0.96	10.65	n	0.516	8.0	0.172
22-05-2014	17	8.0	7.9	0.6	1.01	13.33	n	0.799	12.4	0.137
22-05-2014	18	8.6	9.0	1.0	0.95	8.82	n	0.856	13.2	0.207
22-05-2014	19	8.0	7.0	2.0	1.13	4	n	0.799	12.4	0.457

Depending on the type of visualization (shadowgraph or free view), the exposure times for these series are varied between 8 s, 10 s and 899.22 s. The videos are recorded at 1,000 fps or 3,000 fps with a resolution of 1280 x 800 pixels. For this concentration, R_{switch} is estimated to 0.045 m (using Cantera). The expansion ratio is 0.270.

Table B.3: Test matrices of two bubble tests with 15% H_2 in air (with soap bubble)

Test Date	Test ID	R_1, cm	R_2, cm	Separation D, cm	R_1/R_2	R_1/D	Ignition	$R_1/Rswitch$	$R_1{}^*$, cm	$D/(R_1{}^* - R_1)$
13-09-2013	1	6.5	6.2	1.2	1.04	5.39	n	0.165	10.7	0.283
13-09-2013	2	8.7	6.4	2.3	1.35	3.76	n	0.221	14.3	0.405
13-09-2013	3	8.7	6.5	2.3	1.34	3.72	n	0.222	14.4	0.41
13-09-2013	4	8.7	6.5	2.3	1.34	3.71	n	0.221	14.4	0.411
13-09-2013	5	8.6	6.3	1.8	1.41	5.06	y	0.226	14.4	0.301
13-09-2013	6	7.0	5.6	1.3	1.26	5.44	n	0.178	11.6	0.28
13-09-2013	7	6.9	5.6	1.1	1.23	6.58	y	0.177	11.5	0.231
13-09-2013	8	7.0	6.8	1.3	1.04	5.64	n	0.179	11.6	0.27
13-09-2013	9	6.0	5.9	1.4	1.11	4.8	n	0.167	10.3	0.317
10-05-2014	13	12.9	10.7	1.0	1.21	12.8	y	0.329	21.4	0.119
17-05-2014	7	11.6	10.1	2.6	1.14	4.38	y	0.295	19.2	0.348
17-05-2014	8	10.9	11.2	1.4	0.98	7.6	y	0.278	18.1	0.2
17-05-2014	9	12.8	9.1	4.0	1.41	3.21	y	0.326	21.2	0.475
17-05-2014	10	12.5	9.8	3.6	1.28	3.49	y	0.318	20.7	0.436
17-05-2014	13	7.3	7.8	1.7	0.93	4.38	y	0.185	12.0	0.348
17-05-2014	14	5.2	5.4	0.9	0.97	5.91	y	0.133	8.6	0.258
17-05-2014	15	5.4	5.5	0.9	0.98	6.12	y	0.137	8.9	0.249
17-05-2014	16	8.6	7.8	1.7	1.1	5.03	y	0.219	14.2	0.303
17-05-2014	17	5.1	4.4	0.8	1.14	6.55	n	0.13	8.4	0.233
17-05-2014	18	5.2	5.1	1.8	1.02	2.86	y	0.132	8.6	0.533
17-05-2014	19	5.1	5.0	1.2	1.02	4.37	y	0.13	8.4	0.349

Test Date	Test ID	R_1 [cm]	R_2 [cm]	Separation D [cm]	R_1/R_2	R_1/D	Ignition	$R_1/Rswitch$	$R_1{}^*$ [cm]	$D/(R_1{}^* - R_1)$
19-05-2014	1	13.6	11.6	6.2	1.17	2.19	n	0.346	22.5	0.697
19-05-2014	2	12.8	10.5	6.6	1.22	1.93	n	0.326	21.2	0.79
19-05-2014	3	8.2	9.2	1.4	0.89	6.09	n	0.209	13.6	0.25
19-05-2014	4	10.1	10.2	1.1	0.99	9.56	y	0.259	16.8	0.159
19-05-2014	5	9.6	8.7	2.2	1.1	4.33	n	0.244	15.9	0.352
19-05-2014	6	5.6	5.0	1.3	1.11	4.29	n	0.142	9.2	0.355
19-05-2014	7	5.3	3.3	0.6	1.59	8.53	n	0.135	8.8	0.179
19-05-2014	8	4.2	3.1	0.9	1.37	4.82	n	0.108	7.0	0.316
19-05-2014	9	7.5	5.2	0.7	1.45	10.72	n	0.191	12.4	0.142
19-05-2014	10	6.8	4.9	1.2	1.39	5.65	n	0.173	11.3	0.27
19-05-2014	11	8.0	2.4	0.5	3.33	17.97	n	0.205	13.3	0.085
19-05-2014	12	7.9	6.0	0.8	1.33	10.2	y	0.202	13.1	0.149
19-05-2014	13	6.8	6.4	0.6	1.06	11.91	y	0.173	11.2	0.128
19-05-2014	14	8.5	5.6	2.5	1.53	3.44	n	0.218	14.1	0.443
19-05-2014	15	8.7	6.2	1.3	1.41	6.79	y	0.222	14.4	0.224
19-05-2014	16	10.7	8.3	2.1	1.29	5.02	n	0.272	17.7	0.303
19-05-2014	17	8.1	6.9	1.0	1.17	8.36	y	0.207	13.4	0.182
19-05-2014	18	7.1	6.3	1.7	1.12	4.16	n	0.181	11.8	0.366
19-05-2014	19	7.2	5.5	1.1	1.3	6.32	y	0.183	11.9	0.241
19-05-2014	20	7.7	4.7	1.7	1.65	4.52	y	0.197	12.8	0.337
19-05-2014	21	5.8	5.1	2.3	1.14	2.59	n	0.148	9.6	0.589
19-05-2014	22	5.8	4.6	1.6	1.26	3.55	n	0.147	9.6	0.43

Depending on the type of visualization (shadowgraph or free view), the exposure times for these series are varied between 1 s and 899.22 s. The videos are recorded at 1,000 fps or 3,200 fps with a resolution of 1280 x 800 pixels. For this concentration, Rswitch is estimated to 0.392 m. The expansion ratio is 0.220.

Table B.4: Test matrices of two bubble tests with 15% H_2 in air (without soap bubble)

Test Date	Test ID	R_1, cm	R_2, cm	Separation D, cm	R_1/R_2	R_1/D	Ignition	$R_1/Rswitch$	$R_1{}^*$, cm	$D/(R_1{}^* - R_1)$
10-05-2014	1	6.1	4.8	0.9	1.28	6.49	n	0.156	10.1	0.235
10-05-2014	4	5.6	6.0	3.8	0.93	1.48	n	0.142	9.2	1.027
10-05-2014	5	8.4	6.9	1.2	1.22	7.21	y	0.215	14.0	0.211
10-05-2014	6	9.4	7.2	2.3	1.32	4.17	n	0.24	15.6	0.366
10-05-2014	7	9.1	5.7	1.7	1.61	5.4	n	0.233	15.1	0.282
10-05-2014	8	9.0	6.5	1.7	1.39	5.42	y	0.23	15.0	0.281
10-05-2014	9	9.0	6.4	1.4	1.39	6.53	y	0.228	14.8	0.233
10-05-2014	10	10.0	8.2	3.4	1.23	2.92	n	0.255	16.6	0.522
10-05-2014	11	9.8	8.2	1.7	1.19	5.69	y	0.25	16.2	0.268
10-05-2014	12	11.0	9.4	1.6	1.16	7.03	y	0.28	18.2	0.217
10-05-2014	13	13.0	10.7	0.9	1.22	14.67	y	0.332	21.6	0.104
10-05-2014	14	11.2	9.4	6.7	1.2	1.68	n	0.285	18.5	0.908
10-05-2014	15	8.9	8.6	3.7	1.03	2.41	n	0.228	14.8	0.633
10-05-2014	16	9.2	9.1	3.2	1.01	2.85	y	0.235	15.2	0.535
10-05-2014	17	6.4	6.0	1.7	1.06	3.79	n	0.164	10.6	0.403
10-05-2014	18	6.9	6.2	1.2	1.11	5.7	y	0.176	11.4	0.267
10-05-2014	19	6.8	7.9	1.8	0.86	3.76	y	0.174	11.3	0.406
10-05-2014	20	4.8	5.8	1.0	0.84	5	y	0.123	8.0	0.305
17-05-2014	1	7.5	5.3	2.6	1.43	2.88	n	0.191	12.4	0.529
17-05-2014	2	7.3	6.0	2.4	1.22	3.08	n	0.186	12.1	0.495
17-05-2014	3	6.5	6.7	2.2	0.97	2.9	n	0.166	10.8	0.525
17-05-2014	4	6.4	6.4	0.8	0.99	7.76	n	0.162	10.6	0.196
17-05-2014	5	8.2	5.9	1.6	1.39	4.97	y	0.208	13.5	0.307
17-05-2014	6	6.5	6.1	1.3	1.07	5.11	y	0.165	10.7	0.298
17-05-2014	12	6.5	6.7	2.8	0.97	2.33	n	0.166	10.8	0.655
17-05-2014	20	5.0	4.5	1.3	1.1	3.98	n	0.127	8.3	0.383
17-05-2014	21	3.7	4.0	1.3	0.93	2.83	n	0.094	6.1	0.538

The exposure time for these series is between 899.22 *s*. The videos are recorded at 1,000 fps with a resolution of 1280 x 800 pixels. For this concentration, R_{switch} is estimated to 0.392 m. The expansion ratio is 0.220.

Table B.5: Test matrices of two bubble tests with 20% H_2 in air (with soap bubble)

Test Date	Test ID	R_1, cm	R_2, cm	Separation D, cm	R_1/R_2	R_1/D	Ignition	$R_1/Rswitch$	$R_1{}^*$, cm	$D/(R_1{}^* - R_1)$
21-05-2014	2	9.4	8.6	5.7	1.09	1.66	y	0.015	16.6	0.786
21-05-2014	18	9.7	7.4	6.7	1.31	1.45	n	0.015	17.1	0.903
21-05-2014	29	7.9	7.2	3.6	1.1	2.21	y	0.012	13.9	0.591
21-05-2014	30	9.5	7.7	6.6	1.23	1.44	n	0.015	16.8	0.906

The exposure time for these series is 899.22 s. The videos are recorded at 1,000 fps with a resolution of 1280 x 800 pixels. For this concentration, R_{switch} is estimated to 6.448 m. The expansion ratio is 0.182.

Table B.6: Test matrices of two bubble tests with 20% H_2 in air (without soap bubble)

Test Date	Test ID	R_1 [cm]	R_2 [cm]	Separation D [cm]	R_1/R_2	R_1/D	Ignition	$R_1/Rswitch$	${R_1}^*$ [cm]	$D/({R_1}^* - R_1)$
20-05-2014	3	11.3	11.3	3.1	1.27	3.61	y	0.017	19.9	0.362
20-05-2014	4	9.0	9.0	2.0	1.31	4.42	y	0.014	15.8	0.296
20-05-2014	5	6.1	6.1	3.3	1.08	1.85	n	0.009	10.8	0.706
20-05-2014	6	5.0	5.0	0.9	1.09	5.5	y	0.008	8.8	0.237
20-05-2014	7	5.3	5.3	2.2	1.04	2.37	n	0.008	9.3	0.551
20-05-2014	8	4.9	4.9	2.9	1.04	1.71	n	0.008	8.7	0.762
20-05-2014	9	6.4	4.9	1.5	1.3	4.3	y	0.01	11.2	0.304
21-05-2014	1	9.7	9.0	3.2	1.07	3.05	y	0.015	17.1	0.428
21-05-2014	3	12.0	9.6	5.6	1.25	2.16	n	0.019	21.2	0.605
21-05-2014	4	13.0	9.6	8.4	1.36	1.55	n	0.02	23.0	0.844
21-05-2014	5	7.1	8.7	4.9	0.81	1.44	n	0.011	12.6	0.906
21-05-2014	7	8.7	7.1	2.2	1.23	3.9	y	0.013	15.4	0.334
21-05-2014	8	6.4	6.4	2.9	0.99	2.22	n	0.01	11.2	0.588
21-05-2014	9	9.6	7.3	3.3	1.31	2.93	y	0.015	16.9	0.446
21-05-2014	10	9.9	9.3	4.1	1.06	2.43	y	0.015	17.4	0.537
21-05-2014	11	9.5	8.3	5.0	1.15	1.9	y	0.015	16.8	0.686
21-05-2014	12	9.2	8.1	5.9	1.13	1.54	n	0.014	16.2	0.845
21-05-2014	13	6.4	7.8	2.7	0.82	2.35	y	0.01	11.2	0.555
21-05-2014	14	6.8	6.5	4.8	1.06	1.43	n	0.011	12.1	0.911
21-05-2014	15	7.4	7.0	4.4	1.06	1.67	n	0.011	13.0	0.78
21-05-2014	16	8.3	7.5	2.8	1.11	3.02	y	0.013	14.7	0.432
21-05-2014	17	10.3	8.6	6.3	1.2	1.64	n	0.016	18.3	0.797
21-05-2014	19	8.9	6.7	5.4	1.31	1.64	n	0.014	15.6	0.797
21-05-2014	20	5.9	5.7	2.1	1.04	2.77	y	0.009	10.4	0.471
21-05-2014	21	6.2	5.6	3.6	1.1	1.73	y	0.01	10.9	0.754
21-05-2014	27	5.7	5.3	2.3	1.08	2.43	y	0.009	10.0	0.537
21-05-2014	28	9.0	8.1	4.5	1.11	2	y	0.014	15.9	0.653

The exposure time for these series is 899.22 s. The videos are recorded at 1,000 fps with a resolution of 1280 x 800 pixels.

For this concentration, R_{switch} is estimated to 6.448 m. The expansion ratio is 0.182.

Table B.7: Test matrices of two bubble tests with 30% H_2 in air (with soap bubble)

Test Date	Test ID	R_1 [cm]	R_2 [cm]	Separation D [cm]	R_1/R_2	R_1/D	Ignition	$R_1/Rswitch$	${R_1}^*$ [cm]	$D/({R_1}^* - R_1)$
13-03-2013	1	7.2	3.5	5.1	2.05	1.42	y	0.00108	13.6	0.785
13-03-2013	2	7.5	6.7	2.0	1.12	3.78	y	0.00113	14.2	0.294
13-03-2013	3	2.3	6.8	1.9	0.34	1.25	y	0.00035	4.4	0.889
13-03-2013	4	2.9	8.4	2.2	0.35	1.35	y	0.00044	5.6	0.824
13-03-2013	5	4.1	5.9	3.1	0.7	1.33	n	0.00061	7.7	0.834
13-03-2013	6	4.2	3.4	1.3	1.22	3.21	n	0.00063	7.9	0.346
13-03-2013	8	2.7	3.5	2.5	0.76	1.05	y	0.0004	5.1	1.057
15-03-2013	1	4.3	5.0	4.0	0.85	1.06	n	0.00064	8.1	1.045
15-03-2013	2	5.3	5.5	4.4	0.97	1.2	n	0.00081	10.1	0.925
15-03-2013	3	4.9	6.2	4.0	0.79	1.24	n	0.00075	9.4	0.895
15-03-2013	4	6.9	4.6	4.2	1.5	1.65	n	0.00104	13.1	0.672
15-03-2013	6	7.4	4.2	3.1	1.77	2.4	n	0.00111	14.0	0.464
15-03-2013	7	6.3	3.9	3.1	1.62	2.03	y	0.00095	11.9	0.548
18-03-2013	1	5.5	5.3	2.4	1.03	2.29	y	0.00083	10.4	0.486
18-03-2013	2	5.5	5.1	2.6	1.09	2.13	y	0.00084	10.5	0.523
18-03-2013	3	6.5	5.4	3.5	1.2	1.86	n	0.00099	12.4	0.596
18-03-2013	4	8.4	6.1	1.1	1.37	7.84	y	0.00127	15.9	0.142
18-03-2013	5	7.2	6.4	4.5	1.13	1.58	y	0.00108	13.6	0.703
18-03-2013	6	5.8	5.0	7.3	1.15	0.79	n	0.00087	11.0	1.41
18-03-2013	7	7.6	4.6	3.1	1.64	2.49	y	0.00115	14.4	0.446
18-03-2013	8	5.9	4.3	5.7	1.36	1.03	n	0.00089	11.2	1.079
18-03-2013	9	5.2	4.9	3.9	1.05	1.31	y	0.00078	9.8	0.847
21-03-2013	2	6.0	6.4	6.2	0.94	0.96	n	0.00091	11.4	1.16
21-03-2013	3	7.7	6.2	3.5	1.25	2.2	y	0.00117	14.7	0.51
21-03-2013	4	6.8	5.7	3.9	1.19	1.75	y	0.00103	13.0	0.64
21-03-2013	5	5.3	6.5	4.8	0.82	1.12	n	0.00081	10.1	0.99
21-03-2013	6	2.9	4.3	3.4	0.69	0.86	n	0.00044	5.6	1.29

Test Date	Test ID	R_1 [cm]	R_2 [cm]	Separation D [cm]	R_1/R_2	R_1/D	Ignition	$R_1/Rswitch$	${R_1}^*$ [cm]	$D/({R_1}^* - R_1)$
02-04-2013	1	6.0	6.4	2.8	0.93	2.15	y	0.00091	11.4	0.52
02-04-2013	2	6.8	7.1	6.5	0.96	1.05	n	0.00103	13.0	1.06
02-04-2013	3	8.1	6.7	3.8	1.2	2.14	y	0.00122	15.4	0.52
02-04-2013	4	7.3	4.7	4.8	1.57	1.52	y	0.00111	13.9	0.73
02-04-2013	5	4.2	5.7	2.1	0.74	1.97	y	0.00064	8.0	0.56
02-04-2013	6	4.7	4.1	2.5	1.16	1.87	y	0.00072	9.0	0.59
05-04-2013	1	7.3	9.0	2.4	0.81	3.06	y	0.00111	13.9	0.36
05-04-2013	2	9.1	9.7	1.2	0.94	7.59	y	0.00137	17.3	0.15
05-04-2013	3	5.1	6.0	4.4	0.85	1.16	n	0.00077	9.7	0.96
05-04-2013	4	5.7	7.3	6.2	0.79	0.92	y	0.00087	10.9	1.21
05-04-2013	5	6.1	6.1	7.3	1	0.83	n	0.00092	11.5	1.34
05-04-2013	6	6.1	5.2	6.4	1.15	0.94	n	0.00091	11.5	1.18
05-04-2013	7	5.4	6.0	6.6	0.91	0.82	n	0.00082	10.3	1.35
16-04-2013	1	7.2	6.4	6.3	1.13	1.14	n	0.00109	13.8	0.97
16-04-2013	2	8.6	6.6	6.5	1.31	1.32	n	0.0013	16.4	0.84
16-04-2013	3	10.5	8.1	4.7	1.29	2.24	y	0.00158	19.9	0.5
16-04-2013	4	10.4	7.8	5.0	1.33	2.09	y	0.00157	19.8	0.53
16-04-2013	5	6.5	5.8	6.3	1.12	1.04	n	0.00099	12.4	1.07
16-04-2013	6	6.6	5.9	6.3	1.13	1.05	y	0.001	12.5	1.06
16-04-2013	7	4.1	4.2	3.8	0.97	1.06	n	0.00062	7.7	1.05

Depending on the type of visualization (shadowgraph or free view), the exposure times for these series are varied between 1 s, 8 s and 899.22 s. Most of the videos are recorded at 1,000 or 3,000fps with a resolution of 1280 x 800 pixels. For this concentration, R_{switch} is estimated to 66.15 m. The expansion ratio is 0.146.

Table B.8: Test matrices of two bubble tests with 30% H_2 in air (without soap bubble)

Test Date	Test ID	R_1 [cm]	R_2 [cm]	Separation D [cm]	R_1/R_2	R_1/D	Ignition	$R_1/Rswitch$	$R_1{}^*$ [cm]	$D/(R_1{}^* - R_1)$
25/10/2013	2	8.4	4.1	3.4	2.05	2.46	y	0.00127	16.0	0.452
25/10/2013	4	8.1	4.5	4.0	1.79	2.04	n	0.00122	15.4	0.545
25/10/2013	5	8.3	4.2	4.6	1.98	1.8	n	0.00126	15.8	0.618
25/10/2013	7	8.5	4.9	3.6	1.73	2.34	y	0.00128	16.1	0.475
08/11/2013	2	9.9	7.5	14.5	1.31	0.68	n	0.00149	18.7	1.637
08/11/2013	3	9.5	9.3	12.2	1.02	0.78	n	0.00143	18.0	1.425
08/11/2013	4	9.9	7.7	10.6	1.29	0.94	n	0.0015	18.9	1.18
08/11/2013	5	10.0	6.5	7.9	1.54	1.27	n	0.00151	19.0	0.873
08/11/2013	6	10.1	6.8	6.7	1.49	1.5	n	0.00153	19.2	0.741
08/11/2013	7	10.0	7.5	5.2	1.33	1.93	n	0.00151	19.0	0.577
08/11/2013	8	9.8	7.0	4.4	1.41	2.25	y	0.00148	18.6	0.495
08/11/2013	9	7.3	4.8	3.6	1.54	2.04	y	0.00111	14.0	0.544
08/11/2013	10	6.9	4.9	4.3	1.41	1.59	n	0.00104	13.1	0.698
08/11/2013	11	6.4	5.2	2.8	1.23	2.3	y	0.00097	12.2	0.483
08/11/2013	12	7.2	5.0	4.5	1.45	1.6	y	0.00109	13.8	0.696
08/11/2013	13	7.3	5.3	5.8	1.37	1.25	n	0.0011	13.8	0.889
08/11/2013	16	4.6	8.8	2.4	0.52	1.94	y	0.00069	8.7	0.574
08/11/2013	17	7.0	5.4	4.3	1.31	1.65	y	0.00106	13.4	0.675
15/11/2013	1	9.5	9.2	10.1	1.03	0.94	n	0.00143	18.0	1.187
15/11/2013	2	8.5	8.2	7.8	1.03	1.09	n	0.00129	16.2	1.017
15/11/2013	3	6.4	6.1	5.3	1.03	1.19	n	0.00096	12.1	0.934
15/11/2013	4	6.7	6.1	3.4	1.09	1.95	n	0.00101	12.7	0.571
15/11/2013	5	5.9	5.3	2.4	1.11	2.44	y	0.0009	11.3	0.456
15/11/2013	7	5.8	5.1	3.0	1.14	1.95	n	0.00088	11.0	0.569
15/11/2013	8	5.5	5.6	2.1	0.99	2.59	y	0.00084	10.5	0.428

The exposure time for these series is 8 s. Most of the videos are recorded at 3,000 fps with a resolution of 1280 x 800 pixels. For this concentration, R_{switch} is estimated to 66.15 m. The expansion ratio is 0.146.

Appendix C

Results of the Two Spherical bubble tests

The following tables provide the results of the double spherical bubble tests using the shadowgraph system. The tests are organized according to the concentration of the mixture (11% H_2-air, 15% H_2-air, 20% and stoichiometric mixture) and either the soap bubble was burst or not prior to the experiments. Included in the table are the test's date, the test's number, the size of both bubbles, the separating distance, whether or not the transition was successful, the final radius of the flame and other ratios.

Table C.1: Test matrices of two spherical bubble tests with 11% H_2 in air (with soap bubble)

Test Date	Test ID	R_1 [cm]	R_2 [cm]	Separation D [cm]	R_1/R_2	R_1/D	Ignition	$R_1/Rswitch$	$R_1{}^*$ [cm]	$D/(R_1{}^* - R_1)$
22-08-2014	B1	6.0	5.7	2.2	1.05	2.72	n	1.332	9.2	0.672
22-08-2014	B10	9.7	9.6	0.0	1.01	-	n	2.161	14.9	0

Table C.2: Test matrices of two spherical bubble tests with 11% H_2 in air (without soap bubble)

Test Date	Test ID	R_1 [cm]	R_2 [cm]	Separation D [cm]	R_1/R_2	R_1/D	Ignition	$R_1/Rswitch$	${R_1}^*$ [cm]	$D/({R_1}^* - R_1)$
22-08-2014	B2	6.2	5.6	1.3	1.11	0.21	n	1.393	9.6	0.393
22-08-2014	B3	6.0	5.7	0.9	1.06	0.15	n	1.352	9.3	0.276
22-08-2014	B4	7.8	5.9	0.7	1.33	0.09	n	1.746	12.1	0.167
22-08-2014	B5	5.6	6.0	0.5	0.94	0.09	n	1.257	8.7	0.168
22-08-2014	B6	6.4	5.6	0.4	1.14	0.06	n	1.427	9.9	0.105
22-08-2014	B7	6.9	5.1	3.0	1.36	0.43	n	1.539	10.6	0.787
22-08-2014	B8	5.6	7.5	1.4	0.75	0.25	n	1.252	8.7	0.458
22-08-2014	B9	6.0	7.0	1.0	0.86	0.16	n	1.340	9.3	0.289
22-08-2014	B11	6.0	5.1	1.8	1.19	0.29	n	1.350	9.3	0.535
22-08-2014	B12	6.5	5.5	1.5	1.18	0.23	n	1.447	10.0	0.429
22-08-2014	B13	6.0	5.3	1.7	1.13	0.28	n	1.335	9.2	0.513
22-08-2014	B14	5.7	5.0	1.3	1.14	0.23	n	1.264	8.7	0.423
22-08-2014	B15	5.6	5.2	1.2	1.09	0.21	n	1.250	8.6	0.388
22-08-2014	B16	6.0	5.7	0.4	1.04	0.07	n	1.340	9.3	0.125
22-08-2014	B17	5.7	5.1	1.3	1.11	0.23	n	1.264	8.7	0.423

Table C.3: Test matrices of two spherical bubble tests with 15% H_2 in air (with soap bubble)

Test Date	Test ID	R_1, cm	R_2, cm	Separation D, cm	R_1/R_2	R_1/D	Ignition	$R_1/Rswitch$	$R_1{}^*$, cm	$D/(R_1{}^* - R_1)$
30-07-2014	2	4.8	4.6	0.8	1.03	5.83	y	0.122	7.9	0.261
30-07-2014	3	4.9	4.6	3.4	1.07	1.46	n	0.125	8.1	1.047
30-07-2014	4	5.3	5.1	2.8	1.02	1.86	n	0.134	8.7	0.817
30-07-2014	5	5.3	4.5	2.3	1.19	2.32	n	0.136	8.8	0.656
05-08-2014	1	4.8	3.9	1.1	1.24	0.23	y	0.123	8.0	0.344
05-08-2014	10	5.1	4.5	0.8	1.13	0.16	y	0.130	8.5	0.244

Table C.4: Test matrices of two spherical bubble tests with 15% H_2 in air (without soap bubble)

Test Date	Test ID	R_1, cm	R_2, cm	Separation D, cm	R_1/R_2	R_1/D	Ignition	$R_1/Rswitch$	$R_1{}^*$, cm	$D/(R_1{}^* - R_1)$
30-07-2015	1	5.4	5.0	2.9	1.09	1.87	n	0.137	8.9	0.814
30-07-2016	6	4.5	4.1	3.3	1.09	1.37	n	0.114	7.4	1.115
05-08-2014	2	3.9	3.9	2.5	0.99	0.65	n	0.099	6.5	0.991
05-08-2014	3	4.4	4.6	1.5	0.97	0.33	n	0.113	7.4	0.5
05-08-2014	4	5.0	5.1	1.4	0.98	0.29	y	0.127	8.3	0.437
05-08-2014	5	4.6	4.6	1.9	1.01	0.4	n	0.118	7.6	0.614
05-08-2014	6	5.1	4.4	0.8	1.15	0.16	y	0.129	8.4	0.24
05-08-2014	7	4.5	4.4	1.7	1.02	0.37	n	0.116	7.5	0.563
05-08-2014	8	5.4	4.6	1.4	1.17	0.26	y	0.139	9.0	0.395
05-08-2014	9	6.1	4.3	2.6	1.4	0.42	n	0.154	10.0	0.645

Table C.5: Test matrices of two spherical bubble tests with 20% H_2 in air (with soap bubble)

Test Date	Test ID	R_1, cm	R_2, cm	Separation D, cm	R_1/R_2	R_1/D	Ignition	$R_1/Rswitch$	${R_1}^*$, cm	$D/({R_1}^* - R_1)$
06-08-2014	B1	4.7	51.5	3.6	1.15	1.29	n	0.007	8.3	1.013
06-08-2014	B2	4.7	56.1	1.0	1.07	4.62	y	0.007	8.4	0.283
06-08-2014	B3	5.6	55.9	2.6	1.27	2.18	y	0.009	9.9	0.6
06-08-2014	B4	5.5	60.5	3.9	1.15	1.43	n	0.009	9.7	0.914
12-08-2014	B1	4.6	59.8	1.0	0.95	0.21	y	0.007	8.0	0.276
12-08-2014	B15	7.4	91.8	3.5	1	0.47	n	0.011	13.0	0.617

Table C.6: Test matrices of two spherical bubble tests with 20% H_2 in air (without soap bubble)

Test Date	Test ID	R_1 [cm]	R_2 [cm]	Separation D [cm]	R_1/R_2	R_1/D	Ignition	$R_1/Rswitch$	${R_1}^*$ [cm]	$D/({R_1}^* - R_1)$
12-08-2014	B2	4.6	4.3	1.4	1.06	0.31	y	0.007	8.1	0.399
12-08-2014	B3	4.8	5.3	2.9	0.92	0.59	y	0.007	8.5	0.775
12-08-2014	B4	5.9	4.4	4.6	1.32	0.78	n	0.009	10.4	1.015
12-08-2014	B5	5.9	4.9	1.9	1.2	0.33	y	0.009	10.4	0.427
12-08-2014	B6	5.2	4.5	4.3	1.16	0.84	n	0.008	9.2	1.094
12-08-2014	B7	5.6	4.7	3.7	1.19	0.65	n	0.009	9.9	0.852
12-08-2014	B8	6.0	4.5	3.7	1.32	0.62	n	0.009	10.5	0.806
12-08-2014	B9	6.6	5.2	0.4	1.27	0.06	y	0.010	11.7	0.074
12-08-2014	B10	6.2	6.2	1.8	1.01	0.29	y	0.010	11.0	0.382
12-08-2014	B11	6.3	6.2	5.6	1.02	0.89	n	0.010	11.2	1.162
12-08-2014	B12	7.1	4.9	3.7	1.46	0.52	n	0.011	12.5	0.672
12-08-2014	B13	7.2	6.5	1.6	1.11	0.23	y	0.011	12.7	0.297
12-08-2014	B14	6.8	7.0	4.3	0.97	0.63	n	0.011	12.0	0.817
12-08-2014	B16	7.5	6.5	3.6	1.16	0.48	y	0.012	13.3	0.625
12-08-2014	B17	6.9	7.4	1.6	0.93	0.24	y	0.011	12.1	0.313
12-08-2014	B18	7.6	4.6	3.6	1.67	0.47	n	0.012	13.4	0.608
12-08-2014	B19	5.7	7.1	2.4	0.79	0.42	y	0.009	10.0	0.554
12-08-2014	B20	5.6	8.1	4.0	0.69	0.72	n	0.009	9.9	0.937
12-08-2014	B21	6.0	6.8	3.9	0.89	0.64	n	0.009	10.7	0.838
12-08-2014	B22	8.1	7.3	4.7	1.11	0.58	n	0.013	14.3	0.756

Table C.7: Test matrices of two spherical bubble tests with 30% H_2 in air (with soap bubble)

Test Date	Test ID	R_1 [cm]	R_2 [cm]	Separation D [cm]	R_1/R_2	R_1/D	Ignition	$R_1/Rswitch$	$R_1{}^*$ [cm]	$D/(R_1{}^* - R_1)$
15-08-2014	B1	5.9	6.9	2.0	0.86	2.95	y	0.0009	11.3	0.376
15-08-2014	B2	7.1	6.3	5.1	1.12	1.4	n	0.0011	13.5	0.793
15-08-2014	B3	6.5	7.0	2.6	0.92	2.51	y	0.0010	12.3	0.443
15-08-2014	B4	6.4	7.6	4.3	0.85	1.5	n	0.0010	12.2	0.741
15-08-2014	B5	5.9	7.4	3.0	0.8	1.96	n	0.0009	11.3	0.568
15-08-2014	B6	6.4	6.2	2.3	1.04	2.83	y	0.0010	12.2	0.392
15-08-2014	B7	6.3	6.2	4.8	1.01	1.32	n	0.0010	11.9	0.84
15-08-2014	B8	6.2	5.8	4.1	1.08	1.52	y	0.0009	11.8	0.729
15-08-2014	B9	6.9	5.6	6.0	1.24	1.14	y	0.0010	13.0	0.972
15-08-2014	B10	6.4	5.8	4.7	1.11	1.36	y	0.0010	12.2	0.818

Table C.8: Test matrices of two spherical bubble tests with 30% H_2 in air (without soap bubble)

Test Date	Test ID	R_1 [cm]	R_2 [cm]	Separation D [cm]	R_1/R_2	R_1/D	Ignition	$R_1/Rswitch$	$R_1{}^*$ [cm]	$D/(R_1{}^* - R_1)$
19-08-2014	B1	6.1	5.5	1.3	1.12	0.21	y	0.0009	11.6	0.231
19-08-2014	B2	6.3	6.0	2.0	1.05	0.31	y	0.0010	12.0	0.346
19-08-2014	B3	6.6	6.2	2.6	1.06	0.4	y	0.0010	12.5	0.447
19-08-2014	B4	7.1	6.3	4.9	1.14	0.69	n	0.0011	13.5	0.763
19-08-2014	B5	5.9	5.2	5.2	1.13	0.89	y	0.0009	11.2	0.985
19-08-2014	B6	5.8	5.8	7.0	1	1.2	n	0.0009	11.0	1.337
19-08-2014	B7	6.3	5.8	4.5	1.1	0.71	y	0.0010	12.1	0.793
19-08-2014	B8	6.2	5.6	4.9	1.13	0.78	n	0.0009	11.9	0.864
19-08-2014	B9	5.8	4.8	3.7	1.19	0.64	n	0.0009	11.0	0.713